



## Seeing the Light Through the Dark

J. ALVES<sup>1</sup>, C. LADA<sup>2</sup> and E. LADA<sup>3</sup>

<sup>1</sup>European Southern Observatory, Garching, Germany

<sup>2</sup>Harvard-Smithsonian Center for Astrophysics, Cambridge MA, USA; <sup>3</sup>University of Florida, Gainesville FL, USA

### 1. Introduction: The Search for the Initial Conditions for Star Formation

Stars and planets form within dark molecular clouds. However, despite 30

years of study, little is understood about the internal structure of these clouds and consequently the initial conditions that give rise to star and planet formation. This is largely due to the fact that molecular clouds are primarily com-

posed of molecular hydrogen, which is virtually inaccessible to direct observation. Because of its symmetric structure, the hydrogen molecule possesses

(Continued on page 15)

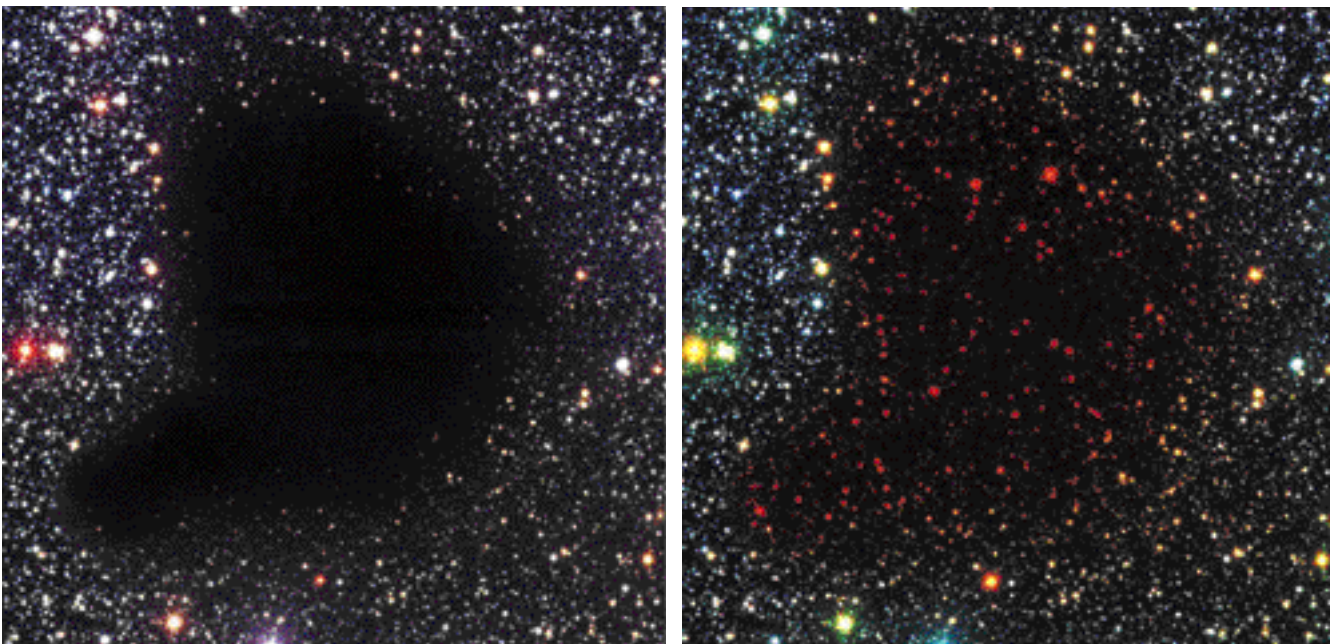


Figure 1: Visible and near-infrared images of Barnard 68. The images are a B, V, and I-band composite (left) and a B, I, Ks-band composite (right). At visual wavelengths the cloud is completely opaque owing to extinction of background starlight caused by small ( $\sim 0.1\mu\text{m}$ ) interstellar dust particles that permeate the cloud. The red stars detected at  $2\mu\text{m}$  through the visually opaque regions of the cloud (right) are the stars that will provide direct measurements of dust extinction through the cloud.

## La Silla Telescope Status, a Great Achievement on Image Quality Performances

A. GILLIOTTE, ESO

Nowadays almost all La Silla telescopes deliver very good image quality, routinely achieving sub-arcsec images. In some cases, the theoretically predicted performances of the telescope is matched, or the limitations are at least understood.

The image quality, however, is not only a function of the telescope optical set-up, it is also highly dependent on the cleanliness of the optical surfaces.

### Main Mirror Maintenance

Five years ago, systematic cleaning of the primary mirrors using CO<sub>2</sub> was implemented on the major telescopes: the NTT, 3.6-m, 2.2-m and Danish 1.54-m. Main mirror cleaning is now carried out by the telescope team as part of the routine maintenance operation. The only restriction with this process is that the humidity cannot be too high. Indeed, high humidity causes the condensed water surrounding each cold CO<sub>2</sub> particle to stick the dust to the mirror surface, resulting in an accumulation of dust on the mirror.

A mirror water washing operation, performed by the opticians, was also implemented about three years ago. The best period to wash the mirrors is the end of the summer, when the high humidity is decreasing and hence the frequency of the CO<sub>2</sub> cleaning was disrupted. The mirror washing was first implemented on the NTT, whose mirror

cell was designed for such a process, then on the 3.6-m and is soon to be carried out on the 2.2-m as well.

The optimal frequency of the CO<sub>2</sub> cleaning, resulting in clean mirrors without too much time spent on the operation, was found to be one week. The NTT was the test bench for the process with the mirror surface maintaining good reflectivity for a three-year period with the regular CO<sub>2</sub> cleaning and four "in-situ" washings (Fig.1).

Aphtograph of the washing operation at the NTT is also presented in Figure 2.

All the above-mentioned telescopes were realuminised during the year 2000 and the reflectivity is still above 88% at 670 nm with low roughness. The 2.2-m main mirror suffered some water contamination during the bad winter period and a first washing is scheduled for the near future. Recently, the 3.6-m main mirror also suffered water contamination from cooling liquid, and the washing is already scheduled end of March.

The status of the mirror is verified on a monthly basis with a measure of the R% and roughness. A database of the mirror status for the main telescopes will soon be available on the La Silla web site.

### Telescope Image Quality

About nine years ago, the awareness of the observer towards the image quality increased and the quality delivered

by the 3.6-m was found insufficient because the improvements in the performance and dynamic range of the detectors showed more accurately the image quality achieved by the telescope. With the availability of wavefront sensors – the first one available was a Shack-Hartmann type called Antares – the optical quality of the telescope was measured more often, and more precise aberration information was obtained. On several occasions, large aberrations were identified. The spherical aberration, often mistaken for seeing quality, appeared clearly and only the decentring coma was adjusted after measurements performed only on zenith. It was found that almost all third-order aberrations were affecting the telescope. The most critical issue concerned the instability of the aberrations at different telescope orientations as well as with changes in temperature. A dedicated study with eventual periods of closed telescope was really compulsory. In 1994, a complete study of the 3.6-m with a contracted optical engineer on La Silla was initiated to determine the status of the telescope and to find a way of improving it.

During this process, we gathered considerable experience in solving problems with the telescope, but also a deeper knowledge of the limitations of the telescope was reached. The 2.2-m, Danish 1.54-m and the NTT have all benefited from this exercise. Of course, the active optics concept, greatly demonstrated with the NTT, allowed a better understanding of the local thermal contribution.

The contributions of dome and mirror seeing were identified and a solution to decrease both has been found.

Thanks to all the La Silla staff for their ongoing interest and success in improving the image quality at the telescopes on site.

### The NTT Status

This telescope delivers the best image quality on La Silla with the active optics system fulfilling all expectations. Initially, the limiting factor for this telescope was found to be the image quality of the La Silla site. Now, after a long period of operation, more image quality limitations have appeared. To monitor the image quality, the NTT has a distinct advantage over the other telescopes as repeated image analysis is made during the observations. All re-

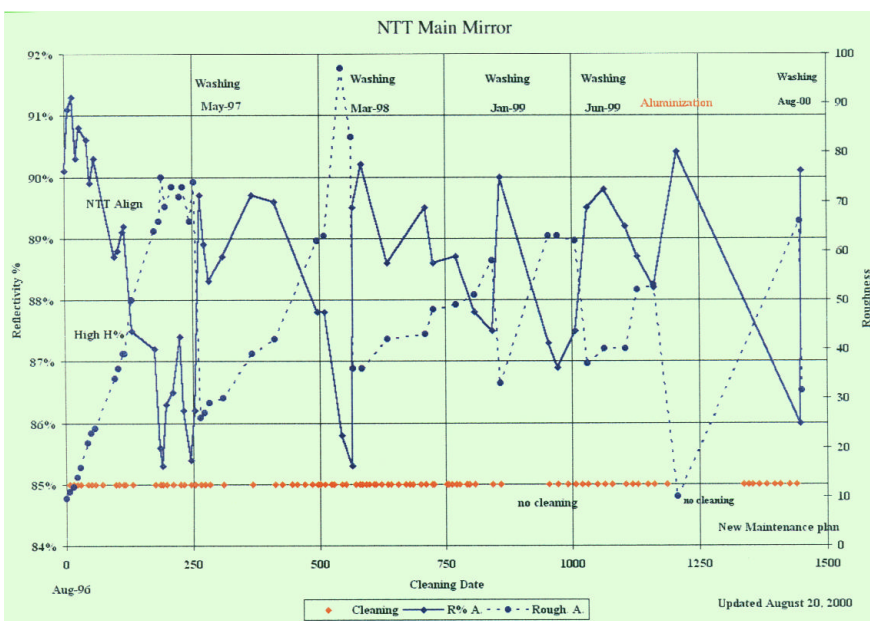


Figure 1: The variation of the reflectivity (R%) and roughness of the NTT main mirror during the period from August 1996 to August 2000.



Figure 2: The NTT main mirror being rinsed with distilled water. The last washing step before drying the mirror surface.

sults are logged in a database, and statistics can be performed with respect to external meteorological conditions or other parameters. The image quality generally becomes poorer when the wind speed is below 5 m/s or if the temperature is dropping rapidly as demonstrated by Figure 3a.

Several recommendations were made to the NTT team to improve the image quality:

- Install high flux fans to produce artificial wind to reduce mirror seeing.
- Install a new M2 baffle with open shade to avoid warm bubble formation.
- Improve the air conditioning in the instrument room to avoid a positive gradient.

- Install a Nasmyth shutter to close the optical path not in operation.

The new baffle and fans have been installed and the new results already show a substantial improvement in the image quality (cf. Fig. 3b).

The air-conditioning of the instrument rooms was slightly improved but an optimal solution could not be implemented because of high cost.

The timing of a complete image analysis and mirror correction cycle is unfortunately long in comparison with the VLT active optics system. On some occasions, more frequently than before, the active optics is not converging properly. Hence the telescope does not always operate in closed-loop correction. Some efforts should be undertaken

to reach the same operational mode as used on the VLT.

A complete maintenance of the astatic levers is underway to recalibrate and readjust each lever. For perfect imaging quality at the zenith, each lever must be adjusted to the medium range of the counterweight move, and the spring compensation tuned to compensate the spherical aberration constant term. This time-consuming operation will be performed during 2001.

The possible upgrade of the active optics will also include a standardisation of the present software to comply with the latest version at the VLT.

### The 3.6-m Status

Excellent work at the 3.6-m has resulted in improved image quality due to the minimisation of the spherical aberration, triangular and astigmatism contributions, even when the telescope is inclined. In addition, the dome and mirror seeing contributions are now almost negligible. The main limitations affecting image quality are the coma instability when moving the telescope far from the zenith. Astigmatism is still slightly high, with a contribution coming from the axial fixed points. A new design of the axial fixed point contact on the mirror back side is compulsory to reduce a lateral stress applied on the mirror.

A new support for the M2 unit is currently under study. It will mainly be a copy of the present NTT M2 adjusting support. The improvement to image quality will be significant, with the coma variation kept under control at a low value. We are still awaiting the green light to build and implement this new unit.

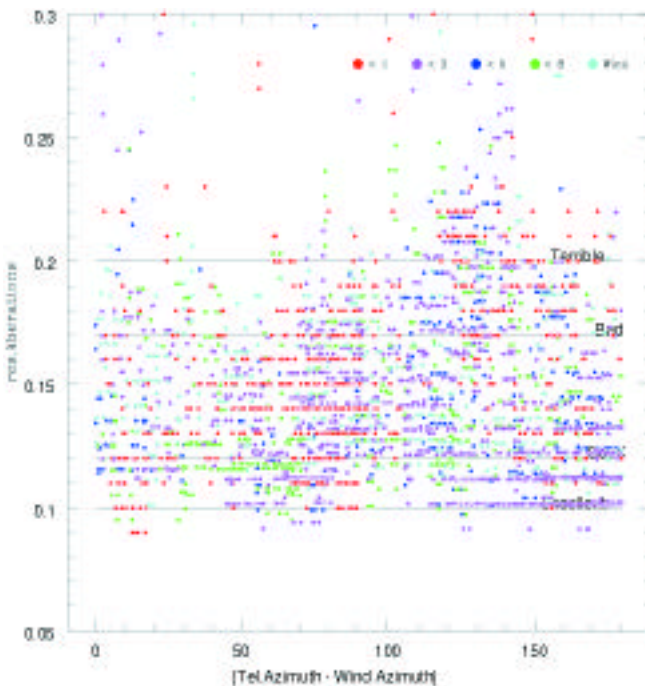


Figure 3a represents the "fitting" residual variations (non-modelised 7 first aberrations) of the image quality with NTT dome position relative to the wind direction as well as the wind speed. Colour code of wind speed is at top of figure in m/s.

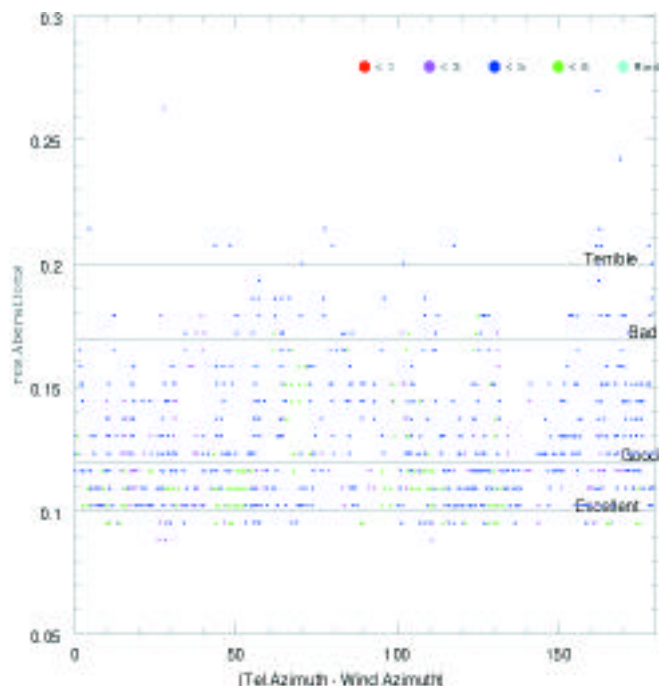


Figure 3b corresponds to the same layout as Figure 3a, after installation of the new baffle and fans.

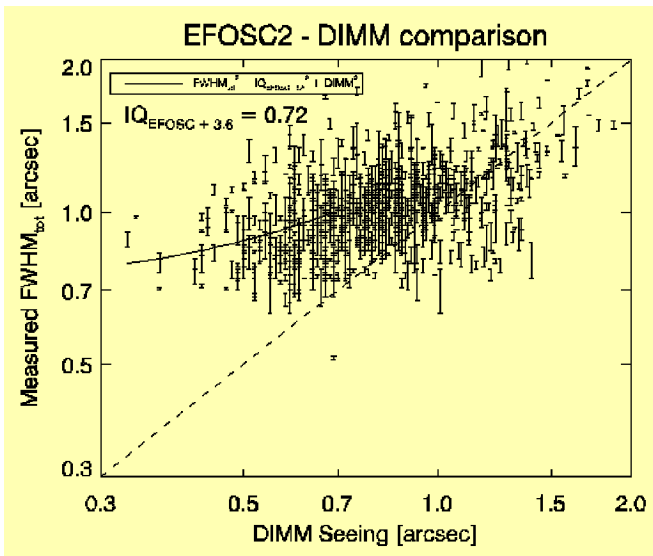


Figure 4 shows that the image quality is, on several occasions, better than that measured by the Dimm monitor. Local site effects and the mirror fans are most likely the reason for the better seeing measured at EFOSC2 on these occasions. Image quality can be as good as 0.6 arcsec and ranges up to 1.5 arcsec, with the coma variation being the main reason for the measured spread in EFOSC2 seeing quality.

coma terms are almost stable and below 0.2 arcsec.

The telescope focus has been shifted to compensate the high constant term of the spherical aberration. However, the variability of this aberration was not confirmed at the time when the amount by which to shift the focus was decided. Although the right correction may not have been applied, observers are not reporting poor image quality. The main limitation of image quality at the Danish 1.54-m is still the instrument detector sampling. Even after the recent detector changes (October 2000), the sampling of 0.81 arcsec (2 pixels of 0.015 mm with a scale of 27 arcsec/mm) is often reached when the night seeing conditions are around or below 0.6 arcsec. (The previous CCD suffered from diffusion transfer increasing in fact the pixel size.)

The present status of the image quality at the 3.6-m, despite the two remaining limitations, is already within the objectives fixed at the beginning of the study. We have achieved the goal of 0.9 arcsec within 60 deg Zenithal Distance and image quality as good as 0.6 arcsec has been measured with EFOSC2. The EFOSC2 sampling limit of two pixels is now often attained.

For the last few months, the EFOSC2 image quality is logged together with the external seeing. Figure 4 speaks for itself about the present quality of images. The EFOSC2 image quality is already acknowledged by the ESO community.

The Infrared mode of the telescope with the F/35 chopping M2 mirror has also been improved. The image quality obtained at 10 and 20 microns with the new TIMM12 is diffraction limited.

#### The 2.2-m Status

During 2000, the telescope has been greatly improved with the large decrease in the contribution from astigmatism. A separate article describes these activities.

Observers often report the image quality as very good, and sub-arcsec images are often obtained when the outside seeing is good. The limiting resolution of the Wide Field Imager pixel size is often reached when the seeing is below 0.5 arcsec and the mirror colder than the outside air.

Image quality limitations still exist but are more related to thermal contributions rather than opto-mechanical features.

#### The Danish 1.54-m Status

The ongoing problem of the spherical aberration varying with the temperature has been studied again. Experience gained on the 3.6-m, NTT and 2.2-m presented a possible explanation of this challenging feature. Again, the opto-mechanical mirror support seems to be guilty and the behaviour of the axial fixed points with temperature variations is the most probable explanation. A bending effect at the mirror edge, where the spherical aberration is more sensitive, could produce the 0.3 arcsec variable term of this aberration. The defocus, astigmatism, quadratic and

#### Pending Issues

A further step on improving the image quality of the telescopes will be considered this year. A large part of the stray light level affecting the depth of the image, is related to the telescope baffling quality as well as the cleanliness of the optical surface. At least three cases must be considered, the first case is when there is a high density of bright stars in the field, the second when there are very bright objects close to the target and the last case when there is a bright star almost alone in the field. The improvement of the telescope baffling will reduce at least the second case. The others depend primarily on the light diffusion by the optical surfaces. Of course, the mirror polishing quality improved dramatically between the construction of the 3.6-m and the VLT, but this benefit could be easily lost if the cleanliness of the mirror surface is not ensured.

The baffling status of the 2.2-m, the NTT and the 3.6-m telescopes must be verified and recommendations will be issued.

## Image Quality Improvement of the 2.2-m

A. GILLIOTTE, ESO

### Historical Overview

On the very first period of operation of the 2.2-m telescope, a direct CCD camera was offered to the community. With a pixel size of 0.35 arcsec and a small field of 3 arcmin, the telescope image quality was never reported as being bad or showing asymmetric, elliptical images. In the mid-1990s, a new

imaging instrument called EFOSC2 was installed at the telescope. Observers soon began seeing variable image elongations across the full field, which were later identified as coming from the instrument and not the telescope. Meanwhile, the optical quality of the telescope was measured to be as good as 0.35 arcsec d80% close to zenith, using our portable Shack-

Hartmann called Antares. The optical quality of the EFOSC instrument was strongly dependent on the precision with which focus had been achieved, and subsequent variations with temperature. The EFOSC camera focus did not include temperature compensation as was the case with EFOSC1 on the 3.6-m. The focus degradation introduced field curvature and increasing

astigmatism as one moved off-axis. Optical quality tests with EFOSC after refocusing the camera and performing a careful thorough focus sequence re-established the instrument and telescope quality within the resolution delivered by the two pixels sampling 0.7 arcsec.

### Image Quality Degradation

After the installation of the Wide-Field Imager (WFI), several observers reported bad, elongated images. The defect was identified as astigmatism which was found to increase for large North and East telescope orientations. On several occasions, even observations at zenith showed the same features. Only a telescope “shake-up” could remove the astigmatism, and even then, only temporarily.

Optical tests were performed on several occasions with the new Curvature Sensing Method (CSM) and these confirmed the astigmatism variation for large zenithal distances. Earlier tests only performed at zenith showed the correct quality. Observations with direct CCD and EFOSC2 in the past were not of sufficiently high spatial resolution to detect the problem. Therefore, the defect could have been present all along since the early days and gone unnoticed until the arrival of the WFI.

### Optical Tests

The tests could not reproduce the defect at zenith. Therefore, it seems that there was some dependence on the history of telescope movements. As had previously been done at the 3.6-m, the optical tests were performed by systematically moving the telescope along the same sequence each time. First, a blank sequence was followed to set the telescope properly, followed by South-North and East-West series. The CSM uses an ST8 SBIG CCD mounted on a translation stage to obtain the two defocused intra and extra focal images. Thirty-second exposures were performed to ensure that variations in the seeing were averaged out. This CCD is good in terms of sampling, with 9 μm pixels and a correct linearity to restore the beam intensity variance. The beam heterogeneity between both extrafocal images is produced by the optical aberrations.

The WFI image quality is very good when correct focus is achieved. The small difference in the filter optical thickness must be properly compensated by telescope focus offset. Temperature changes also introduce variation in the telescope focus. For conditions of very good seeing, the focus must be performed as carefully as possible. The WFI pixel size is only 0.24 arcsec, and with this, the sensitivity to telescope imaging defects is increased.

The astigmatism aberration was confirmed during all optical tests. It is always a challenge to identify the origin of the astigmatism, but unfortunately this can take a long time. Any kind of stress or buckling on the telescope mirror will trigger the first elastic deformation mode, and this corresponds to the optical astigmatism term.

From the outset, all supporting elements of both mirrors should be suspected. A complete check of all fixed points as well as astatic levers (radial and axial) needs to be performed. Because astigmatism was almost symmetric over such a large field, the aberration could not have been produced by a misalignment of the mirrors. In this case, the origin points more to how the mirrors are held. The defect appears at large inclination and sometimes remains at zenith. In a first pass, the main mirror support system should be studied followed by the secondary mirror if nothing is found.

Of course, the tests were conducted during short test periods within long stretches of observing time. This meant that it was mandatory to keep the telescope in a stable condition for the observers; which means that the tests could only be done in small conservative steps.

### A Contribution from the Instrument Operation

An additional problem was discovered which almost certainly contributed to the early reports of image problems. In the early days, the focus offsets produced by changes in temperature, were only applied to the nominal reference filter, and not automatically corrected when a different filter was used. For large focus offsets, the instrument was shifted out of focus and this produced the field astigmatism image elonga-

tions. This problem is now fixed. Note that this “astigmatism” differs from that caused by elastic deformation of the mirror. Field astigmatism varies within the field whereas the “stress” astigmatism is constant. Of course, in some cases a combination of both effects could have been present.

### The Opto-Mechanical Contribution

All the tests were performed with the participation of the mechanic team and long, fruitful discussions took place with the team members. A first check was conducted on the lateral astatic pads after dismantling the mirror cell from the telescope. The mirror is kept laterally in position by a reference sphere in contact with the Cassegrain hole. Radial astatic levers maintain the mirror laterally by pushing or pulling, and no force is applied when the mirror is horizontal. All levers were found to be moving freely without mechanical stress. However, the reference sphere was found to be dirty on the northern side. The cause of this is thought to be cleaning of the mirror when it is inclined, allowing some of the Carbon Dioxide snow to fall into the Cassegrain hole, taking dust from the mirror surface with it.

The design of the mirror cell includes the facility to keep the mirror in a “park” position. In this case the mirror rests on three supports without the control of astatic levers. Three axial fixed points define the mirror orientation while the mirror is supported over the astatic levers under the control of pneumatic pressure. When the air pressure is removed, the mirror moves down by around 2 mm and the three axial fixed points move down within a spring tension device. The springs are used to keep the fixed points in contact with the

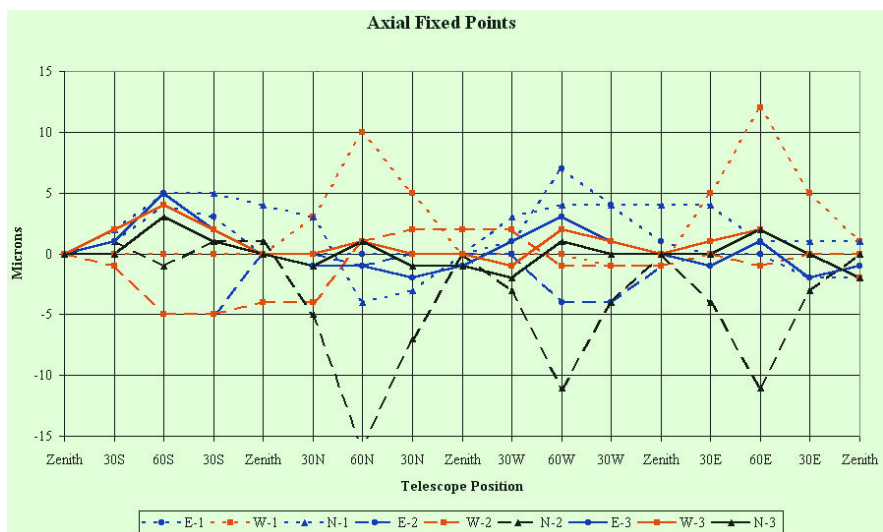


Figure 1: Behaviour of the axial fixed points with changes in telescope position. The measurements shown were made during three intervals: before the April tests (short dashed lines), during the June tests (long dashed lines) and after all tests (solid line).

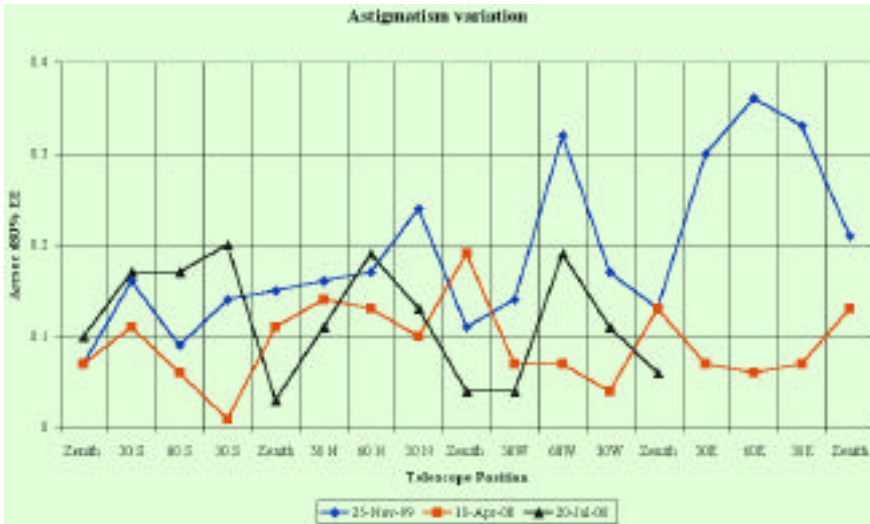


Figure 2: Variation of the astigmatism over the same range of telescope positions as Figure 1. The large deviation of the astigmatism for the east and west part of the cycle is clearly visible. Part of the last July sequence was not performed because of bad weather. The larger variations found during the last test night are due partially to a local thermal effect.

reference position with the correct applied force on zenith. The astatic levers are distributed around two rings. Two manual air pressure controllers distribute the pressure equally on all levers. Each unit delivers air pressure to one ring only. At the beginning of the observation, the telescope start-up operation includes the air pressure distribution on the mirror cell. The mirror raises until the mirror weight is in equilibrium with the astatic levels, assuming the correct positioning of the fixed points in contact with their respective references. Due to the lack of load cell, the force applied on the mirror is not known (it is a non-active optics). Departure on force distribution cannot be verified directly. The only part allowing access to the mirror position check are the three axial points, where linear gauges have been installed.

### A Summary of the Tests

At each telescope position during the measurement sequence, a check of both mirror position and the amount of aberration was made.

#### April 2000 Period

During this test period, the behaviour of the western fixed point was not correct for large inclinations towards the north and east. A correlation with an increase of astigmatism and triangular aberration terms was also identified. The three fixed points were checked during the re-aluminisation of the 2.2-m that took place on April 20. Effectively, the west point was found to be tilted with improper mechanical contact which increased the force of the springs. The effect was to raise the mir-

ror when the cosine astatic forces decreased. Therefore, the pad pushing against the mirror introduced astigmatism and a small triangular deformation.

#### June 2000 Period

After a complete overhaul of the three fixed points a new round of tests was performed. Now the northern fixed point showed a new pattern with a slight decrease of the applied force in inclined telescope positions. The spring tension had to be increased to obtain the correct force, both at zenith and at large inclination.

The last measurement of the axial fixed points showed the correct pattern, with a slight decrease for each inclined position, due to the decrease in the cosine component of the mirror weight.

#### July 2000 Period

A new check of the aberrations in the telescope was undertaken. The fixed points again showed the correct behaviour for the sequence of measurements. However, the spherical aberration term as well as those of the astigmatism increased "abnormally" at some telescope positions.

Figure 1 shows the range of movement in the axial fixed points over the full range of telescope position at different times. Figure 2 and 3 show the behaviour of the astigmatism and the triangular aberration during the different test periods.

#### The thermal contribution

"Unforeseen" aberrations appeared in July, and only temporarily. They are related to local thermal activity that acts to produce a wavefront deformation. In this case, "thermal aberration" would be a more correct term to describe what takes place. On this test night the cold temperature of the outside air was producing large local effects.

This effect is a good demonstration of the limitations that can exist in telescope imaging quality, not just from misalignment of the telescope (with mirror deformation in an improper cell design) but also from thermal convection.

The thermal convection can be separated in different components, such as the dome/tube seeing, dome/slit seeing, mirror seeing and local perturbations produced by extra warm sources.

The thermal conditions of each test night were different, with almost all except the last having the mirror colder than ambient air (by between zero and 2 degrees). Even so, the thermal effects were still negligible compared to the contribution of the axial fixed points to image degradation.

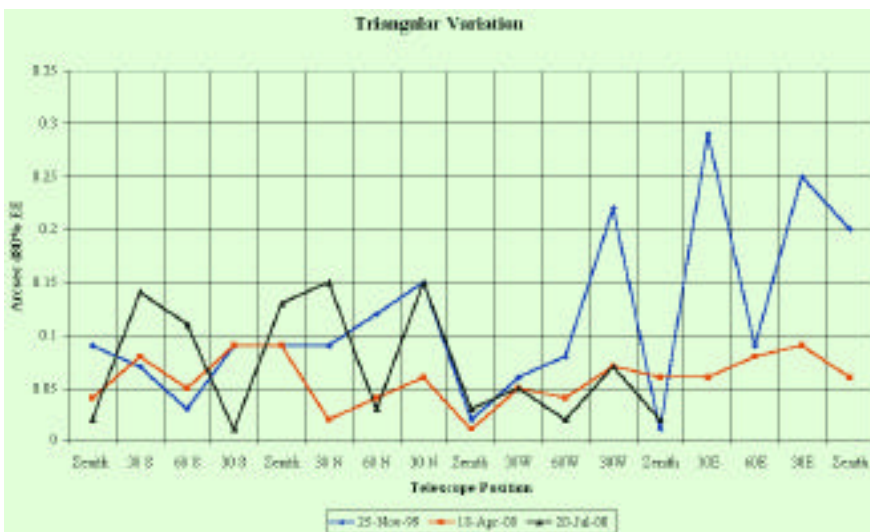


Figure 3: Variation of the triangular aberration over the same range of telescope positions. Again, the variations are large for the west and east part of the cycle before the April test. The thermal conditions of the last night (with a strong temperature decrease) produced a very unfavourable local convection effect on the mirror edge, thereby affecting the wavefront.

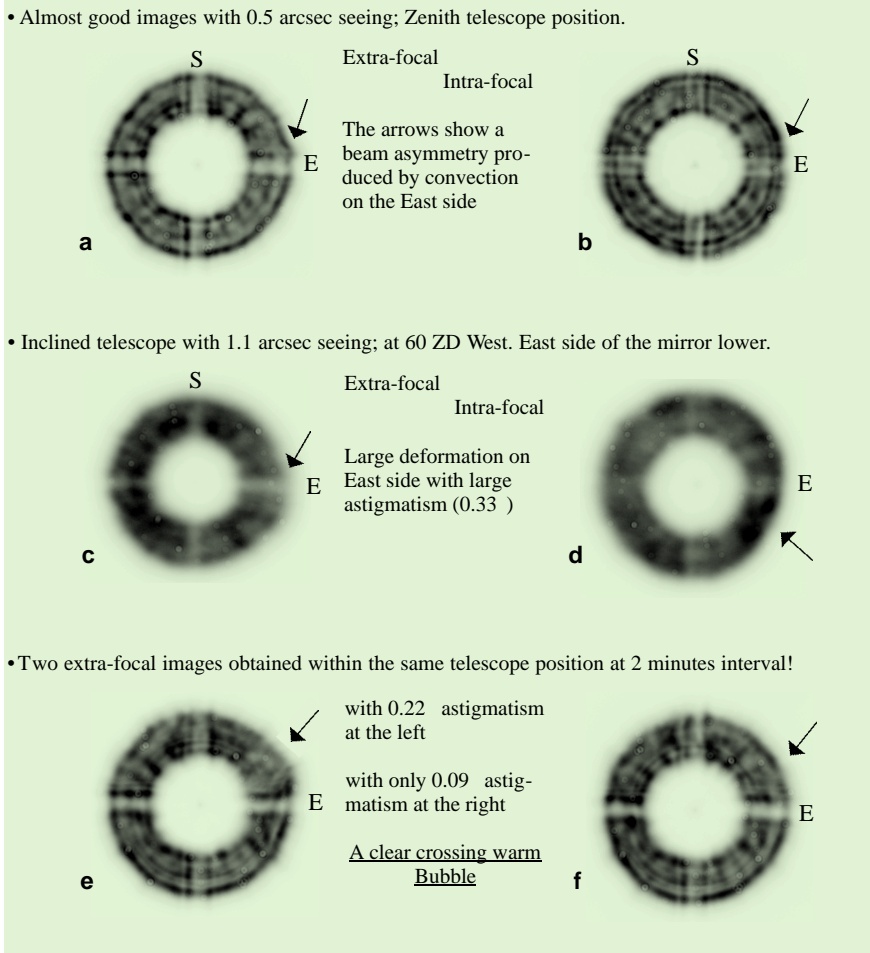


Figure 4: Thermal contribution to the image quality as seen in defocused images.

On the last night, however, the mirror was warmer by 1.5 degrees, with a corresponding degradation in the mirror seeing. The outside air temperature reached a low value of 4 degrees,

causing a larger gradient with the remaining warmth of the telescope delta pads. Figure 4 clearly shows how this local effect is visible in the defocused images. The figure also shows the dis-

tortion of the defocused images due to local thermal perturbations.

## Conclusion

Following the interventions performed up to and including July 2000, the telescope image quality remains good with several reports by observers as being very good. Under good external seeing conditions, it is possible to achieve sub-arcsec images, sometime approaching 0.5 arcsec. The image quality achieved with the WFI is as expected over a large part of the sky. Improvements could still be made to minimise the thermal contribution when colder temperatures are experienced. The best method (which is already in use on the 3.6-m and the NTT) would be to ventilate the main mirror with high-flux fans. A reduction in the mirror seeing, as well as local perturbations, could be achieved by blowing air across the mirror, from north to south.

The installation of load cells on the three axial fixed points will be also a forward step on the telescope improvement. The force delivered by each of the axial fixed points could be fine tuned, to reach a new minimising of the residual low astigmatism. The limit of the image quality will be then defined by the pixel size of the WFI.

## Acknowledgements

We are grateful to the mechanics team for the discussions and participation during all the steps of this study. The assistance of the Medium Size Telescope Team, in allowing regular test periods and operational help, was also essential to the success of the image quality improvement.

# NEWS from the NTT

## O. HAINAUT and the NTT Team

### A Motor-related Disaster

At the time this is being written, the NTT is running very nicely. While this is how the NTT is supposed to behave, it has not been the case during the last month. Indeed, on January 16, it was detected that one of the 4 main azimuth motors had died. The team immediately started to reconfigure the drive system to operate without that motor (in case of emergency, we can run on 2 motors only). During that process, a second motor died! We decided to stop the operation and shut down the telescope to investigate; indeed, while we can survive with 2 motors, we cannot afford to kill one per day. The two faulty

motors have been removed, our (single) spare installed, and the electronics started to perform a *complete* check of all the system driving the motors. In that process, it was discovered that a third motor presented some minor signs of damages.

The next step was to open one of the faulty motors to diagnose and, ideally, to repair it. For this purpose, we invaded the dome of the Schmidt telescope, which was de-commissioned some time ago. This large room has plenty of space, is very clean and equipped with a crane, making it the ideal place for disassembling the motors. The La Silla Mechanics, Electronics and NTT Team worked almost round-the-clock to open

the motor. This task is not as simple as it sounds: the motors are actually complete servo-drive units, including in a very compact design the motor itself, its water/glycol cooling system, the tachometer and the brake, the complete unit weighing 550 kg. Moreover, some special tools had to be manufactured; indeed, when the motors were delivered, it was not foreseen that they would ever have to be re-opened, and the assembly tools were left at the factory. To make the situation even more challenging, it occurred in January, which is right in the Chilean vacation period. La Silla was operated with a reduced staff. Eventually, the main motor coil was accessed, and we realised that



Figure 1: Dead motor in the Schmidt dome, ready for disassembly.

it was severely damaged: water had leaked on that coil over a long period of time, slowly building up a mixture of sulfate and carbon that eventually short-circuited the coil with its steel chassis. Unfortunately, even after cleaning this gunk out and restoring the connectors, the coils were still short-circuited, indicating some internal damages that could not be repaired on the spot. As we still had a motor missing for normal operation, we decided to open the spare altitude motor; while the mechanic parts are different, the coils are similar. The team, becoming expert in disassembling these motors, removed the coil from the altitude motor and placed it in the body of the azimuth motor in 24 hours only. The final rush was to re-assemble the azimuth motor and test it. I won't go into details in describing the atmosphere in the Schmidt dome when the motor started to spin; enough said that the satisfaction was palpable. The mechanics immediately re-installed the repaired motor in the telescope and adjusted it (a task that lasted till the early hours of the next day), so that the NTT electronics could immediately start the adjustments and tests. The following night, we were on the sky for a quick, but thorough test and commissioning of the new system. The NTT was back to life, after 12 nights lost for observations. This was the longest down-time ever for the NTT.

The cause of the short-circuit was obviously water. The main question is then to know where this water came from. The presence of glycol indicates that it was from a leak of the cooling system, not from condensation. The O-rings sealing the cooling pipes were found in perfect condition, so it seems they are not at the origin of the leak. A

careful examination of the upper part of the motor chassis revealed little specks of oxidation right where the cooling tubes are located, so we suspect that the water diffused through micro-porosity of the steel. The next step is now to maintain and repair the remaining motors, and to fix them so that this problem does not repeat itself in the future.

By re-arranging the schedule and using a 4-night technical run combined with a 2-night service observing run, we could perform the priority observations of all but one of the observation runs that had been lost.



Figure 2: The faulty coil removed from the motor; the brush on the right gives the scale of this 60 kg piece.

## Instruments

Since the previous report from the NTT, SOFI still had a few hick-ups related to its cryo-mechanics. The wheels, which suffer from the same problems as ISAAC on the VLT, will eventually be replaced by equivalent ones made of different material, hopefully solving the problem in a definitive way. In the mean time, the instrument control software has been modified to avoid the problem.

Asymmetric spectral lines have been reported by some of our observers using EMMI in Blue Medium Dispersion mode. This was tracked to a misalignment of the blue arm that has been corrected: the BLMD mode now provides perfectly symmetric lines. We still have to re-align the instrument for the dichroic mode. At the same time, the calibration of the long-slit unit used in medium dispersion spectroscopy has been checked and found quite accurate.

SUSI2's detector head has been replaced by a new model that will not cause any contamination of the chips, a problem that plagued SUSI2's early days. The detectors themselves have been baked and cleaned, and SUSI2 is now as good as new.

## Improvements

In addition to the upgrade of the control system to the 2000 release of the VLT software (which is extremely stable and reliable), new workstations have been installed. Visitors will appreciate the power of the HP Visualise B2000 and J2240 that are put at their disposal.

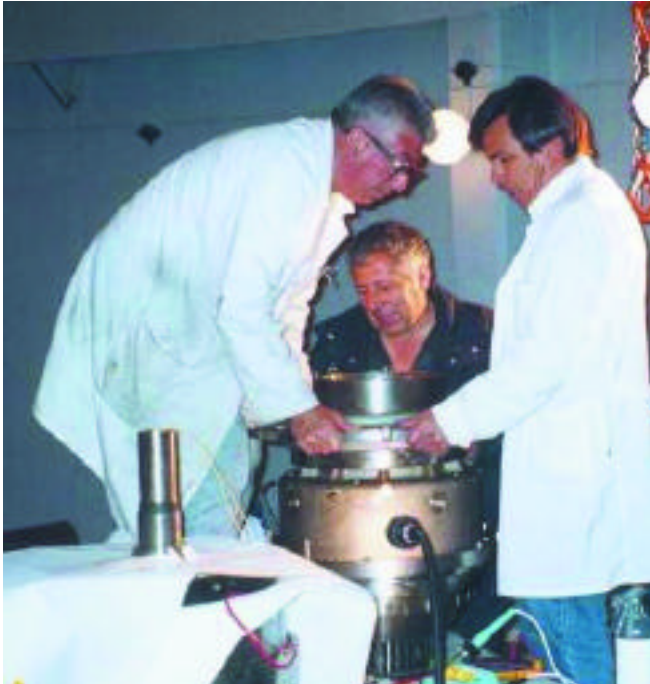


Figure 3: Final moments of the re-assembly of the motor.

We also installed a set of high-speed fans around the main mirror, to produce a constant artificial wind which disrupts

whose upper part is completely transparent to the wind. This provides an air-flow over the secondary mirror, and

the hot air cells that could form over the mirror. This strongly contributes to improve the image quality when there is no wind. The baffle of the secondary mirror has been changed for a light-weight, Kevlar and Carbon fibre structure that is optically equivalent to the former baffle, but

avoids the formation of a hot-air bubble that would introduce some aberrations. Another article in this issue of *The Messenger* describes these improvements and their results in more details.

## Staff

Since our last report, Ismo Kastinen and Hernan Nuñez (Telescope and Instrument Operators) have left the team; Ismo is now a Software Engineer at La Silla, and Hernan a TIO at the VLT. Gabriel Martin (TIO) is about to leave the NTT to work at the Magellan Observatory on Las Campanas as Instrument Specialist. Monica Castillo and Duncan Castex have joined the Team as TIO. There are also many changes in the astronomical staff: Vanessa Doublier (fellow) has left the Team, and Stephane Brilliant (fellow) is currently on his last shift at the NTT; both of them have been hired as staff astronomers at the VLT. Obviously, the NTT is an excellent training camp for Paranal! Malvina Billeres and Merieme Chadid have joined the NTT Team as fellows.

## 2p2 Team News

H. JONES

### Personnel Movements

In December we welcomed Emanuel Galliano to our team. Emanuel is a French student at ESO Chile who is already familiar with La Silla, through his previous work with the DENIS group. He will be working primarily on operations at the 2.2-m.

In February, however, we bade farewell to Emanuela Pompei after nearly two years with the team. Although Emanuela is leaving La Silla, she will remain with ESO in Chile, commencing work as a Staff Astronomer on Paranal in March. We wish her all the best in her move north.

### P2PP and BOB Now on the 2.2-m

In December, the final commissioning phase of the new operating software at the 2.2-m took place. This means that Wide Field Imager (WFI) observing programmes at the 2.2-m telescope are now performed using VLT Observing Software, with all pointing and exposure acquisitions controlled through Observation Blocks (OBs).

If you have upcoming Service Mode observations, then you will be contacted directly about the creation of OBs as

part of the Phase-2 preparations for your programme.

If you have an upcoming Visitor Mode WFI run, then you will need to familiarise yourself with the P2PP software. Specifically, you should know how to create and edit OBs in this environment, as this is what is used at the telescope. You should also be aware of the different types of WFI-specific templates available to build OBs, and plan your observations accordingly. Whether or not you choose to prepare your OBs in advance of coming to observe is up to you. If you already have experience with P2PP, you may wish to install the software at your home institute and create your OBs ahead of time. Otherwise it is better if you can create your OBs on the mountain. In this case, it is highly desirable that you arrive the day before your first night if this is at all possible. Allowing ample time for preparation plays a major part in the efficiency of the observing run.

Further information can be found at our 2.2-m P2PP/BOB web page, at [http://www.ls.eso.org/lasilla/Telescopes/2p2T/E2p2M/WFI/P2PP\\_BOB/](http://www.ls.eso.org/lasilla/Telescopes/2p2T/E2p2M/WFI/P2PP_BOB/). It contains links to the P2PPHome Page and the new WFI Templates Manual, which describes observing templates available for OB creation. The page also has instructions for installing and running the software at your home institute, including use of the WFI Instrument Package. As always, questions or comments can be directed to the 2p2 Team at any time ([2p2team@eso.org](mailto:2p2team@eso.org)).

### New CCD on the Danish 1.54-m

A new CCD was commissioned at the Danish 1.54-m in September by a team from the Copenhagen University Observatory. The new EEV/MAT CCD (2048 × 4096 pixels) replaces the old Loral 2048 × 2048 detector to bring about improvements on two fronts. First, the new device does not suffer from the same charge diffusion problem as the old CCD. This problem was thought to have been responsible for the consistently poorer seeing measured at this telescope compared to others. Second, the EEV CCD has half the read-out noise (3 e<sup>-</sup> rms) of the old device, and a much larger full-well.

However, the optics of DFOSC do not allow the full area of this large format device to be used. The region used suffers from some defects such as bad columns and charge traps, in a similar way to the Loral chip. The quantum efficiency of the EEV device is slightly less, peaking around 450 nm and declining steadily to the red. The parallel charge transfer efficiency shows no losses although there is a small but non-negligible loss in the serial direction due to trap in the serial register.

A full report on the characteristics of the device (by Anton Norup Sorensen of the Copenhagen University Observatory), is available from the 2p2 Team Web Page at <http://www.ls.eso.org/lasilla/Telescopes/2p2T/D1p5M/misc/tingo.ps>.

# Tunable Filters and Large Telescopes

H. JONES (ESO Chile), A. RENZINI (ESO Garching), P. ROSATI (ESO Garching) and W. SEIFERT (Landessternwarte, Heidelberg)

## Introduction

Traditionally, astronomy has relied upon filters with a fixed bandpass to select the wavelengths of the light allowed to reach the detector, thus allowing the astronomer to derive some colour information about the objects under study. In the optical, these filters are most often classical broadband UBVRI, or narrow passbands centred at the wavelengths of the common emission-line features, either at rest-frame or redshifted wavelengths.

Examples of the latter are becoming numerous, especially on the 8–10-m-class telescopes that make it possible to detect very faint, distant emission-line objects, even through narrow passbands. In this vein, Kurk et al. (2000) used FORS1 at the VLT with a 65-Å-wide filter at 3814 Å to image a  $z = 2.2$  radio galaxy, searching for nearby Ly-alpha detections at the same redshift. They detected around 50 such objects, collectively suggestive of strong clustering around the dominant radio galaxy. Moreover, they also found extended Ly-alpha emission ( $\sim 100$  kpc in extent) centred on the galaxy, adding further evidence to the possible scenario of protocluster formation.

Steidel et al. (2000) used an 80-Å-wide filter on Keck to search for Ly-alpha emitters at  $z = 3.09$ , the redshift of a prominent peak in the redshift distribution of their original sample of broad-band selected Lyman-break galaxies. This took the number of galaxies associated with the peak from 24 to 162, a gain of almost a factor of 7, thereby demonstrating the power of narrow-band observations in the detailed mapping of large-scale structures at high redshift. They also found extended ( $\sim 100$  kpc) Ly-alpha emitting “blobs”, that again may point to incipient cluster formation at these redshifts.

Kudritzki et al. (2000) used FORS1 at the VLT for the spectroscopic follow-up to a sample of emission-line objects, identified by narrow-band imaging in the field of the Virgo cluster. The expectation was to confirm them as intra-cluster planetary nebulae, given their detection with a [OII] ( $\lambda = 5007$  Å) filter. As it turned out, however, the narrow passband was equally good at revealing Ly-alpha-emitting objects at  $z \sim 3.1$ , and nine were found.

In some of the above examples, a filter with the desired passband luckily matched the project requirements; in others, one had to be designed with a specific target in mind. However, studies of this kind (as well as many others in the local universe), would clearly benefit given the use of a passband that can be easily tuned both in its width and central wavelength, over the full optical range. The use of (Wide-band) Tunable Filter (WTF) instruments at the Anglo-Australian and William Herschel Telescopes (Bland-Hawthorn & Jones 1998a,b) in the past five years has indeed seen a very broad range of astrophysical applications. At low redshifts, science undertaken with these instruments includes studies of brown dwarf atmospheric variability (Tinney & Tolley 1999), and the identification of optical counterparts to Galactic X-ray sources (Deutsch, Margon & Bland-Hawthorn 1998). High-redshift science has included estimates of the cosmic star-formation history (Jones & Bland-Hawthorn 2001), identification of galaxy clustering around high-redshift QSOs (Baker et al. 2001), deep imaging of jet-cloud interactions in powerful radio galaxies (Tadhunter et al. 2000), and the detection of a large ionised nebula around a nearby QSO (Shopbell et al. 2000). Figure 1 shows a section of field from a tunable filter survey on the Anglo-Australian Telescope (Jones & Bland-Hawthorn 2001), for distant

emission-line galaxies. Figure 2 shows example scans and scanning narrow-band “spectra” obtained with the tunable filter for some of the same objects.

Understandably, there is growing interest in the role that tunable filters can play in the instruments currently under design and construction for the new generation of large telescopes. These include tunable filters in instruments for the GranTeCan (OSIRIS: Cepa et al. 2000) and SOAR telescopes (Cecil 2000), among others under consideration. The technique is all the more powerful when the focal reducing instruments in which they are placed have the capability for both tunable imaging and multi-object spectroscopy, since the two modes are complementary. In this article we review tunable imaging and the future role it could potentially play at the VLT. We also briefly mention the wide range of science, both Galactic and extragalactic, that could be undertaken with a tunable filter on an 8-m-class telescope.

## Making a Filter Tunable

There are many ways of making a filter with tuning capability, and consequently, many types of tunable filter. These include those using birefringent materials (such as the Lyot, Solc and acousto-optic tunable filters), more traditional interferometers such as the Michelson and Fabry-Perot, and even liquid crystal tunable filters. We will not describe details of each technology here, but instead refer the interested reader to Bland-Hawthorn (2000), who discusses the merits of each for tunable imaging. While all have advantages and limitations, in the end it is the stringent demands of night-time astronomy that dictate which are feasible. For astronomical applications, the ideal filter should have high peak transmission, a broad (rectangular) profile, and should be large enough to admit a generous beam size. It should also be of good imaging quality, produce a stable and reproducible passband, and cover a large range of wavelengths, to name just the major requirements.

Of all the possibilities, it is the Fabry-Perot interferometer that has been the popular choice of astronomers for three-dimensional spectral imaging. This is because they are readily available on a commercial basis and make use of well-established technology. Astronomical applications of these instruments have included studies of extended diffuse nebulae (e.g. Haffner, Reynolds & Tufte 1999) and obtaining

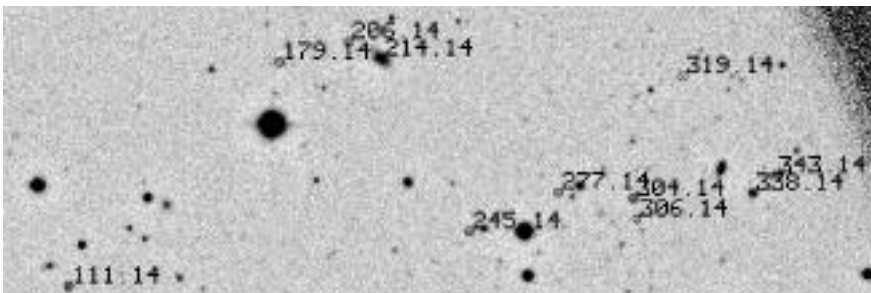


Figure 1: A section of field (approximately  $6 \times 2$  arcmin with north up, east left) from the emission-line galaxy survey of Jones & Bland-Hawthorn (2001). The numbers next to each emission-line candidate are object identifications.

kinematic information (such as line widths and radial velocities) on nearby disk galaxies (e.g. Amram and Östlin in this issue, p. 31; Laval et al. 1987; Cecil 1989; Veilleux, Bland-Hawthorn & Cecil 1997; Shopbell & Bland-Hawthorn 1998). The Fabry-Perot systems employed have traditionally used narrow wavelength coverage and high spectral resolutions (resolving powers  $R$  1500).

There are two problems to be overcome in the adaptation of a Fabry-Perot interferometer to tunable imaging. First, it must work at sufficiently low spectral resolution (in other words, narrow plate spacing) that scanning in spectral steps over larger ranges of wavelength is feasible. Second, the filter coatings must be optimised over a large range of wavelengths. Traditionally, Fabry-Perots have had neither the wavelength coverage nor the ability to work at such small plate spacing.

### Fabry-Perot Tunable Filters

It is a little more than one hundred years since Charles Fabry and Alfred Perot first highlighted the potential of an interference device producing fringes from two parallel silvered plates (Perot & Fabry 1899; Fabry & Perot 1901). Modern Fabry-Perot interferometers consist of two parallel glass plates held a small distance apart, such that constructive interference of light between the plates causes only specific wavelengths to be transmitted. However, with typical plate spacings in the range 20 to 500 microns, Fabry-Perots for astronomical work have been confined to high orders of interference (50 to 2000), thereby giving rise to the high resolving powers mentioned earlier.

Tunable filters differ from conventional Fabry-Perot devices in two novel but important ways. First, the plates are operated at much smaller plate spacings than the Fabry-Perot instruments so far used for astronomy. The effect of this is to widen the central interference region of the chosen wavelength. A conventional Fabry-Perot, with a plate spacing of many tens or even hundreds of microns, presents an interference region as a narrow ring on the sky, with very small area (Fig. 3a). A tunable filter, with a plate spacing of no more than a few microns, aims to provide a broadened central interference region, known as the Jacquinot spot (Fig. 3b). The latter is more useful for survey work, where one seeks a common wavelength transmitted across the full field and where lower spectral resolutions are desired.

The second way in which a tunable filter differs from a conventional Fabry-Perot is in its ability to access a much wider range of plate spacings. Conventional devices are most commonly used to scan through a relatively small range of wavelengths around a single spectral feature. However, a tunable fil-

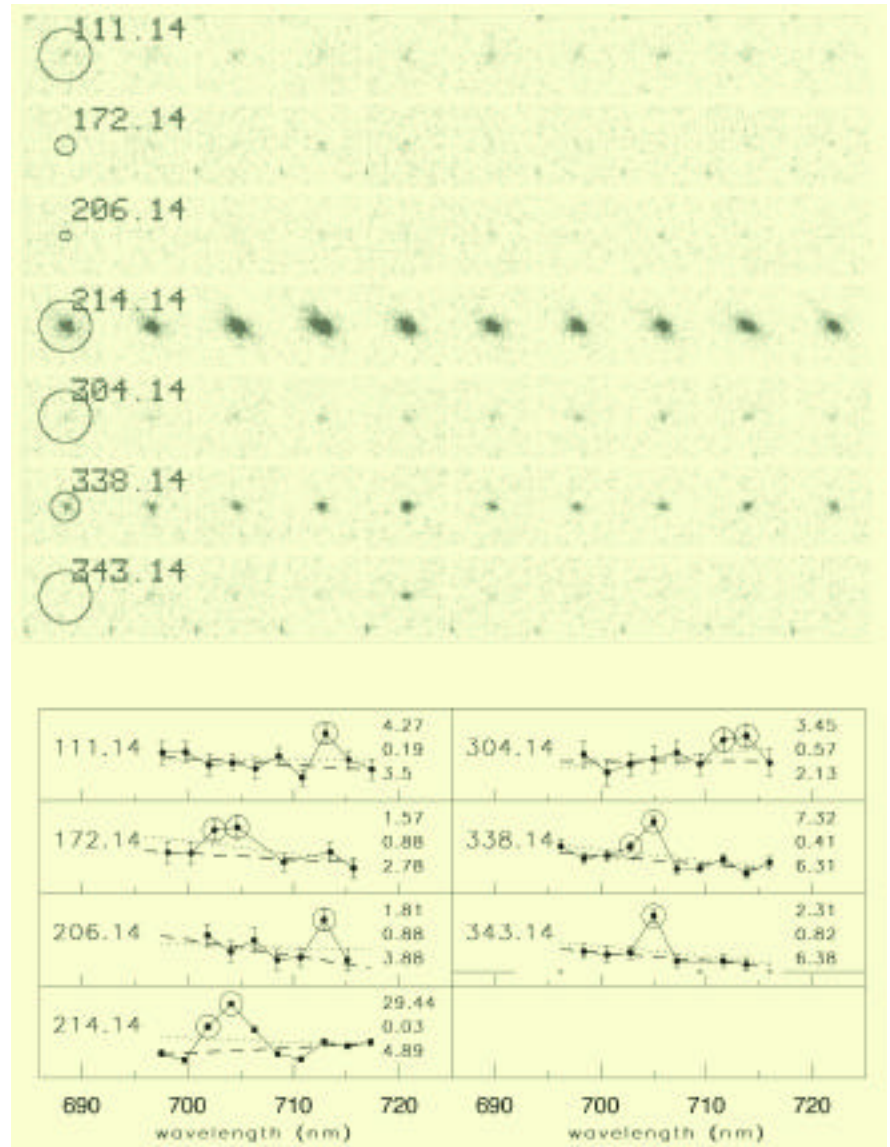


Figure 2: (Top) Individual object scans for some of the same candidates as in Figure 1. Individual images are 9 arcsec on a side with north at top, east to the left. Circles denote aperture size.

(Bottom) Spectral flux measurement for the same galaxies. Both preliminary (dotted line) and final (solid line) continuum fits are shown. Numbers shown on the right are flux ( $\times 10^{-16}$  ergs/s/cm $^2$ ), a star-galaxy classification parameter and deviation of the line detection in  $\sigma$ . Deviant points (excluded from the final continuum fit) are indicated by circles. The zero flux level is shown by the horizontal tickmarks (where present) and non-detections are represented on this level by crosses. Galaxy 214.14 has independently been found to have emission in [OII] by Ellis et al. (1996); the emission we see here is H-alpha and [NII].

ter, aiming to access as broad a tunable range as is possible, needs to access a much wider range of plate settings. This is made possible by having a stack of piezo-electric transducers (PZTs) to control plate spacing, instead of the usual single-layer. These structural differences between a tunable filter and a conventional Fabry-Perot contribute to the different types of data that are obtained with each instrument:

(i) conventional Fabry-Perots can be used to obtain a high-resolution narrow-range spectrum at each pixel position over a wide field (Fig. 3i),

(ii) conventional Fabry-Perots can also be used to obtain a single spectrum of a diffuse source which fills a large fraction of the aperture (from one

or more deep frames at the same etalon spacing, Fig 3ii), and,

(iii) tunable filters can obtain a sequence of monochromatic images within a field defined by the Jacquinot spot, (Fig. 3iii).

Atherton & Reay (1981) were the first to suggest the possibilities of a Fabry-Perot as a tunable imager. However, the technology available at the time was not sufficient for precise control of the plates over a such wide range of spacings, and suitable coatings were not very good by the standards of today (see Pietraszewski 2000 for descriptions of the current state of the art in Fabry-Perot technology). In the mid-1990s, J. Bland-Hawthorn (AAO) revisited the tunable filter concept by

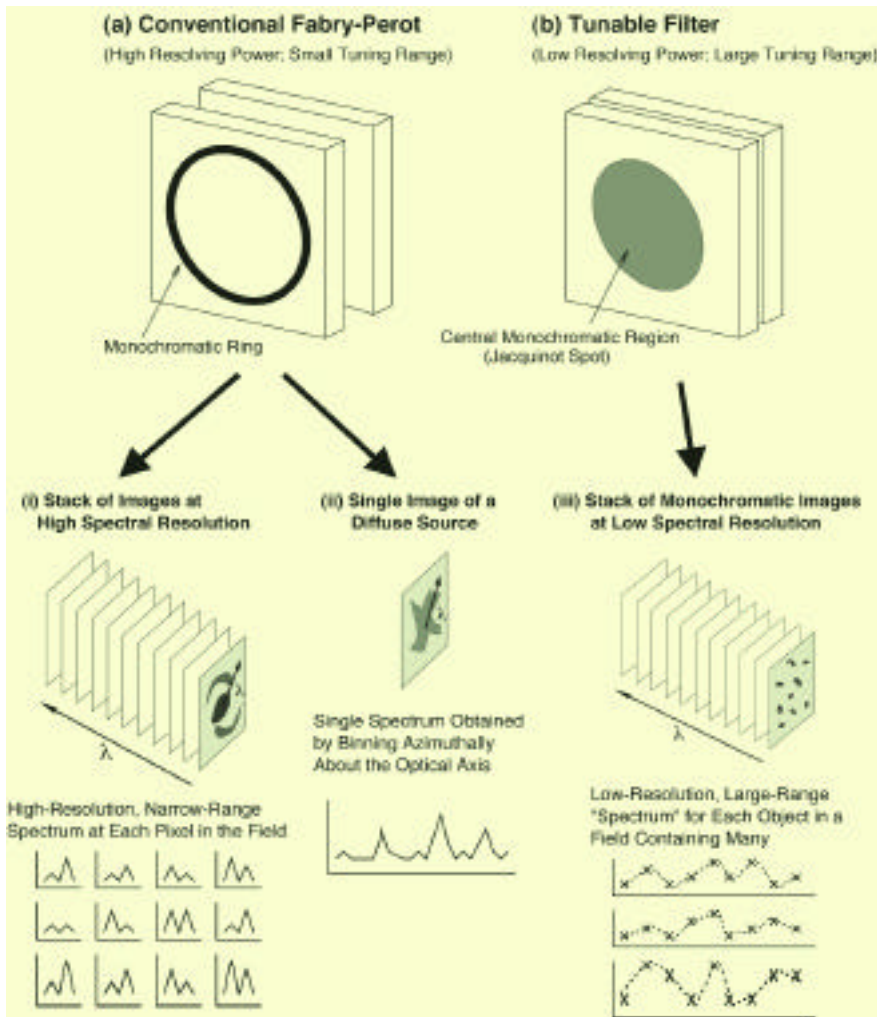


Figure 3: Different modes of Fabry-Perot use in the case of both (a) conventional instruments, and (b) tunable filters.

having an old, disused conventional Fabry-Perot, refitted with stacked PZTs, then repolished and recoated for the range 6500 Å to 1 micron. The result was the first TAURUS Tunable Filter (TTF; Bland-Hawthorn & Jones 1998a,b) implemented at the Anglo-Australian Telescope (AAT). Two years later, an instrument coated for the blue (3700 to 6500 Å) was commissioned. These instruments are operated at the Cassegrain focus of the AAT, and together have been used extensively. The instruments can also be used in conjunction with a CCD charge-shuffling mode, that allows repeated multi-band imaging on different parts of the CCD frame, before it is read out (Bland-Hawthorn & Jones 1998a, b). More details of the different features of TTF can be found at <http://www.aao.gov.au/local/www/jbh/ttf/>. The advantages of using a Fabry-Perot for tunable imaging has also been recognised by other groups (e.g. Thimm et al 1994, Meisenheimer et al. 1997).

How does one set about tuning a passband to a specific width and placement, when all one is changing is the spacing between the plates? As Fig-

ure 4 shows, the answer lies in the nature of the transmission profile of the Fabry-Perot, and the different effect of making small and large adjustments. Figure 4a shows the set of blocking filters used with the red TTF. These are necessary to block the light of unwanted orders and make excellent intermediate-band filters in their own right, given their placement between the brightest parts of the night-sky background. Suppose we wanted to scan around H-alpha at 6563 Å. First we would put the R<sub>0</sub> blocking filter in place (Fig. 4a, solid line). Then we would set the spacing of the plates according to the desired width of our passband. Figure 4b shows that if we set the plates to 8 or 10 microns, we get a very narrow profile (at orders 24 or 30 respectively); if we set the plates to just 2 or 4 microns we get a much wider band (orders 6 or 12). If we then wanted to scan the passband, we would adjust the spacing between the plates by small amounts, thereby shifting the chosen order one way or the other in wavelength. The dotted profiles in the lower panel of Figure 4b show the effect of changing 2 microns slightly to 1.98, 1.96 and 1.94 microns. Note that the images deliv-

ered by a tunable filter are not strictly monochromatic, but shift slightly to the blue as one moves from the location of the optical axis on the image, to the edge. This phase effect is a natural consequence of interference between two surfaces and easily characterised through the cosine of the off-axis angle (at the etalon). The red TTF shifts about 18 Å at a distance of about 5 arcmin from the optical axis, as measured on the sky. The phase effect is not normally a problem for most applications, especially if the objects of interest are compact sources such as distant galaxies and stars.

### A Tunable Filter versus Many Narrow-band Filters

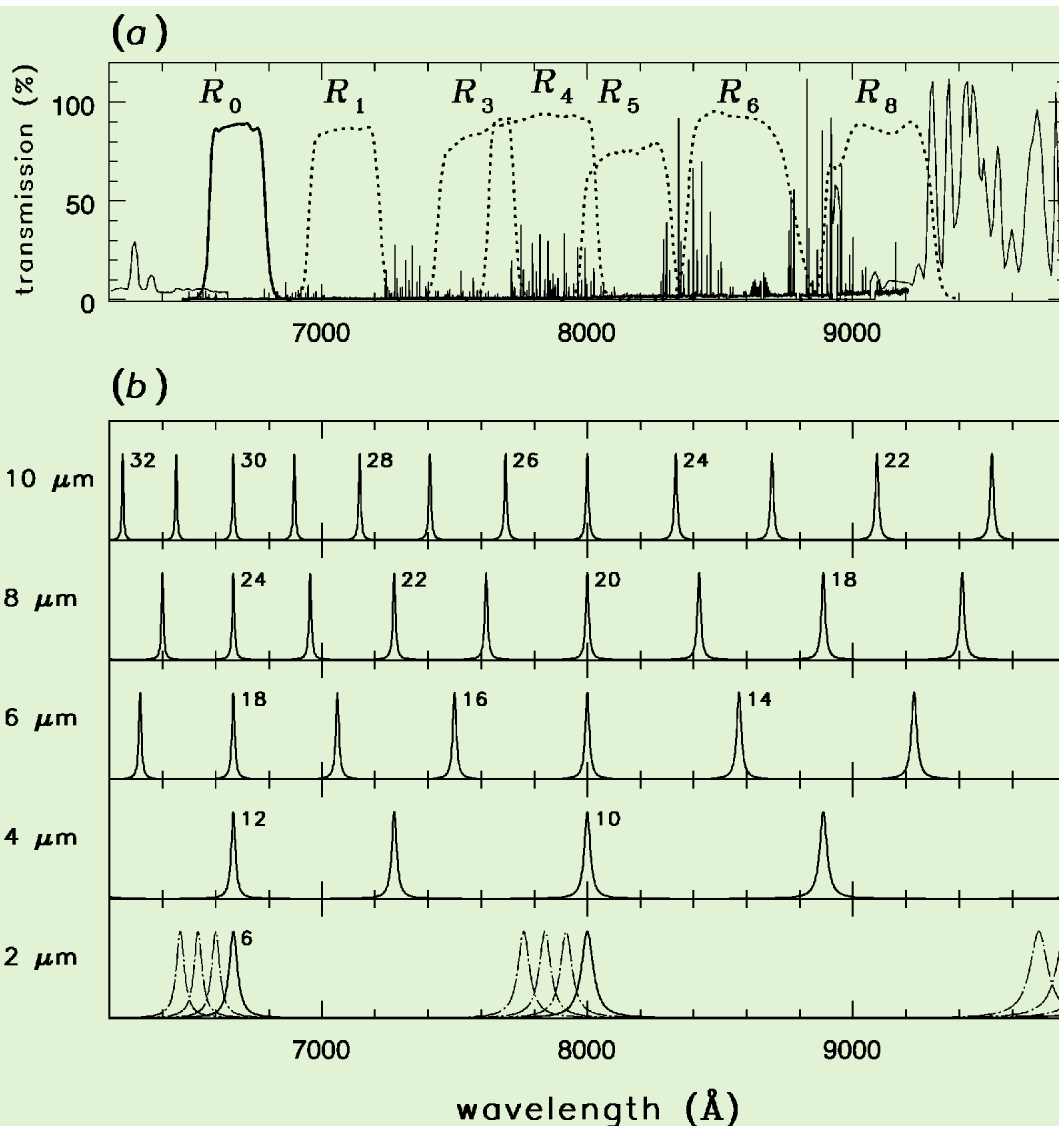
Is a tunable filter any better than simply having a large set of filters? With a Fabry-Perot tunable filter it is possible to control both the width and placement of the bandpass. The only restriction on placement is that it must lie within one of the order-sorting filters. For example, the red TTF on the AAT can select a bandpass of between 6 to 60 Å in any of the 7 order-sorting filters that collectively cover 2300 Å in the 6500 Å to 1 micron range of the device.

With a set of fixed filters one is stuck with a predetermined width and placement for the bandpass. Tilt-tuning might be considered an option but this quickly broadens and degrades the passband, in the sense that peak transmission is lowered and the profile skewed. Furthermore, such tilt tuning only allows adjustment to the blue. The inability to set the bandpass means one cannot optimise spectral resolution, nor background level, nor central wavelength nor sampling (in the case of scans). The ability to tune and optimise is critical to projects with (i) objects at arbitrary redshift, (ii) background-limited observations, and (iii) objects with a specific spectral feature in mind. These make up the majority of front-line narrow-band observing, since much has already been done in the way of imaging bright objects at common spectral features. Furthermore, the exact optical characteristics of individual filters will vary slightly from filter to filter, implying inhomogeneities which will need to be dealt with on a filter-by-filter basis. This limits the ability to do precise differential imaging between two bands – a common application in both stellar and extragalactic work.

### Reducing Tunable Filter Data

There is often the perception that Fabry-Perot interferometers produce data sets that are difficult for first-time users to understand and reduce. This is not true in the special case of tunable filters, as the variety of published results from the AAT and WHT

Figure 4:  
 (a) Wavelength region covered by the red TTF at the AAT, showing the location of the intermediate blocking filters with respect to bands of OH night-sky emission. (b) Transmission profile of the tunable filter plotted on the same scale, as a function of changing plate separation (left). Even-numbered orders are indicated. The dotted lines in the lower panel show the effect of changing the plate spacing to 1.98, 1.96 and 1.94  $\mu\text{m}$ .



show. Conventional Fabry-Perots work at much higher resolving powers and so when they are used to map kinematics in nearby galaxies, it requires precise mapping of the wavelength change across the field, so that a 3D-spectral cube can be constructed and subsequently transformed into a 2D map of velocities. However, tunable filter data are typically concerned only with scanning surveys of small point-like sources such as stars or distant galaxies. This requires nothing more than the detection, matching and photometry of each object on each frame – routine steps in any imaging survey, with or without a tunable filter. There is still a change in wavelength across the field of the tunable filter, but the lower resolving power makes this a less dramatic effect in terms of the broader width of the transmitting band-pass.

Tunable filter data from the AAT have been reduced with scripts utilising both the FOCAS (Valdes 1993) and SExtractor (Bertin & Arnouts 1996) packages for the object detection. One of us (Jones) has written a collection of IRAF

tasks (TFred) offering a range of tools to treat tunable filter data in IRAF. A more comprehensive treatment is given in Jones, Shopbell & Bland-Hawthorn (2001), where approaches to the reduction of Fabry-Perot tunable filter photometry are described.

### Tunable Filters and the VLT

There is currently no tunable filter capability on the VLT, and (in the short-term at least), neither on 8–10-m-class telescopes elsewhere. It is therefore worthwhile to contemplate if and how it might be possible to implement a tunable filter at the VLT. While a detailed technical, cost and manpower study remains to be done, we have investigated the main parameters of a possible incorporation of a tunable filter into the FORS2 focal reducer.

The largest commercially available tunable filter which could be fitted into either of the FORS instruments has a free aperture of 116 mm. The mechanical size of such a unit (sealed to minimise thermal/environmental influences) is 200 mm in diameter and

about 135 mm in height (as measured along the optical axis). This space could be accommodated in the collimated beam of FORS2 if the upper of the two grism wheels were dismounted. Nevertheless, the full spectroscopic capability of FORS2 is preserved, albeit with more frequent grism exchanges. The FORS2 echelle mode would be lost, although it would be possible to re-install the corresponding gratings in FORS1. Most importantly, no major mechanical hardware modifications would be necessary to effect the implementation. The control electronics needed to operate the tunable filter are delivered by industry. However, to allow for efficient use of the filter by the observer, a full integration into the GUI of the instrument would be needed.

As the free aperture of the tunable filters is slightly smaller than that needed to cover the full FORS field of view, a vignetting of 7.5 % occurs at the corners of the detector, preserving an unvignetted central field of 4.8 arcmin diameter. The blue shift of the filter transmission at the edge of the unvignetted field is only a fraction of the transmis-

sion profile width and therefore not a problem for most applications. For the lowest resolution, ordinary broad-band filters could be used as blocking filters. Additional filters needed to work at higher orders could be placed in the two interference filter wheels in front of the detector. The optimum passband for such filters is slightly less than the free spectral range at the highest resolving powers envisaged for use.

The useful wavelength range of the tunable filter is largely arbitrary but needs to be decided at the time of manufacture, as it is governed by the design (and resulting performance) of the etalon coating. For example, the two tunable filters in use at the AAT individually cover 3700–6500 Å and 6500 Å–1 micron. With a device in FORS, spectral resolutions achievable at 370 nm for example, would range from 330 to 1350, while at 650 nm would encompass 180 to 720. Such resolutions assume a variation of the spacing between the etalon plates from 2 to 8 micron, which can be achieved through stacked piezo-electric transducers. The tunable filter has a high efficiency comparable or even superior to common narrow-band filters.

The approach of using FORS2 to furnish the VLT with a tunable filter carries both pros and cons. On the one hand there is the relatively small effort compared to that of building an entirely new instrument, and the extension of the scientific uses of FORS2 following the commencement of VIMOS. On the other there is the need to remove one of the grism wheels to make the space. Eliminating one grism wheel will make for increased manual intervention in the exchange of grisms if one wants to preserve all the filter/grism combinations presently available. Clearly, the relative weight of these different arguments needs to be evaluated before deciding how to proceed.

### Potential Science on 8-m-class Telescopes

Scientific applications of a tunable filter at an 8-m telescope span an extremely wide range, potentially satisfying the needs of what is a very diverse user community. Several such applications were described at the beginning of this article. Here, we mention a few more possibilities. At the high limit of spectral resolution ( $R \sim 1500$ ) it may be possible to probe the internal dynamics of most kinds of emission-line nebulae and relatively nearby galaxies, along with that of QSO and radio galaxy environments. At lower resolutions ( $R \sim 150$ ), most (but not all) applications will concern the distant universe. For example, high-redshift clusters of galaxies are usually found either in deep X-ray or infrared surveys, with cluster

members being identified relatively easily through association with the 'red sequence' of passively evolving ellipticals. With such methods, however, spirals and star-forming galaxies that may also be cluster members are much more difficult to identify, given their broad range of colours, which can sometimes act to make them indistinguishable from foreground or background galaxies. However, tuning the tunable filter to a suitable emission line at the cluster redshift easily permits identification of these late-type galaxies.

Mapping the large-scale structure out to  $z \sim 5$  is one of the main goals within reach of the current generation of large telescopes and their instruments. The pilot experiment by Steidel et al. (2000) clearly demonstrates the advantages of narrow-band detection for this kind of work. Indeed, tuning the filter to the redshift peaks found through future Lyman-break galaxy surveys will expand the number of galaxies associated with these large-scale features many times over. Multi-object spectroscopy will further complement this, by determining the dynamics of sheets, filaments, and proto-clusters.

As the new VLT instrument VIMOS comes into operation, it becomes necessary to re-assess the role of the two FORS instruments, since the former will outperform the FORSes in many of their current applications. An upgrade plan for the two FORS instruments is therefore under study at ESO, including the red-optimisation of the CCDs on FORS2, which is planned for later in the year. Installing a tunable filter on FORS2 is another possibility for consideration, and in this article we have illustrated some of the scientific advantages and a possible technical implementation. The VLT also currently lacks an efficient UV imager, and indeed another upgrade under consideration concerns the UV optimisation of FORS1, all the way to the atmospheric cutoff. Together, these upgrades would reconstitute new scientific utility to the FORS instruments, while significantly expanding the capabilities of the VLT overall.

### References

Amram P. and Östlin G., 2001, *The Messenger* **103**, p. 31.  
 Atherton, P. D., Reay, N. K. 1981, *MNRAS* **197**, 507.  
 Baker, J. C., Hunstead, R. W., Bremer, M. N., Bland-Hawthorn, J., Athreya, R. A., Barr, J. 2001, *AJ*, in press.  
 Bertin, E., Arnouts, S. 1996, *A&A* **117**, 393.  
 Bland-Hawthorn, J., Jones, D. H. 1998a, *PASA*, **15**, 44.  
 Bland-Hawthorn, J., Jones, D. H. 1998b, in "Optical Astronomical Instrumentation", Proc SPIE **3355**, ed. S. D'Odorico, 855.  
 Bland-Hawthorn, J. 2000, in "Imaging the

Universe in Three Dimensions", ASP Conf. Series 195, eds. W. van Breugel and J. Bland-Hawthorn, 34.  
 Cecil, G. 1989, in "Extranuclear Activity in Galaxies", eds. E. J. A. Meurs and R. A. E. Fosbury, (ESO: Garching bei München, Germany).  
 Cecil, G. 2000, in "Optical and IR Telescope Instrumentation and Detectors", Proc SPIE 4008, eds. M. Iye and A. F. M. Moorwood, 83.  
 Cepa, J., Aguiar, M., Escalera, V. G., Gonzalez-Serrano, I., Joven, E., Peraza, L., Rasilla, J. L., Rodriguez, L. F., Gonzalez, J. J., Cobos, F. J., Sanchez, B., Tejada, C., Bland-Hawthorn, J., Militello, C., Rosa, F., 2000 in "Optical and IR Telescope Instrumentation and Detectors", Proc SPIE 4008, eds. M. Iye and A. F. M. Moorwood, 623.  
 Deutsch, E. W., Margon, B., Bland-Hawthorn, J. 1998, *PASP* **110**, 912.  
 Ellis, R. S., Colless, M., Broadhurst, T., Heyl, J., Glazebrook, K. 1996, *MNRAS* **280**, 235.  
 Fabry, C., Perot, A. 1901, *ApJ* **13**, 265.  
 Haffner, L. M., Reynolds, R. J., Tufte, S. L. 1999, *ApJ*, **523**, 223.  
 Jones, D. H., Bland-Hawthorn, J. 2001, *ApJ*, in press.  
 Jones, D. H., Shoppell, P. L., Bland-Hawthorn, J. 2001, *MNRAS*, submitted (see [http://sc6.sc.eso.org/~hjones/WWWpubl/detect\\_meas.ps.gz](http://sc6.sc.eso.org/~hjones/WWWpubl/detect_meas.ps.gz)).  
 Kudritzki, R.-P., Mendez, R. H., Feldmeier, J. J., Ciardullo, R., Jacoby, G. H., Freeman, K. C., Arnaboldi, M., Capaccioli, M., Gerhard, O., Ford, H. C. 2000, *ApJ*, **536**, 19.  
 Kurk, J. D., Rottgering, H. J. A., Pentericci, L., Miley, G. K., van Breugel, W., Carilli, C. L., Ford, H., Heckman, T., McCarthy, P., Moorwood, A. 2000, *A&A*, **358**, L1.  
 Laval, A., Boulesteix, J., Georgelin, Y. P., Georgelin, Y. M., Marcelin, M. 1987, *A&A*, **175**, 199.  
 Meisenheimer K., Beckwith, S., Fockenbrock, R., Fried, J., Hippelein, H., Hopp, U., Leinert, Ch., Roeser, H.-J., Thommes, E., Wolf, C. 1997, in "The Early Universe with the VLT", (Springer: Berlin), 165.  
 Perot, A. and Fabry, C. 1899, *ApJ* **9**, 87.  
 Pietraszewski, K. A. R. B. 2000, in "Imaging the Universe in Three Dimensions", ASP Conf. Series 195, eds. W. van Breugel and J. Bland-Hawthorn, 591.  
 Shoppell, P. L., Bland-Hawthorn, J. 1998, *ApJ* **493**, 129.  
 Shoppell, P. L., Veilleux, S., Bland-Hawthorn, J. 2000, in "Imaging the Universe in Three Dimensions", ASP Conf. Series 195, eds. W. van Breugel and J. Bland-Hawthorn, 404.  
 Steidel, C.C., Adelberger, K.L., Shapley, A.E., Pettini, M., Dickinson, M., Giavalisco, M. 2000, *ApJ*, **532**, 170.  
 Tadhunter, C., Villar-Martin, M., Morganti, R. 2000, in "Imaging the Universe in Three Dimensions", ASP Conf. Series 195, eds. W. van Breugel and J. Bland-Hawthorn, 284.  
 Thimm, G. J., Roser, H.-J., Hippelein, H., Meisenheimer, K. 1994, *A&A* **285**, 785.  
 Tinney, C. G., Tolley, A. J. 1999, *MNRAS* **304**, 119.  
 Valdes, F. 1993, "FOCAS User's Guide", NOAO.  
 Veilleux, S., Bland-Hawthorn, J., Cecil, G. 1999, *AJ* **118**, 2108.

## Seeing the Light Through the Dark *(Continued from page 1)*

no dipole moment and cannot produce a readily detectable signal under the conditions that characterise cold, dark clouds. The traditional methods used to derive the basic physical properties of such molecular clouds therefore make use of observations of trace  $H_2$  surrogates, namely those rare molecules with sufficient dipole moments to be easily detected by radio spectroscopic techniques (Lada 1996), and interstellar dust, whose thermal emission can be detected by radio continuum techniques (e.g., André et al. 2000). However, the interpretation of results derived from these methods is not always straightforward (e.g., Alves, Lada, & Lada 1999; Chandler & Richer 2000). Several poorly constrained effects inherent in these techniques (e.g., deviations from local thermodynamic equilibrium, opacity variations, chemical evolution, small-scale structure, depletion of molecules, unknown emissivity properties of the dust, unknown dust temperature) make the construction of an unambiguous picture of the physical structure of these objects a very difficult task. There is then a need for a less complicated and more robust tracer of  $H_2$  to access not only the physical structure of these objects but also to accurately calibrate molecular abundances and dust emissivity inside these clouds. The deployment of sensitive, large-format infrared array cameras on large telescopes, however, has fulfilled

this need by enabling the direct measurement of the dust extinction toward thousands of individual background stars observed through a molecular cloud. Such measurements are free from the complications that plague molecular-line or dust-emission data and enable detailed maps of cloud structure to be constructed.

### 2. The Method and Results So Far

The most straightforward and reliable way to measure molecular cloud structure is to measure dust extinction of background starlight. We have developed a new powerful technique for measuring and mapping the distribution of dust through a molecular cloud using data obtained in large-scale, multi-wavelength, infrared imaging surveys. This method combines measurements of near-infrared colour excess to directly measure extinctions and map the dust column density distribution through a cloud (see Fig. 2). *It is the most straightforward and unambiguous way of determining the density structure in dark molecular clouds.* Moreover, the measurements can be made at significantly higher angular resolutions and substantially greater optical depths than previously thought possible. We have conclusively demonstrated the efficacy of this technique with our study of the dark cloud complex IC

5146 (Lada et al. 1994, Lada et al. 1999), L 977 (Alves et al. 1998), and Barnard 68 (Alves, Lada, & Lada 2001), where we detected nearly 7000 infrared sources background to these clouds and produced detailed maps of the extinction across the cloud to optical depths and spatial resolution an order of magnitude higher than previously possible ( $A_V \sim 40$  magnitudes, spatial resolution  $\sim 10$  arcsec).

We have used our extinction observations to measure the masses, density structure, extinction laws, and distances to these objects. We found the radial density profiles of filamentary clouds (IC 5146 and L 977) to be well behaved and smoothly falling with a power-law index of  $\alpha = -2$ , significantly shallower than predicted by early theoretical calculations of Ostriker (1964) ( $\alpha = -4$ ). Moreover, because we are using pencil beam measurements of dust column density along the line of sight to background stars, we were able to demonstrate that the small-scale structure of the clouds is surprisingly smooth with random density fluctuations ( $\sigma_{A_V} / A_V$ ) present at very small levels ( $< 3\%$ ). This result is in very good agreement with optical studies of the small-scale structure of the diffuse Interstellar Medium (ISM) (Thoraval, Boissé, & Duvert 1999).

When convolved to the appropriate spatial resolution, our maps showed structure in the dust distribution which was strikingly well correlated with millimetre wave CO and CS emission maps of the cloud (see Fig. 3), although showing crucial differences at high optical depths where these other tracers of column density become unreliable (see Fig. 4). These comparisons enabled us, for the first time, to directly derive CO, CS, and  $N_2H^+$  abundances, and variations of, over an extinction range of 1–30 magnitudes, a range nearly an order of magnitude greater than achieved previously with optical star-counting techniques. In a recent experiment we were able to make a direct measurement of molecular depletion in a cold cloud core (Kramer et al. 1999). Finally, a comparison between our extinction data and millimetre continuum emission data allowed a most accurate measurement of the ratio of dust absorption coefficients at millimetre and near-infrared wavelengths (Kramer et al. 1998).

### 3. Barnard 68 as a Stellar Seed

Recently we have been concentrating efforts on mapping the densest regions of the ISM that are likely places of

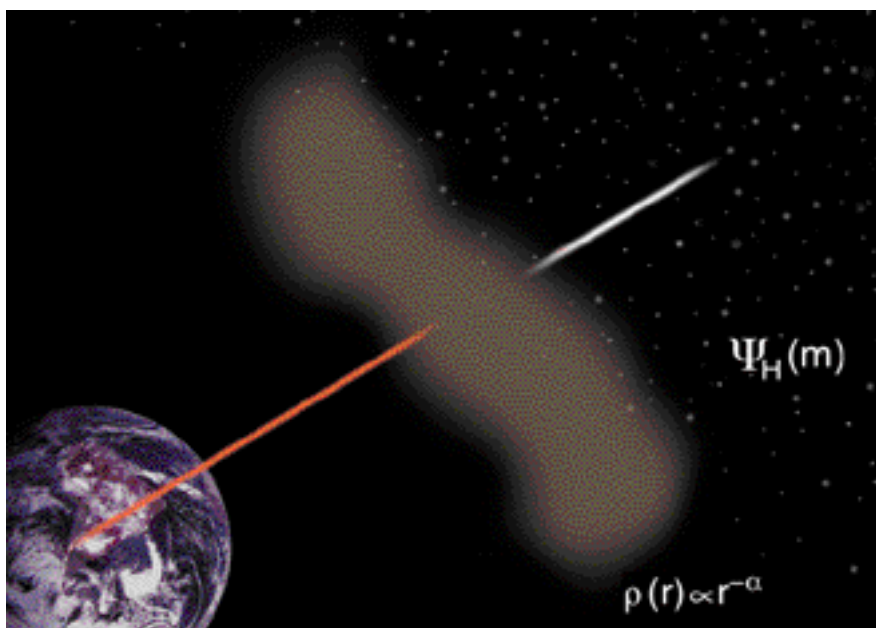


Figure 2: Illustration of the Near-Infrared Colour Excess (NICE) method used to derive and map dust column density in molecular clouds. Because the amount of reddening is directly proportional to the total extinction, we can determine the line-of-sight extinction to each star seen through a molecular cloud (at near-infrared wavelengths, NIR) using a reddening law for interstellar dust and knowledge of the star's intrinsic NIR colour.

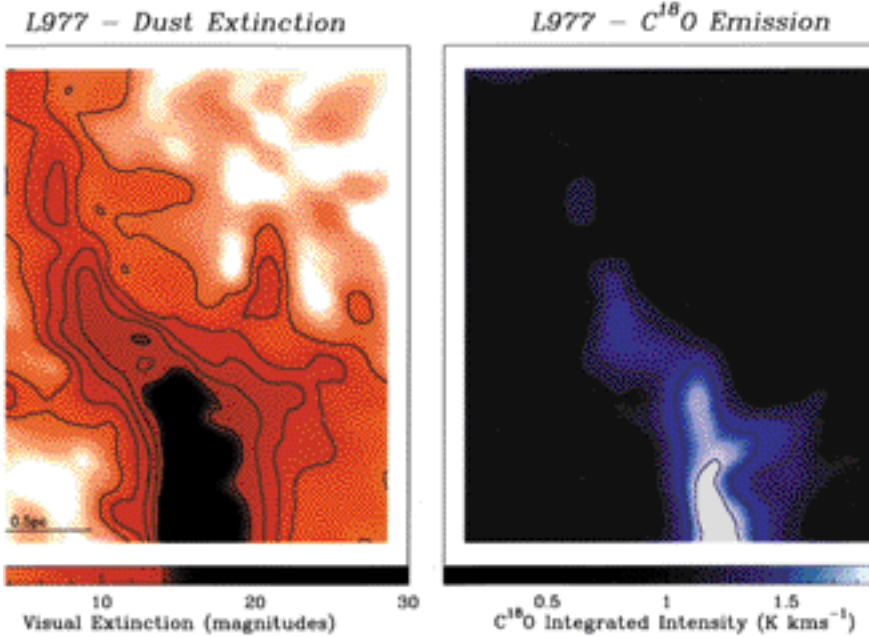


Figure 3: Dust extinction map and  $C^{18}O$  molecular line map of L977. The structure in the dust distribution correlates strikingly well with the millimetre-wave  $C^{18}O$  emission map of the cloud, although showing crucial differences at high optical depths (see next figure) where the CO tracer becomes unreliable (from Alves et al. 1999).

future star formation. We performed very sensitive near-infrared imaging observations to map the structure of a type of dark cloud known as a Bok globule (Bok & Reilly 1947), one of the least complicated configurations of molecular gas known to form stars (Fig. 5). The target cloud for our study, Barnard 68 (Figs. 1 and 5), is itself one of the finest examples of a Bok globule, and was selected because it is a nearby, relatively isolated and morphologically simple molecular cloud with distinct boundaries, a known distance (125 pc; Launhardt & Henning 1997), and temperature (16 K; Bourke et al. 1995). It was first discovered by E. E. Barnard (Barnard 1919) and was the target of several optical dust extinction studies by Bart Bok and co-workers (Bok & Reilly 1974; Bok 1977). Although a very dense cloud, Barnard 68 does not present any of the signatures of ongoing star formation, such as IRAS sources, outflows, or mm continuum sources (Avery et al. 1987; Reipurth, Nyman, Chini 1996).

Barnard 68 lies in the direction of the centre of the Galaxy but above the galactic plane where it is projected against the rich star field of the galactic bulge. This makes Barnard 68 a particularly ideal candidate for an infrared extinction study for the following reasons. First, the background bulge stars are primarily late-type (giant) stars whose intrinsic infrared colours span a narrow range and can be accurately determined from observations of nearby control fields. Second, the background star field is sufficiently rich to permit a detailed sampling of the extinction across the entire extent of the cloud.

Third, the cloud is sufficiently nearby that foreground star contamination is negligible.

We used the SOFI (Moorwood, Cuby, Lidman 1998) near-infrared camera on the European Southern Observatory's New Technology Telescope (NTT) to obtain deep infrared J band (1.25  $\mu\text{m}$ ), H band (1.65  $\mu\text{m}$ ) and Ks band (2.16  $\mu\text{m}$ ) images of the cloud over two nights in March 1999. Complementary optical data were obtained with ESO's Very

Large telescope (VLT) on Cerro Paranal, fitted with FORS1 CCD camera (Appenzeller et al. 1998), during one night of March 1999. The results of the optical and near-infrared imaging are displayed in Figure 1 (see page 1). At optical wavelengths obscuring dust within the cloud renders it opaque and completely void of stars (left). However, due to the wavelength dependence of dust extinction (i.e., opacity), the cloud is essentially transparent at infrared wavelengths enabling otherwise invisible stars behind the cloud to be imaged (right). We detected 3708 stars simultaneously in the deep H and K band images out of which  $\sim 1000$  stars, lying behind the cloud, are not visible at optical wavelengths. Because dust opacity decreases sharply with wavelength (Fig. 6), the colours of stars that are detected through a dust screen appear reddened compared to their intrinsic colours.

We have accurately sampled the dust extinction and column density distribution through the Barnard 68 cloud at more than a thousand positions with extraordinary (pencil beam) angular resolution. Although the individual measurements are characterised by high angular resolution, our mapping of the dust column density in the cloud is highly undersampled. Consequently, we smoothed these data to construct the first 10 arcsec resolution map of dust extinction of a cold dark cloud (Fig. 7) and an azimuthally averaged radial extinction (dust column density) profile of the cloud (Fig. 8). This is the most finely sampled and highest signal-to-noise radial column density profile ever obtained for a dense and cold molecular

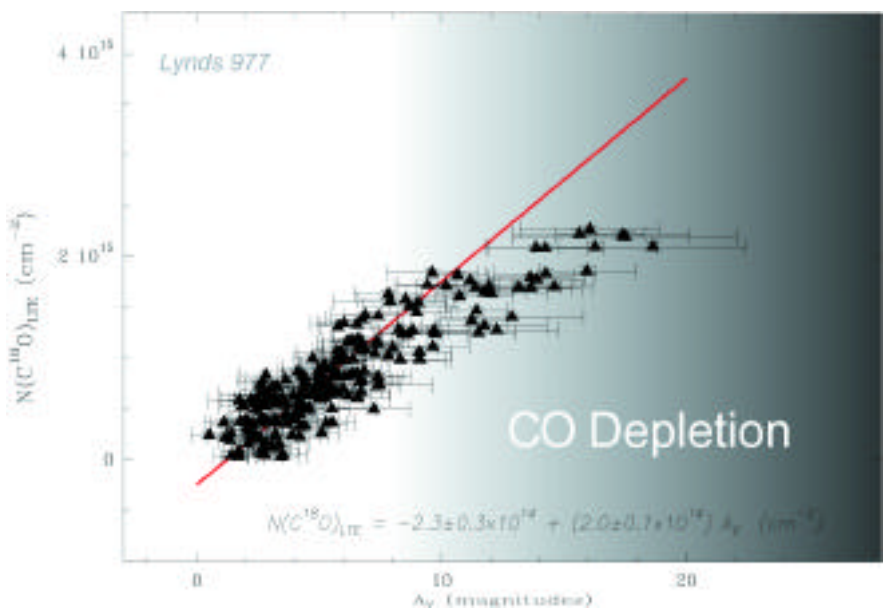


Figure 4: Relation between  $N(C^{18}O)_{LTE}$  and visual extinction  $A_V$  for molecular cloud L 977. The solid straight red line represents the result of a linear least-squares fit, with errors in both coordinates, over the entire data set. There is a clear deviation from the linear relation at extinctions  $\geq 10$  magnitudes above which  $C^{18}O$  becomes a very poor tracer of  $H_2$  (from Alves et al. 1999). Follow-up molecular line study of this cloud (Tafalla et al. 2001) suggests that, as in the IC 5146 cloud, depletion of CO might be occurring at high optical depths.

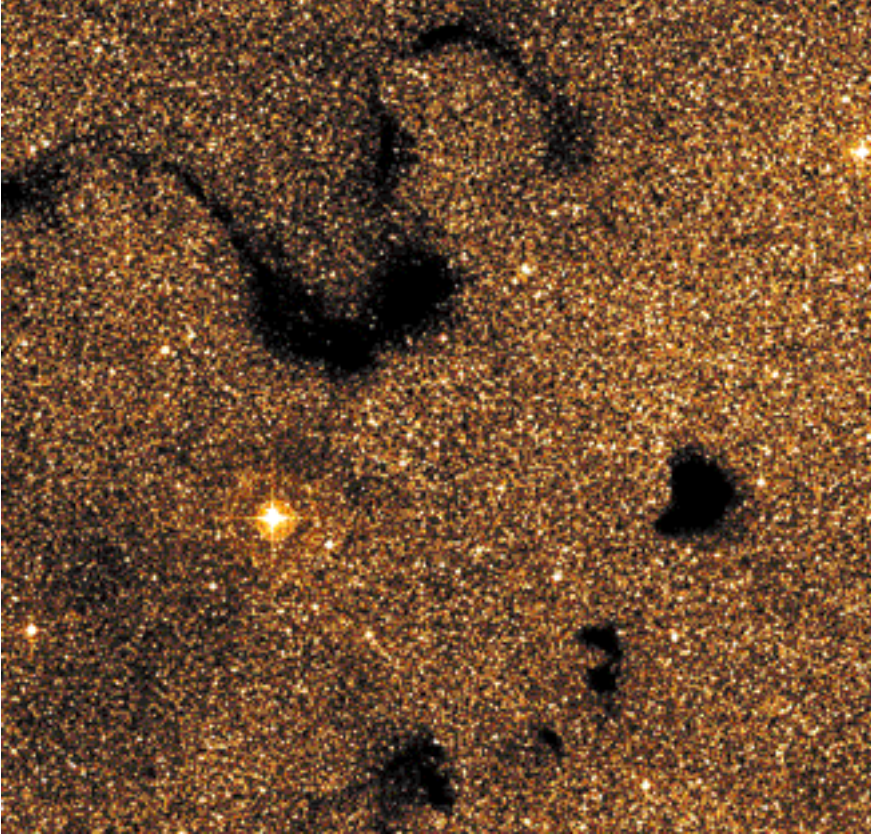


Figure 5: Palomar Digitized Sky Survey image of the neighbourhood of Barnard 68. Complexes of globules like the ones in this image (Barnard 68 to Barnard 72) may be the precursors of small young stellar groups, like the well-known TW Hya.

cloud. For the first time, the internal structure of a dark cloud has been specified with a detail only exceeded by that characterising a stellar interior.

### 3.1 Bonnor-Ebert Spheres

The extinction profile in Figure 8 is the projection of the cloud volume density profile function, and therefore provides an exquisite view of the internal structure of this dense dark cloud. As early as 1948 Bart Bok pointed out that roughly spherical homogenous looking clouds, such as Barnard 68, resemble single dynamical units much like the polytropic models of Lane and Emden used to describe stellar structure (Lane 1870; Emden 1907). Can Barnard 68 be described as a self-gravitating, polytropic sphere of molecular gas? To investigate the physical structure of the cloud, we begin with the assumptions of an isothermal equation of state and spherical symmetry.

The fluid equation that describes a self-gravitating, isothermal sphere in hydrostatic equilibrium is the following well-known variant of the Lane-Emden equation (Lane 1870, Emden 1907):

$$\frac{1}{\xi^2} \frac{d}{d\xi} \left( \xi^2 \frac{d\psi}{d\xi} \right) = e^{-\psi} \quad (1)$$

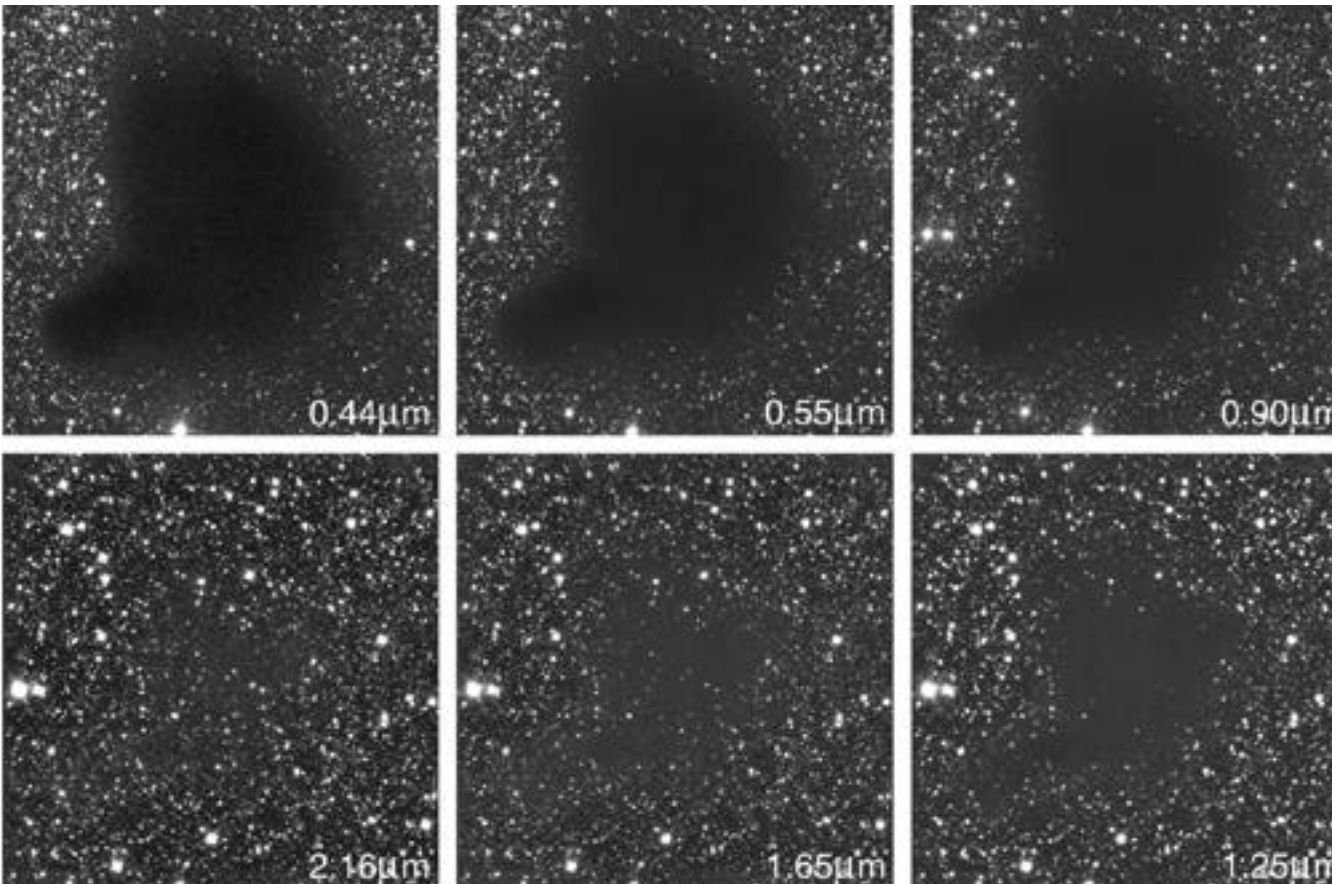


Figure 6: Deep BVJHK imaging of dark molecular cloud Barnard 68 done with FORS1 at the VLT and SOFI at the NTT. The wavelength dependence of interstellar dust extinction in Barnard 68 is clearly depicted in these images. The analysis of the near-infrared colours of the stars seen through the dark cloud allow the construction of the first 10' resolution map of mass as traced by dust extinction, and the most finely sampled and higher S/N density profile ever obtained for a cold dark cloud (from Alves et al. 2001b).

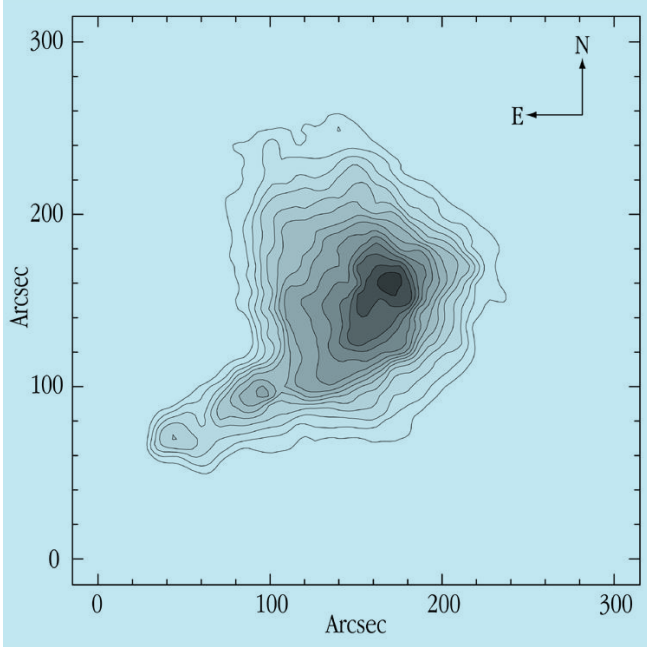


Figure 7: 10'' dust extinction map of Barnard 68. The contours start at  $A_V = 4$  mag and increase in steps of 2 mags. The peak extinction measured through the very centre of the cloud is 33 magnitudes of extinction (from Alves et al. 2001a).

deed an isothermal, pressure confined, and self-gravitating cloud. It is also likely to be in a state near hydrostatic equilibrium with thermal pressure primarily supporting the cloud against gravitational contraction. For Barnard 68,  $\xi_{max}$  is very near and slightly in excess of the critical radial parameter and the cloud may be only marginally stable and on the verge of collapse. If this is the case, we should expect molecular radio-spectroscopy of this cloud to reveal a quiet, non-turbulent cloud with narrow molecular emission lines. Indeed, preliminary results from our radio-spectroscopy observing campaign of Barnard 68 (with the IRAM 30-m Radio Telescope at Pico Veleta, Granada) reveal that the line width of the  $C^{18}O$  line in this cloud is  $\sim 0.18$  kms $^{-1}$ , one of the narrowest lines ever observed in molecular clouds, in perfect agreement with the Bonnor-Ebert sphere nature of Barnard 68.

where  $\xi$  is the non-dimensional radius,

$$\xi = \frac{r}{a} (4\pi G \rho_c)^{\frac{1}{2}} \quad (2)$$

while  $\psi(\xi)$  equals,

$$\psi(\xi) = -\ln(\rho/\rho_c) \quad (3)$$

for which  $r$  is the distance from the centre of the sphere,  $a$  is the isothermal sound speed inside the gas cloud ( $a = (KT/m)^{\frac{1}{2}}$ ),  $\rho$  is the density, and  $\rho_c$  is the central density. For an isothermal sphere bounded by a fixed external pressure there is a family of solutions characterised by a single parameter (Ebert 1955, Bonnor 1956):

$$\xi_{max} = \frac{R}{a} (4\pi G \rho_c)^{\frac{1}{2}} \quad (4)$$

Here  $\xi_{max}$  is the value of  $\xi$  at the outer boundary,  $R$ . Each of these solutions corresponds to a unique cloud mass density profile. Bonnor demonstrated that for  $\xi_{max} > 6.5$  such a gaseous configuration would be unstable to gravitational collapse (Bonnor 1956). The high quality of our extinction data permits a detailed comparison with the Bonnor-Ebert predictions and we find that there is a particular solution, ( $\xi_{max} = 6.9 \pm 0.2$ ), that fits the data extraordinarily well as seen in Figure 8. For the known distance (125 pc), and temperature (16 K), Barnard 68 has a physical radius of 12,500 AU, a mass of 2.1 solar masses, and a pressure at its boundary of  $P = 2.5 \times 10^{-12}$  Pa. This surface pressure is an order of magnitude higher than that of the general ISM (McKee 1999) but it is in rough agreement with the pressure inferred for the Loop I superbubble, where Barnard 68 is embedded, derived from X-ray observations with the

ROSAT satellite (Breitschwerdt et al. 2000).

The close correspondence of the observed extinction profile with that predicted for a Bonnor-Ebert sphere strongly suggests that Barnard 68 is in-

### 3.2 Reverse Engineering: Distance and Gas to Dust Ratio to Few Percent

The exact physical state of the Barnard 68 cloud is further constrained by the fact that  $\xi_{max}$ , which is solely de-

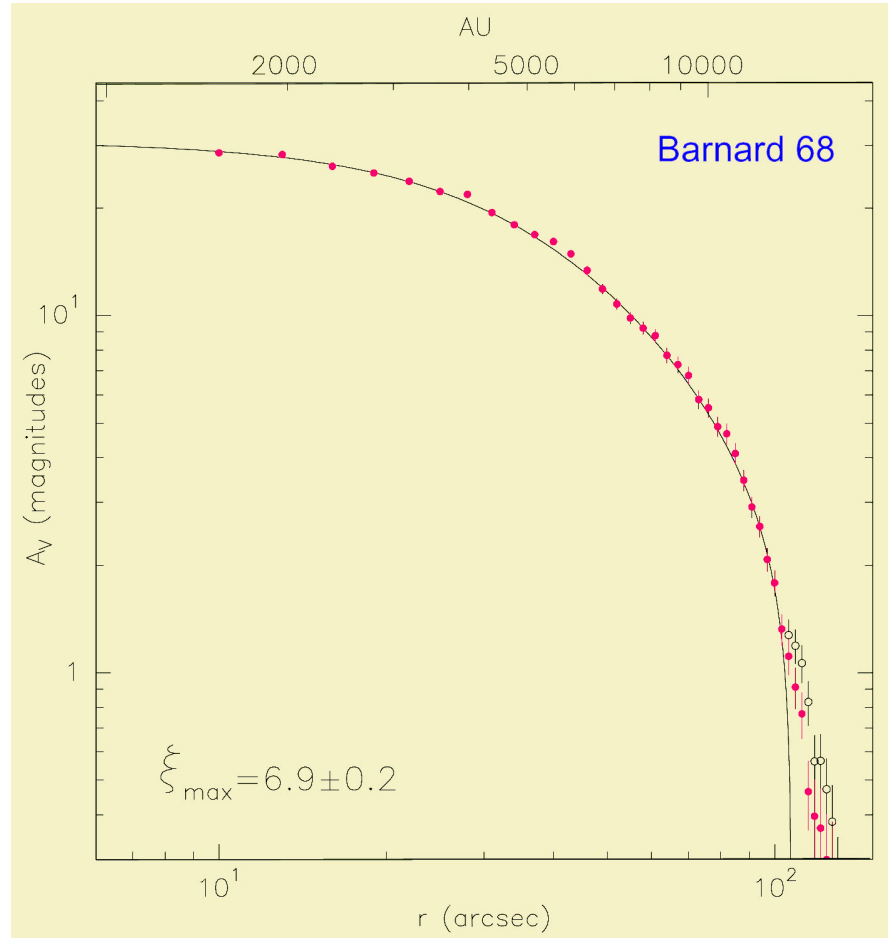


Figure 8: Azimuthally averaged radial dust column density profile of Barnard 68. The red circles show the data points for the averaged profile of a subsample of the data that do not include the cloud's south-east prominence, seen in Figure 6. The solid black line represents the best fit of a theoretical Bonnor-Ebert sphere to the data.



Figure 9: Dark cloud BHR 71 caught in the act of forming a stellar binary. This cloud will be a primary target for deep extinction mapping with the VLTI. The nebula seen against the dark cloud is a cavity carved out by a spectacular molecular outflow (Bourke et al. 1997; Garay et al. 1998 – see also Garay et al. in *The Messenger* No. 83). Combining data from ISO and SEST, Bourke (2001) has shown that BHR71 probably contains a binary system in the making, with each protostar driving its own outflow. This colour composite was constructed by R. Fosbury and R. Hook with data taken during Science Verification of FORS2.

rived from the shape of the observed column density distribution, uniquely specifies the combination of central density, sound speed and physical size that characterises the cloud (i.e., Equation 4). Independent knowledge of any two of these parameters directly determines the value of the third. For example, in Barnard 68 we independently measure the dust extinction (which is directly related to the mass column density, via the gas-to-dust ratio in the cloud) and the angular size of the cloud (which is directly related to its physical size via the cloud's distance). Thus, if we know the temperature of the

cloud, our measurement of its extinction and angular size (combined with the constraint that  $\tau_{max} = 6.9 \pm 0.2$ ) independently gives the distance to the cloud, provided the gas-to-dust ratio is assumed. The temperature of the molecular gas in Barnard 68 has been previously measured using observations of emission from the (1,1) and (2,2) metastable transitions of the ammonia molecule and found to be  $16 \pm 1.5$  K (Bourke et al. 1995). For a canonical gas-to-dust ratio ( $1.9 \times 10^{21}$  protons/magnitude; Bohlin, Savage, & Drake 1978), we derive a distance to Barnard 68 of  $112 \pm 3$  pc. Here the quoted un-

certainty (3%) arises solely from the uncertainty in  $\tau_{max}$ . Accounting for the uncertainty in the temperature measurement, the overall uncertainty increases only to 8%, or  $\pm 9$  pc. From its association with the Ophiuchus complex, the distance to the cloud has been estimated to be  $125 \pm 25$  pc (de Geus et al. 1989), which within the uncertainties agrees with our derivation. This, in turn, implies that the gas-to-dust ratio in this dense cloud must be close to the canonical interstellar value. Indeed, if we independently know the distance to the cloud, our modelling directly yields the gas-to-dust ratio in the cloud.

Assuming a distance of 125 pc, our measurements allow a high-precision determination (2%) for the gas-to-dust ratio in this cloud of  $1.73 \pm 0.04 \times 10^{21}$  protons/magnitude. If we also account for the uncertainties in distance and temperature, the overall uncertainty (accuracy) of our determination increases to  $\pm 0.4 \times 10^{21}$  protons/magnitude, or 23%. Within the overall error, this ratio is the same as the long accepted value characterising low-density interstellar gas and is the first independent and relatively accurate determination of this important astrophysical parameter in a dense molecular cloud core.

### 3.3 On the Origin of Small Stellar Groups

Recently, there has been special attention for isolated and sparsely populated associations of young low-mass stars similar to the recently identified TW Hydra association (Rucinsky & Krautter 1983). The TW Hydra association is a stellar group near the solar system consisting of a handful of young low-mass, sunlike stars, which has been a primary target of recent substellar objects search (e.g. Neuhäuser et al. 2000a, Neuhäuser et al. 2000b). The existence of such a young stellar group presents an interesting problem to astronomers because its origin is difficult to explain given its youth and relatively large distance from known sites of star formation. Bok globules such as those in the Barnard 68 group are thought to be remnant dense cores produced as a result of the interaction of massive O stars and molecular clouds (Reipurth 1983). Over their short lifetimes, such massive stars, through ionisation, stellar winds and ultimately supernova explosions, very effectively disrupt the molecular clouds from which they formed. In the process, large shells of expanding gas are created. When surrounding clouds are disrupted by the passage of these shells, a few of their most resilient dense cores will be left behind, embedded within the shell's hot interior. Remnant cores with just the right mass can establish pressure equilibrium with the hot gas within the shell and survive to become Bok globules. Eventually, as a result of processes described above, these clouds will evolve to form low mass, sun-like stars which are relatively isolated and far from the original birthplace of the O stars. We suggest that Barnard 68, and its neighboring globules B69, B70 and B72 (Figure 5) may be the precursors of a small stellar group, like TW Hya. Up to 35% of all Bok globules con-

tain newly-formed stars (Launhardt & Henning 1997) and thus it is likely that our observations of the starless Barnard 68 cloud provide the first detailed description of the initial conditions prior to the collapse of dark globules and the formation of isolated, low-mass stars.

### 4. The Future

Significant progress in extinction mapping studies will result when the DENIS and 2MASS all-sky near-infrared imaging surveys are completed and released. These surveys will be sufficiently sensitive to produce moderate-depth extinction maps (i.e.,  $A_V \leq 25$  mags) of many nearby dark clouds in those directions of the Galaxy where field stars suffer little extraneous extinction. In the immediate future, large-aperture telescopes, such as the VLT outfitted with ISAAC and NAOS/CONICA, will provide the additional capability to perform deeper surveys of the higher extinction regions ( $25 \leq A_V \leq 60$  mags) in these clouds (as the star forming globule BHR 71 in Figure 9). Finally, space-based infrared telescopes, such as the NGST, should enable the regions of deepest extinction ( $A_V > 60$  mags) to be probed. Together, such observations promise to render a very complete understanding of the physical and chemical structure of molecular clouds and of the general initial conditions to the star-formation process.

### 5. Acknowledgements

The authors acknowledge Marco Lombardi for fruitful discussions and assistance, the Paranal Science Operations team for observing Barnard 68 with FORS1 on VLT Antu, Richard West and Edmund Janssen, Richard Hook and Robert Fosbury for composing Figure 1. The authors are thankful to Monika Petr for helpful discussions during the preparation of the VLT observations.

### References

Alves, J., Lada, C.J., Lada, E.A., Kenyon, S., & Phelps, R. 1998, *ApJ*, **506**, 292.  
 Alves, J., Lada, C.J., & Lada, E.A. 1999, *ApJ*, **515**, 265.  
 Alves, J., Lada, C.J., & Lada, E.A. 2001a, *Nature*, **409**, 159.  
 Alves, J., Lada, C.J., & Lada, E.A. 2001b, *ApJ*, submitted.  
 André, P., Ward-Thompson, D., & Barsony, M. 2000, *Protostars and Planets IV*,

(Tucson: University of Arizona Press), eds. Mannings, V., Boss, A.P., Russell, S. S.  
 Appenzeller, I., Fricke, K., Fürtig, W., Gässler, W., Häfner, R., Harke, R., Hess, H., Hummel, W., Jürgens, P., Kudritzki, R., Mantel, K., Meisl, W., Szeifert, T., & Tarantik, K. *Successful Commissioning of FORS1 – the First Optical Instrument on the VLT*, *The Messenger* **94**, 1–6 (1998).  
 Bok, B. & Reilly, E. 1947, *ApJ*, **105**, 255.  
 Bok, B. 1948, Centennial Symposia (Harvard-Observatory Monographs No. 7); Harvard-College Observatory, Cambridge.  
 Bourke, T., Hyland, A., Robinson, G., James, S. & Wright, C. 1995, *MNRAS*, **276**, 1067.  
 Bourke, T., Garay, G., Lehtinen, K., Köhnenkamp, I., Launhardt, R., Nymann, L., May, J., Robinson, G., Hyland, A. 1997, *ApJ*, **476**, 781.  
 Bourke, T. 2001, *ApJ*, submitted.  
 Breitschwerdt, D., Freyberg, M. & Egger, R. 2000, *A&A*, **361**, 303.  
 Chandler, C. & Richer, J. 2000, *ApJ*, **530**, 851.  
 de Geus, E., de Zeenw, P. & Lub, J. 1989, *A&A*, **216**, 44.  
 Emden, R. 1907, *Gaskugeln*, (Leipzig: Teubner).  
 Garay, G., Köhnenkamp, I., Bourke, T., Rodriguez, L., Lehtinen, K. 1998, *ApJ*, **509**, 768.  
 Garay, G., Köhnenkamp, I., Rodriguez, L., 1966, *The Messenger* **83**, 31.  
 Kramer, C., Alves, J., Lada, C., Lada, E., Sievers, A., Ungerechts, H., Walmsley, M. 1997, *A&A*, **329**, 33.  
 Kramer, C., Alves, J., Lada, C.J., Lada, E.A., Sievers, A., Ungerechts, H., Walmsley, C.M. 1999, *A&A*, **342**, 257.  
 Lada, C.J., Lada, E.A., Clemens, D.P., & Bally, J. 1994, *ApJ*, **429**, 694.  
 Lada, C.J. 1996, Proceedings of IAU Symposium CO: *Twenty-Five Years of Millimeter-Wave Spectroscopy*, eds. W.B. Latter et al. (Kluwer-Dordrecht), p. 387.  
 Lada, C.J., Alves, J., Lada, E.A. 1999, *ApJ*, **512**, 250.  
 Lane, J. 1870, *American Journal of Science and Arts*, Series 2, 4, 57.  
 Launhardt, R. & Henning, T. 1997, *A&A* **326**, 329.  
 Mckee, C. 1999, in *The Origin of Stars and Planetary Systems*, eds. C. Lada & N. Kylafis (Dordrecht: Kluwer).  
 Moorwood, A., Cuby, J. & Lidman, C. SOFI Sees First Light at the NTT, *The Messenger* **91**, 9–13 (1998).  
 Neuhäuser, R., Brandner, W., Eckart, A., Guenther, E., Alves, J., Ott, T., Huélamo, N., Fernandez, M. 2000a, *A&A*, **354**, 9.  
 Neuhäuser, R., Guenther, E., Petr, M., Brandner, W., Huélamo, N., Alves, J. 2000b, *A&A*, **360**, 39.  
 Ostriker, J. 1964, *ApJ*, **140**, 1056.  
 Reipurth, B. 1983, *A&A*, **117**, 183.  
 Reipurth, B., Nymann, L. & Chini, R. 1996, *A&A*, **314**, 258.  
 Rucinski, S. & Krautter, J. 1983, *A&A*, **121**, 217.  
 Tafalla, M., Alves, J., & Lada, C. 2001, in prep.  
 Thoraval, S., Boissé, P., Duvert, G. 1999, *A&A*, **351**, 1051.

# Strong Accretion and Mass Loss Near the Substellar Limit

*F. COMERÓN, ESO, Garching, Germany*

*M. FERNÁNDEZ, Instituto de Astrofísica de Andalucía, Granada, Spain*

Accretion and outflows of mass are among the most distinctive phenomena associated to star formation. Their observational manifestations cover a broad range of appearances and wavelengths, from the large X-ray emitting bubbles caused by stellar winds moving at several thousands of kilometres per second, to the cold dust shells around low-mass stars detected by

their millimetre-wave emission. Even stars with only a few tenths of the mass of the Sun display in their earliest stages spectacular signatures of interaction with the circumstellar environment, such as the strong emission lines seen in T Tauri stars or the fast-moving jets that produce Herbig-Haro objects.

Can strong accretion and mass loss take place even at substellar masses?

Young brown dwarfs are currently known to share many characteristics with the more massive T Tauri stars. The similarities include mid-infrared emission, revealed by ISOCAM (e.g. Comerón et al. 1998, Persi et al. 2000) from warm dust in circumstellar disks or envelopes that provide large reservoirs of mass for accretion. The spectra of very young brown dwarfs often display



Figure 1: A  $B, V, R_C$  image of the field around LS-RCrA1 obtained with the Wide Field Imager at the ESO-MPG 2.2-m telescope. LS-RCrA 1 is the faint object at the centre and marked with an arrow. The bright nebulosity at the upper left corner contains the T Tauri stars R and T CrA. The comma-shaped nebula to the bottom right of that nebula is the Herbig-Haro object HH 100, and the red compact nebula at the bottom centre of the image is HH 101. The bright star near the centre of the image, to the left and below LS-RCrA1, is V709 CrA. The field is approximately  $10' \times 10'$  in size.

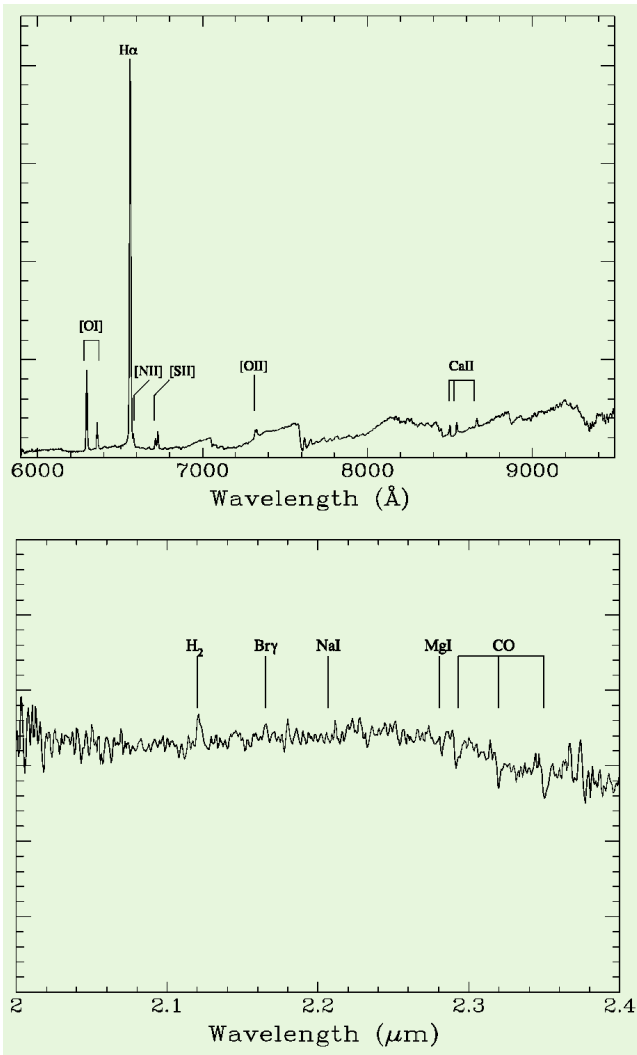


Figure 2: Visible (top) and near-infrared (bottom) spectra of LS-RCrA 1, obtained respectively with FORS2 and ISAAC in March 2000. The most prominent emission lines are marked in the visible spectrum. In the infrared spectrum we mark the position of the detected lines due to  $H_2$  and CO, as well as the expected positions of some atomic features that should be detectable in this region for a normal M6 star.

H emission that is commonly associated to accretion, as confirmed from high-resolution spectroscopy (Muzerolle et al. 2000). Like T Tauri stars, young brown dwarfs also have been found to possess X-ray emission (Neuhäuser & Comerón 1998; Comerón, Neuhäuser, and Kaas 1998) caused by the magnetic fields that play a fundamental role in regulating the flow of mass from the accretion disk onto the surface (Hartmann 1998). In view of these similarities, one may wonder if the spectral signposts of intense accretion sometimes displayed by classical T Tauri stars, and very often found to be correlated with strong mass loss, may also be found near the substellar limit or even below.

Here we present our observations of a very late-type faint member of the R Coronae Australis star-forming cloud that displays an unusually rich emission-line spectrum, similar to that of more massive counterparts, in which both accretion and outflow signatures

coexist. This is the latest-type object for which such an intense emission-line spectrum has been observed so far. The late-type spectrum and the faintness of the underlying object suggest that it is near or below the borderline separating stars from brown dwarfs, showing that such spectacular spectral signatures can be present even at masses of a few per cent of a solar mass. The details of this work are described in extent in a separate paper (Fernández & Comerón 2001).

The special characteristics of the object that we present here, hereafter referred to as LS-RCrA 1 (where LS stands for La Silla) were first revealed in a slitless spectroscopy survey of the core of the R Coronae Australis star-forming region, carried out with DFOSC at the 1.5-m Danish telescope at La Silla in April 1999. The slitless spectroscopy frames showed only a dot at the expected position of H for an otherwise inconspicuous object of  $R_C \approx 19.5$ , with a continuum too faint to be seen in those observations. Near-infrared *JHK* photometry was obtained with SOFI at the NTT in February 2000. Further spectroscopic observations were carried out at the VLT, both with FORS2 in the visible and ISAAC in the K band, in March 2000. Finally, short exposures in *BVR\_C I\_C* were obtained with the WFI at the 2.2-m telescope in August, to check for possible photometric variability. A colour composite of a part of the WFI image is shown in Figure 1, centred on LS-RCrA 1 (see also <http://www.eso.org/outreach/press-rel/pr-2000/phot-25-00.html>).

Figure 2 shows both the FORS2 and ISAAC spectra of LS-RCrA1. The most outstanding feature in the visible is the abundance of strong emission lines, dominated by H with an equivalent width of approximately 330 Å. For-

bidden lines due to [OI], [OII], [NII], and [SII] are also clearly identified, as well as the Ca II triplet near 8550 Å. The appearance and intensity of these emission lines is not unprecedented, and the line ratios are similar to those of Krautter's star (Th 28; Graham and Heyer 1988), a G8-K2 star that powers a string of Herbig-Haro objects. However, the underlying spectrum of LS-RCrA1 is much later than that of Th 28 and other T Tauri stars with strong emission, and can be reliably classified as M6-M7. At the age of the R Coronae Australis, such a late spectral type implies a mass below 0.1 solar masses, and probably substellar.

The ISAAC *K*-band spectrum also presented in Figure 2 is remarkably featureless. At the resolution and signal-to-noise of these observations, a late M-type spectrum should display atomic features in that region due to Na I, Ca I, Mg I, as well as prominent CO bandheads starting at 2.29 μm. Only the latter are clearly identified in the spectrum on LS-RCrA 1, but with equivalent widths of less than half the typical value for its spectral type. Finally, the  $H_2$  line at 2.12 μm is clearly seen in emission.

A final surprise from our observations of LS-RCrA1 comes from its faintness. The measured brightness from our WFI images is  $B = 23.1$ ,  $V = 21.3$ ,  $R_C = 19.8$ ,  $I_C = 18.0$ , and from our SOFI images  $J = 15.3$ ,  $H = 14.5$ ,  $K = 13.9$ . Since its moderately blue colours imply a slight extinction at most and the R Coronae Australis clouds are only  $150 \pm 20$  pc away, this places LS-RCrA1 among the intrinsically faintest members known of a star-forming region.

## Interpretation

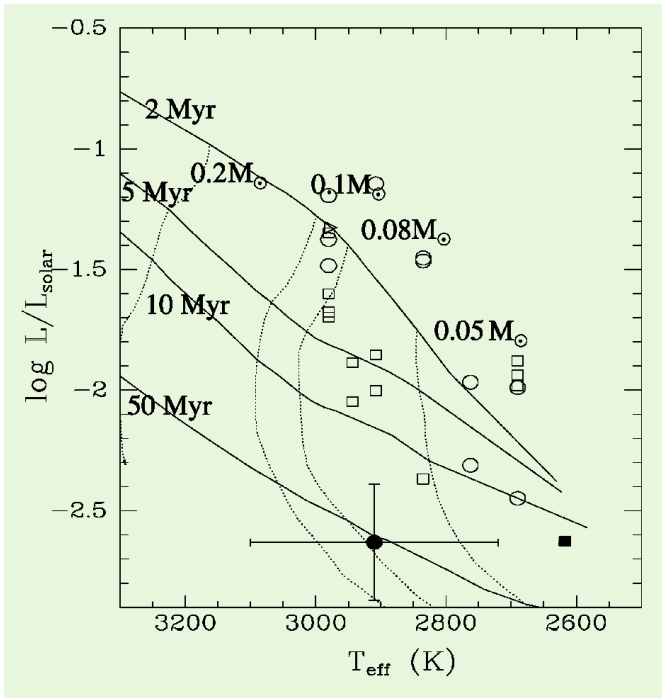
The numerous forbidden emission lines in the spectrum of LS-RCrA 1 strongly resemble those seen in low-mass stars undergoing strong mass loss, such as those powering Herbig-Haro objects (e.g. Reipurth et al. 1986). On the other hand, the large strength of the H line as compared to [SII] suggests that most of the H emission is actually due to accretion, rather than to mass loss. The similar equivalent widths of the Ca II lines near 8500 Å, together with the absence of forbidden-line emission of [CaII], also hint that CaII emission arises from a dense, optically thick region. It seems therefore that LS-RCrA 1 is simultaneously undergoing strong accretion and mass loss, just like its higher-mass T Tauri counterparts that lie at the origin of Herbig-Haro flows.

The *K*-band spectrum presented also shows some characteristics commonly found among very young objects enshrouded by circumstellar material, such as  $H_2$  emission and the absence of any detectable absorption features apart from much weakened CO band-

heads. The lack of absorption lines is commonly interpreted as due to strong veiling of the photospheric spectrum by emission from warm circumstellar dust, that contributes most of the flux at 2  $\mu\text{m}$  and beyond, and is usually correlated with the appearance of H<sub>2</sub> emission (Greene & Lada 1996). In that respect, the K-band spectrum of LSRCrA 1 is "Class I-like", following the widely-used classification of young stellar objects (e.g. Shu, Adams, and Lizano 1987). However, the shape of the continuum at 2  $\mu\text{m}$  is remarkably flat in that region, while the infrared *JHK* colours show no appreciable sign of the circumstellar excess emission that would be needed to dilute the photospheric features beyond detectability in our spectra. In other words, dust does not seem to significantly contribute to the flux of LSRCrA 1 in the 2 micron region, which in that respect is "Class III-like". Such a co-existence of Class I-like and Class III-like features in the K-band spectrum of LSRCrA 1 is not found among the higher-mass objects that have been studied so far, and leads us to consider other possible explanations to the lack of atomic features and the weakness of the CO bands. An interesting possibility in this respect is that the photospheric spectral features in the 2  $\mu\text{m}$  region may be largely filled by emission produced in the heated infalling material near the surface of the star, without being accompanied by continuum emission (Martin 1996).

What is the mass and age of LSRCrA 1? Its membership in the R Coronae Australis star-forming region and the vigorous accretion and mass-loss activity, found only at the earliest stages of stellar evolution, both suggest an age of only a few million years. At this age, LSRCrA 1 should be early in its contraction track and have a relatively large radius, and therefore brightness. However, as mentioned earlier, LSRCrA 1 is surprisingly faint as compared to objects of similar spectral type in star-forming regions. Figure 3 illustrates this: we have plotted in it the position of LSRCrA1 in a temperature-luminosity diagram, where these quantities are inferred from its spectral type and available photometry. Also shown for comparison are pre-main sequence evolutionary tracks and isochrones from Baraffe et al. (1998), and the positions of other very low mass stars and brown dwarfs identified in other star-forming regions. The main contribution to the error bars is due to uncertainties in translating spectral types and magnitudes into temperatures and luminosities. Since the position of the other objects plotted in Figure 3 was computed in the same way as that of LSRCrA1, any systematic errors in the estimate of temperature and luminosity of the latter should move both LSRCrA 1 and the other sources in the same direction and by a similar

Figure 3: Position of LSRCrA 1 (filled circle with error bars) in a temperature-luminosity diagram, with theoretical isochrones and evolutionary tracks from Baraffe et al. (1998) plotted for comparison. Also shown are the positions of other late-type objects in star-forming regions, whose spectral types and infrared photometry are taken from the literature and transformed into temperature and luminosity using the same method as for LSRCrA 1 (see Fernández and Comerón 2001 for details on the transformation). The other sources are from Chamaeleon I (open circles; Comerón, Neuhäuser, and Kaas 2000) and IC 348 (open squares; Luhman 1999). Also plotted are V410 X-ray 3 (open triangle; Luhman 2000) and Oph 162349.8-242601 (filled square; Luhman, Liebert, and Rieke 1997). As explained in the text, the error bars come primarily from the uncertainty in the transformation from spectral type and photometry to temperature and luminosity, and affect in a similar way the positions of all the sources. Therefore, although the precise luminosity and temperature of LSRCrA1 are uncertain by the amount given by the error bars, the offset relative to the other sources plotted is a well established feature.



amount. Therefore, although the temperature and luminosity of LSRCrA 1 are determined with only a rather limited accuracy, its large offset with respect to other known late-type young objects is well established.

If taken at face value, the position of LSRCrA 1 seems to imply that its age is of the order of several times 10<sup>7</sup> years, about one order of magnitude older than the age inferred from the rest of the members of the R Coronae Australis region (Wilking et al. 1997), and also much older than other stars displaying such strong signs of accretion. The rather implausible age and the offset with respect to other young objects of similar underlying spectral characteristics leads us to look for alternative interpretations to the unexpected position of LSRCrA 1 in the temperature-luminosity diagram.

The most obvious peculiarity that separates LSRCrA 1 from the other very low mass objects plotted in Figure 3 is the signs of strong accretion and mass loss on an object of such a low temperature and luminosity, and this may be the reason why LSRCrA 1 looks so old and so different from those other objects. Modellers of low-mass pre-main sequence evolution in the last decade have stressed the great importance of an appropriate, realistic treatment of the boundary condition represented by the atmosphere for correctly reproducing the evolution of temperature and luminosity as a function of

time. The impact of both strong accretion and mass loss on the structure of the atmosphere of LSRCrA1 may thus be sufficient to invalidate a direct comparison between its observational characteristics and the predictions of theoretical models that do not take those factors into account. Indeed, calculations performed by Hartmann, Cassen, and Kenyon (1997) have found that accretion increases both temperature and luminosity with respect to the predictions of accretionless models that assume the same mass and age of the central object. The net result is to make the object appear hotter, and somewhat older, than an object of equal mass and age but without accretion. The calculations of those authors use only moderate accretion rates on central objects of larger mass than the one presented here, and can therefore not be directly extrapolated to LSRCrA 1. However, they do suggest that LSRCrA1 may be actually younger than the  $5 \times 10^7$  years, and less massive than the  $\sim 0.08$  solar masses, implied by the direct comparison to pre-main-sequence tracks. Since 0.08 solar masses is very close to the borderline separating low-mass stars from brown dwarfs, the possibility that accretion is actually making the spectral type appear *earlier* than it would be without accretion suggests that LSRCrA 1 may have a mass well below the brown dwarf limit.

In any case, regardless of whether LSRCrA 1 is stellar or substellar, it is

clearly a so far unique object that poses an interesting case study in several respects. It demonstrates that the spectacular emission-line systems found in classical T Tauri stars can be present also at much lower masses, and suggests that intense accretion and mass loss can dramatically alter the spectroscopic and photometric properties of the underlying object. It stresses the need to complement existing models for the early evolution of low-mass objects with significant accretion and mass loss rates. A consequence of this is the intriguing possibility of biases in current studies of the mass and age distributions of young stellar aggregates if a significant fraction of their members undergo accretion and mass loss phases like LSRCrA 1, due to the reliance of such studies on pre-main sequence evolutionary tracks.

Of course, LS-RCrA 1 also suggests a variety of follow-up of observational studies: what information can we obtain from high-resolution spectra of the emission lines? Does the mass loss of LS-RCrA1 cause any visible impact (as yet undetected in our images) in the surrounding interstellar medium, like the Herbig-Haro objects generated by more massive stars? How do the signatures of accretion and mass loss vary with time? What do possible photometric variations tell us about the existence

and distribution of dark and hot spots on its surface? Can we trace the reservoir of cold circumstellar gas around LS-RCrA 1 through its mid-, far-infrared, and radio emission? How common are objects like LS-RCrA 1 in star-forming regions? Is the rich emission-line spectrum of LS-RCrA1 a rarity among very low mass objects, or does it rather represent a short-lived evolutionary phase? Is the simultaneous appearance of Class I and Class III characteristics a part of the peculiarities of LS-RCrA 1, or is it common among young very low mass stars and brown dwarfs? Are there other signs of activity, such as X-ray emission, associated to LSRCrA 1? Answering these questions and understanding objects like LS-RCrA 1 from a theoretical, quantitative point of view, is essential for placing LS-RCrA 1 in the context of what is already known about the early stages of the lives of stars at different masses, extending such knowledge beyond the substellar edge.

### Acknowledgements

We are pleased to thank the staffs of both La Silla and Paranal Observatories for excellent support during our observations, as well as to Paranal Science Operations and the User Support Group for the successful exe-

cution of our service mode observations with FORS2 at Kueyen.

### References

- Baraffe, I., Chabrier, G., Allard, F., Hauschildt, P. H., 1998, *A&A*, **337**, 403.  
 Comerón, F., Neuhäuser, R., Kaas, A. A., 1998, *The Messenger*, **94**, 38.  
 Comerón, F., Neuhäuser, R., Kaas, A. A., 2000, *A&A*, **359**, 269.  
 Comerón, F., Rieke, G. H., Claes, P., Torra, J., Laureijs, R. J., 1998, *A&A*, **335**, 522.  
 Fernández, M., Comerón, F., 2001, submitted to *A&A*.  
 Graham, J. A., Heyer, M. H., 1988, *PASP*, **100**, 1529.  
 Greene, T. P., Lada, C. J., 1996, *AJ*, **112**, 2184.  
 Hartmann, L., 1998, "Accretion processes in star formation", Cambridge Univ. Press.  
 Hartmann, L., Cassen, P., Kenyon, S. J., 1997, *ApJ*, **475**, 770.  
 Luhman, K. L., 1999, *ApJ*, **525**, 466.  
 Luhman, K. L., 2000, *ApJ*, **544**, 1044.  
 Luhman, K.L., Liebert, J., Rieke, G. H., 1997, *ApJ*, **489**, L165.  
 Martin, S. C., 1996, *ApJ*, **470**, 537.  
 Muzerolle, J., Briceno, C., Calvet, N., Hartmann, L., Hillenbrand, L., Gullbring, E., 2000, *ApJ*, **545**, L141.  
 Neuhäuser R., Comerón F., 1998, *Science*, **282**, 83.  
 Persi, P., et al., 2000, *A&A*, **357**, 219.  
 Reipurth, B., Bally, J., Graham, J. A., Lane, A. P., Zealey, W. J., 1986, *A&A*, **164**, 51.  
 Shu, F. H., Adams, F. C., Lizano, S., 1987, *ARA&A*, **25**, 23.  
 Wilking, B. A., McCaughrean, M. J., Burton, M. G., Giblin, T., Rayner, J. T., Zinnecker, H., 1997, *AJ*, **114**, 2029.

# Star Formation at $z = 2-4$ : Going Below the Spectroscopic Limit with FORS1

J. U. FYNBO<sup>1</sup>, P. MØLLER<sup>1</sup>, B. THOMSEN<sup>2</sup>

<sup>1</sup>European Southern Observatory, Garching, Germany

<sup>2</sup>Institute of Physics and Astronomy, University of Århus, Århus, Denmark

## Introduction

The population of bright galaxies at  $z = 2-4$  has been studied intensively using the Lyman-Break technique (Steidel et al. 1996; Cristiani et al. 2000). Currently, redshifts can be determined from absorption features of galaxies selected in this way down to  $R \approx 25.5$  (e.g. Steidel et al. 2000), which is commonly referred to as the spectroscopic limit. Currently, very little is known about the galaxy population below the spectroscopic limit. This is an unfortunate situation since all the information on the chemical enrichment of young galaxies (Damped Ly- Absorbers) accessible through QSO absorption lines seems to be valid mainly for galaxies significantly fainter than  $R = 25.5$  (Fynbo et al. 1999; Haehnelt et al. 2000). In order to select and study

galaxies fainter than the current spectroscopic limit, one has to rely on other selection criteria than the Lyman-Break. Two promising possibilities are (i) to select galaxies with Ly- emission lines, and (ii) to study the host galaxies of Gamma-Ray Bursts (GRBs).

## Ly- $\alpha$ Selected Galaxies

Ly- selection of high-redshift galaxies has been attempted for many years, but only recently with significant success (Møller and Warren 1993; Francis et al. 1995; Cowie and Hu 1998; Pascarella et al. 1998; Kudritzki et al. 2000; Fynbo et al. 2000a; Steidel et al. 2000; Kurk et al. 2000). In 1998 we detected 6 candidate Ly- emitting galaxies (called S7-S12) in the field of the QSO Q1205-30 at  $z = 3.036$  with deep NTT narrow-band imaging (Fynbo et al.

2000b). In March 2000 we carried out follow-up Multi-Object Spectroscopy with FORS1 on the 8.2-m Antu telescope (UT1). We also obtained deeper broad-band B and I imaging reaching 5 (2) detection limits in 1 arcsec<sup>2</sup> circular apertures of 25.9 (26.9) in the I-band and 26.7 (27.7) in the B-band (both on the AB system). The results of these observations are presented in Fynbo et al. (2001a), and summarised here.

## Imaging

In Figure 1 we show image sections with Ly- (top), VLT B-band (middle) and VLT I-band (bottom) for S7-S12. As seen, despite the faint detection limits, only for S7 and S9 is there a corresponding source detected in the broad bands ( $B(AB) = 25.6$  and 25.4 respectively). For the sources S8 and

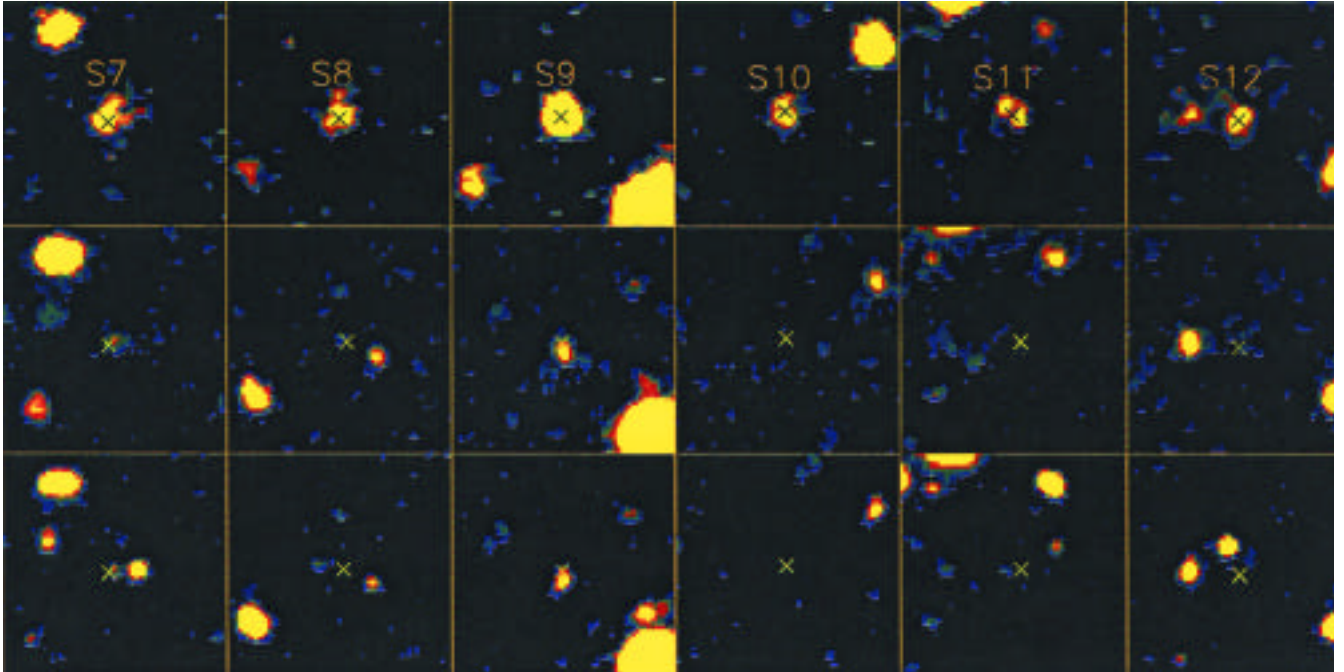


Figure 1: Image sections ( $12 \times 12$  arcsec $^2$ ) from the NTT narrow-band (top), VLT B-band (middle) and VLT I-band (bottom) for each of the six candidate emission-line galaxies S7–S12 (Fynbo et al. 2000a). East is to the left and north up.

S10–S12 no convincing broad-band counterpart is detected.

For the brightest source, S9, there is an offset of  $0.6 \pm 0.2$  arcsec between the Ly- $\alpha$  centroid and then centroid of the continuum source. The same offset is also seen in the 2-dimensional spectrum of the source (Fig. 2, the slit was nearly aligned along the direction of the offset). To assess whether a likely explanation for this is that we see two sources superposed, we calculate the probability for a chance alignment along the line of sight. The surface density of galaxies down to the 5 detection limit in the VLT B-band image is 50 per arcmin $^2$ . The probability to find a galaxy by chance within 0.6 arcsec from a given position on the sky is therefore roughly  $\times 0.6^2 \times 50/3600 = 1.6\%$ . The probability of such a chance alignment in one of six cases is hence roughly 10%, which is small but not negligible. Therefore, with the present data we cannot conclude whether S9 is a single object with strong Ly- $\alpha$  emission centred 0.6 arcsec from the continuum emission, or a chance alignment of two objects. Note here that evidence that the spatial distribution of Ly- $\alpha$  emission of high-redshift galaxies can be different from that of the continuum emission of the same galaxy, was reported by Møller and Warren (1998) and Roche et al. (2000).

### Spectroscopy

The individual spectra of S7–S12 are shown in Fynbo et al. (2001a). All 6 sources have confirmed emission lines. In the middle panel of Figure 3, we show the composite spectrum of all 6 sources in the spectral region

4600 Å–5270 Å around the emission line (left) and in the spectral region 6050Å–6720Å (right). As seen, there is one strong emission line detected in the blue part of the spectrum. This line could be due to a foreground emission-line galaxy at  $z = 0.313$  with [OII] 3727 in the narrow filter, or Ly- $\alpha$  at  $z = 3.036$ . To discriminate between the two possibilities we look for the presence of other lines. In the lower panel we show the spectrum of a  $z = 0.224$  (B(AB) = 24.2) emission-line galaxy detected in one of the redundant slits. This spectrum has been redshifted to  $z = 0.313$  so that the [OII] 3727 emission line falls at the same wavelength as the observed emission lines of S7–S12. With dashed, vertical lines we indicate the positions of the [NeIII], H and [OIII] emission lines seen in the spectrum of the  $z = 0.313$  galaxy. As seen, there is no hint of these lines in the composite spectrum of S7–S12, which confirms that S7–S12 indeed are high redshift

Ly- $\alpha$  emitters and not foreground emission-line galaxies. In the upper panel we show the spectrum of Q1205-30 in the same spectral regions as for S7–S12 to illustrate, in the same way, that there is no CIV emission from S7–S12. Hence, the Ly- $\alpha$  emission is most likely powered by star-formation.

These results show that Ly- $\alpha$  selection allows the study of high-redshift galaxies that are currently not accessible with the Lyman-Break technique. The inferred space density of S7–S12 is about 10 times higher than that of  $R < 25.5$  Lyman-Break galaxies (Fynbo et al. 2000a). Only ~ 20% of the Lyman-Break galaxies show Ly- $\alpha$  in emission (Steidel et al. 2000). This may be an underestimate if Ly- $\alpha$  and continuum emission often have different spatial distributions. However, if this fraction is valid further down the luminosity function, then there could be 50 times more galaxies like S7–S12 than  $R < 25.5$  Lyman-Break galaxies. Of

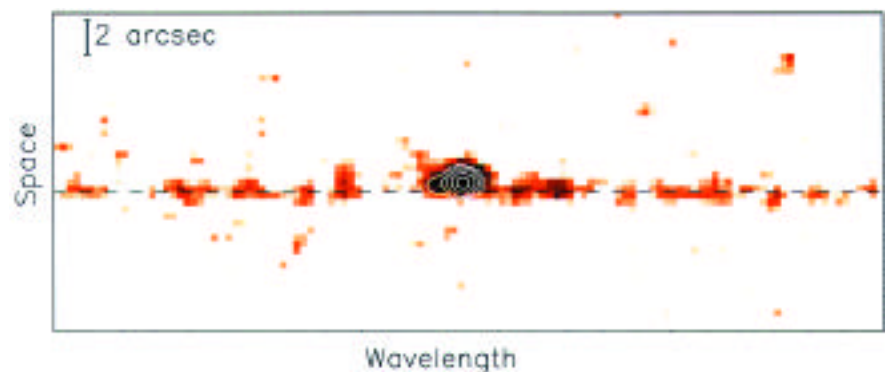


Figure 2: The 2-dimensional spectrum of the brightest Ly- $\alpha$  source, S9, showing the offset between the Ly- $\alpha$  emission and the continuum emission.

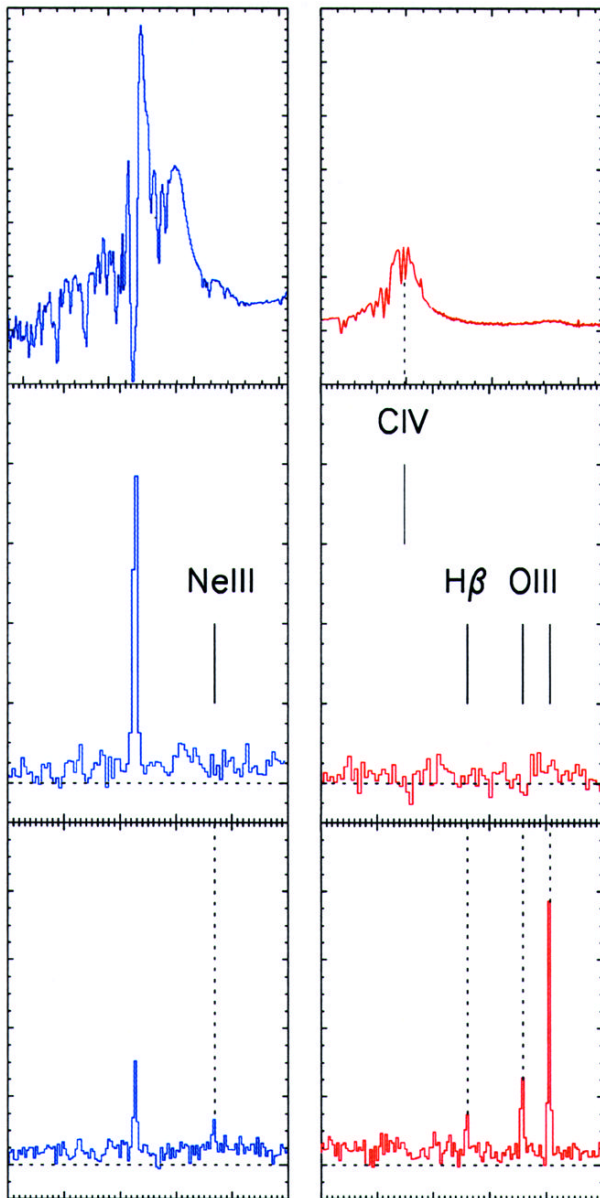


Figure 3: The middle panel shows the composite spectrum of S7–S12. The lower panels show the spectrum of an emission-line galaxy redshifted to  $z = 0.313$  so that the [OIII] line falls at the wavelength of the observed emission line of S7–S12. As seen, the composite spectrum of S7–S12 shows none of the lines expected if S7–S12 had been foreground emission-line galaxies. The upper panels show the spectrum of Q1205-30 to indicate the position of the CIV emission expected for AGNs. The absence of CIV emission from S7–S12 shows that the Ly- $\alpha$  emission is powered by star-formation and not by a central AGN.

course we need to measure the space density of faint Ly- $\alpha$  emitters to similar depths as in the field of Q1205-30 in several (blank) fields before this conclusion can be drawn.

### GRB Host Galaxies

In some widely accepted scenarios, GRBs are related to the deaths of very massive, short-lived stars and furthermore gamma-rays are not obscured by dust. Hence, a sample of GRB host galaxies may be considered star-formation-selected independent of the amount of extinction of the rest-frame UV and optical emission.

Several high-redshift galaxies have been localised as host galaxies of GRBs. A Lyman-Break type galaxy at redshift  $z = 3.42$  with an R-band magnitude of  $R = 25.6$  (and a prominent Ly- $\alpha$  emission line) was found to be the host galaxy of GRB 971214 (Kulkarni et al. 1998; Odewahn et al. 1998). GRB 990123 and GRB 990510 occurred at nearly identical redshifts ( $z \sim 1.6$ ), but

the host galaxy of the former ( $R = 24.6$ ) is more than 20 times brighter than the latter ( $R = 28$ ) (Holland and Hjorth 1999; Fruchter et al. 1999, 2000a). In the same way, GRB 000301C and GRB 000926 occurred at  $z = 2.0404$  and  $z = 2.0375$ , but have very different host galaxies. The host galaxy of GRB 000301C remains undetected down to a detection limit of  $R = 28.5$  (Fruchter et al. 2000b; Smette et al. 2001; Jensen et al. 2001), whereas the host galaxy of GRB 000926 is relatively bright ( $R = 24$ , Fynbo et al. 2001b). Finally, no host galaxy has been detected for GRB 000131, that occurred at  $z = 4.50$ , down to a limit of  $R = 25.7$  (Andersen et al. 2000).

If GRBs indeed trace star-formation, these observations indicate that at these redshifts galaxies covering a broad range of luminosities contribute significantly to the overall density of star formation. Furthermore, as the observed R-band flux is proportional to the star-formation rate, there must be 1–2 orders of magnitude more galaxies at the  $R = 28$  level than at the  $R = 24$

level at  $z = 2$ . Otherwise it would be unlikely to detect  $R = 28$  galaxies as GRB hosts.

### Conclusion: Faint Galaxies at High Redshifts

The study of Damped Ly-Absorbers (Fynbo et al. 1999; Haehnelt et al. 2000), Ly- $\alpha$  selected galaxies and GRB host galaxies independently suggest that there are 1–2 orders of magnitude more galaxies fainter than  $R \approx 25.5$  than brighter than this limit at  $z = 2–4$ . The properties of galaxies at this faint end of the luminosity function are currently very uncertain. Since the population of bright, Lyman-Break selected galaxies is already (observationally) very well studied and characterised, progress in the understanding of the high-redshift galaxy population will most likely come from the study of galaxies below the spectroscopic limit.

### References

- Andersen M. I., Hjorth J., Pedersen H., et al., 2000, *A&A* **364**, L54.  
 Cowie L. L., Hu E. M., 1998, *AJ* **115**, 1319.  
 Cristiani S., Appenzeller I., Arnout S., et al., 2000, *A&A* **359**, 489.  
 Fynbo J. U., Møller P., Warren S. J., 1999, *MNRAS* **305**, 849.  
 Fynbo J. U., Thomsen B., Møller P., 2000a, *A&A* **353**, 457.  
 Fynbo J. U., Thomsen B. Møller P., 2000b, *The Messenger* **95**, 32.  
 Fynbo J. U., Gorosabel J., Dall T. H., et al., 2001a, submitted to *A&A*.  
 Fynbo J. U., Møller P., Thomsen B., 2001a, submitted to *A&A*.  
 Francis P. J., Woodgate B. E., Warren S. J., et al., 1995, *ApJ* **457**, 490.  
 Fruchter A., Thorsett S. E., Metzger M. R., et al., 1999, *ApJ* **519**, L13.  
 Fruchter A., Hook R., Pian E., 2000a, GCN 757.  
 Fruchter A., Metzger M., Petro L., 2000b, GCN 701.  
 Haehnelt M. G., Steinmetz M., Rauch M., *ApJ* **534**, 594.  
 Holland S., Hjorth J., 1999, *A&A* **344**, L67.  
 Jensen B. L., Fynbo J. U., Gorosabel J., et al., 2001, *A&A* submitted (astro-ph/0005609).  
 Kudritzki R.-P., Méndez R.H., Feldmeier J.J., et al., 2000, *ApJ* **536**, 19.  
 Kulkarni S. R., Djorgovski S. G., Ramaprakash A. N., et al., 1998, *Nat* **393**, 35.  
 Kurk J. D., Röttgering H. J. A., Pentericci L., et al., 2000, *A&A* **358**, L1.  
 Roche N., Lowenthal J., Woodgate B., 2000, *MNRAS* **317**, 937.  
 Møller P., Warren S. J., 1993, *A&A* **270**, 43.  
 Møller P., Warren S. J., 1998, *MNRAS* **299**, 661.  
 Odewahn S. C., Djorgovski S. G., Kulkarni S. R., et al., 1998, *ApJ* **509**, L5.  
 Pascarella S. M., Windhorst R. A., Keel W. C., 1998, *AJ* **116**, 2659.  
 Smette A., Fruchter A. S., Gull T. R., et al., 2001, *ApJ* in press (astro-ph/0007202).  
 Steidel C. C., Giavalisco M., Pettini M., Dickinson M., Adelberger K., 1996, *ApJ* **462**, L17.  
 Steidel C. C., Adelberger, Shapley A. E., et al., 2000, *ApJ* **532**, 170.

# Discovery of a Bow-Shock Nebula Around the Pulsar B0740-28

H. JONES (ESO Chile); B. STAPPERS (University of Amsterdam); B. GAENSLER (MIT)

Bow-shock nebulae around high-velocity pulsars provide our primary insight into the interaction between a pulsar and its surrounding environment. Specifically, optical observations of such nebulae allow us to derive full three-dimensional pulsar velocities which are extremely important for the birth rates and evolution of pulsars. They can also provide important information on the density, temperature and composition of the surrounding ambient medium. Unfortunately, only a few bow-shock nebulae have been discovered, despite there being nearly a thousand pulsars known from radio surveys. We have therefore commenced a search for pulsar bow-shocks, using the results to characterise the properties of the associated pulsars, pulsar winds and ambient environments.

During the first two nights of this programme (January 4 and 5, 2001), we discovered an optical bow-shock nebula around the radio pulsar B0740-28 using SUSI2 at the NTT. Prior to this, only four pulsars were known to power optical bow-shock nebulae (see Cordes 1996 and references therein), and only one of these at southerly declinations (J0437-4715; Mann, Romani & Fruchter 1999).

Figure 1 shows H $\alpha$  images of a newly-discovered nebula associated with PSR B0740-28 (Fig. 1a, top), and of the (previously known) bow-shock associated with PSR J0437-4715 (Fig. 1b, bottom). Each was taken through the 656/7 filter of SUSI2 and is 1 arcmin on a side with north to the top and east to left. The B0740-28 image is the result of nearly 2 hours of integration while that for J0437-4715 was obtained in a little more than 30 minutes. The faint star directly behind the shock front of J0437-4715 is a white dwarf companion to the pulsar (which is not seen in the optical). Both images were treated using standard techniques for bias and flat-field signature removal, image registration and then co-addition. CCD defects and cosmic rays were removed using cross-pixel interpolation on the final frame rather than filtering through the stack, in order to preserve as much of the faint nebula signal as possible. A residual background was subtracted separately from the B0740-28 image, presumably arising from scattered moonlight on one of the nights. Finally, the nebula counts were top-hat filtered out and smoothed before being recombined with the original, to increase the contrast of the object against the sky background. The

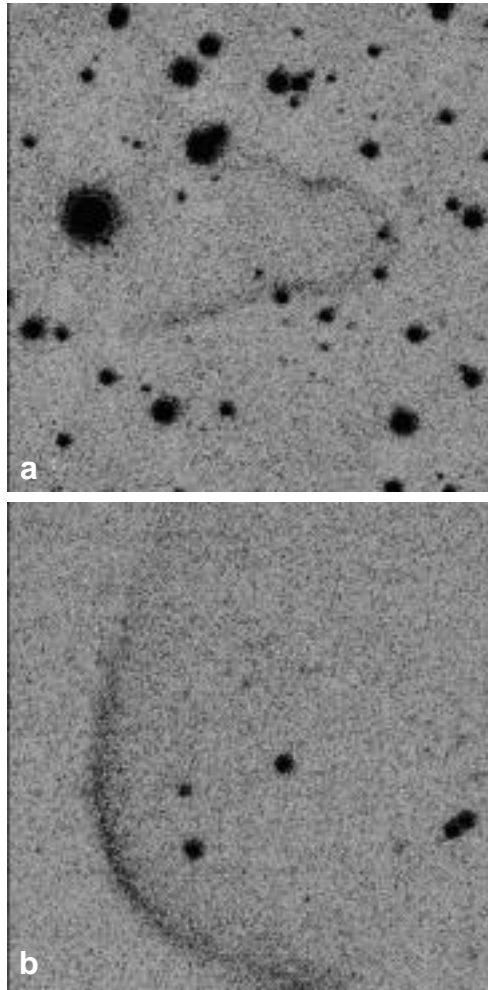


Figure 1: Two pulsar-powered bow-shock nebulae imaged in H $\alpha$  on 4–5 January 2001 at the NTT. (a) The newly-discovered nebula associated with PSR B0740-28 (the pulsar is located about 1 arcsec to the left of the head of the bow shock) and (b) the bow-shock associated with PSR J0437-4715. The star directly behind the shock front is a companion to the pulsar which itself is not detected in the optical. Images are 1 arcmin on a side with north up, east left.

continuum component was not separately observed and so has not been subtracted in either case.

The images in Figure 1 show the nebula associated with PSR B0740-28 to have a closed cometary morphology, more like the nebula around PSR B2224+65 (the “Guitar” nebula; Cordes, Romani & Lundgren 1993) than the open bow-shock of PSR J0437-4715. Like the bow-shock associated with PSR B2224+65, the B0740-28 nebula has a distinct key-hole shape, with the spherical head of the shock-front protruding from the fanned tail. The position of the pulsar (about 1

arcsec to the left of the head of the bow-shock), and the measured proper motion for the pulsar of 29 mas/yr westwards (Bailes et al. 1990), confirm the bow-shock interpretation for the nebula.

All of the pulsars with known bow-shock nebulae in the optical have high energy loss due to spin-down and/or high velocities (including the recent addition of PSR B0740-28). However, at the same time, they exhibit a diverse range of spin periods, ages and magnetic field strengths, highlighting the variety of pulsar winds which can be probed by these sources. The recently-discovered nebula associated with a so-called “radio-quiet” neutron star further exemplifies the variety of neutron star forms known to power nebulae (van Kerkwijk 2000, ESO press release 19/00).

Detailed studies of nebular emission, such as that carried out on B1957+20 by Aldcroft et al. (1992), enable a determination of not only the nature of the shock and the properties of the ambient ISM, but also of the kinematic distance to the pulsar. Such a distance determination is essential of course in improving our understanding of the individual system, but also allows an independent test of the pulsar distance scale as determined by its dispersion measure. We are currently in the process of doing this for B0740-28, and in doing so, solve another small piece of the puzzle.

However, the first step towards a general understanding of these fascinating objects is to build a sample of them sufficiently large that it canvasses the full range of conditions encountered. This is the main aim of our continuing survey.

We would like to thank the NTT Team for their assistance with various aspects of the run, particularly Support Astronomers Stephane Brilliant and Pierre Leisy, and telescope operator Duncan Castex.

## References

- Aldcroft et al., 1992, *ApJ*, **400**, 638.
- Bailes et al., 1990, *MNRAS*, **247**, 322.
- Cordes, Romani & Lundgren, 1993, *Nature*, **362**, 133.
- Cordes, 1996, in IAU Colloq. **160**, p. 393.
- Kennel & Coroniti, 1984, *ApJ*, **283**, 710.
- Kulkarni et al., 1992, *Nature*, **359**, 300.
- Mann, Romani & Fruchter, 1999, *BAAS*, **195**, 41.01.
- Michel, 1982, *Rev Mod Phys*, **54**, 1.
- Rees & Gunn, 1974, *MNRAS*, **167**, 1.

# Young Stellar Clusters in the Vela D Molecular Cloud

L. TESTI<sup>1</sup>, L. VANZI<sup>2</sup>, F. MASSI<sup>3</sup>

<sup>1</sup>Osservatorio Astrofisico di Arcetri, Florence, Italy; <sup>2</sup>European Southern Observatory, Santiago, Chile

<sup>3</sup>Osservatorio Astronomico di Teramo, Teramo, Italy

It is now well established by means of direct and indirect observations that most, if not all, stars are formed in groups rather than in isolation (Clarke, Bonnell & Hillenbrand 2000). An important result that strongly constrains theories of massive star and stellar cluster formation is that the stellar density of young stellar clusters seems to depend on the mass of the most massive star in the cluster. Low-mass stars are usually found to form in loose groups with typical densities of a few stars per cubic parsec (Gomez et al. 1993), while high-mass stars are found within dense stellar clusters of up to  $10^4$  stars per cubic parsec (e.g. the Orion Nebula Cluster, Hillenbrand & Hartmann 1998). To explain this different behaviour, it has been proposed that massive stars may form with a process that is drastically different from the standard accretion picture, e.g. by coalescence of lower mass seeds in a dense cluster environment. The transition be-

tween these two modes of formation should occur in the intermediate-mass regime, namely  $2 \leq M/M_{\odot} \leq 15$ .

In order to probe this transition, Testi et al. (1999) recently completed an extensive near infrared (NIR) survey for young clusters around optically visible intermediate-mass stars (Herbig Ae/Be stars) in the northern hemisphere. The main result of this survey is that there is a strong correlation between the spectral type of the Herbig Ae/Be stars and the membership number of the stellar groups around them. Furthermore, there is compelling evidence that the most massive stars in their sample are surrounded by *denser*, not simply more populous clusters. These findings are in qualitative agreement with models that suggest a causal relationship between the birth of a massive star and the presence of rich stellar clusters. The observed correlation and scatter, however, could also be explained in terms of random assembling clusters

with membership size distribution of the form  $g(N) \sim N^{-1.7}$  picking stars from a standard IMP (Bonnell & Clarke 1999). In this view, since massive stars are rare objects compared to low-mass stars, they will be observed only as members of large ensembles of stars (clusters), while the detection of an isolated high-mass star would have a relatively low probability. As discussed in Testi et al. (2001), there are two observational strategies to provide additional constraints on which of the two models is the most appropriate: to expand the sample of optically revealed young O and B stars to increase the statistics, and to search for clusters in complete samples of luminous embedded sources in giant molecular clouds. The young high-mass isolated objects predicted by the random model should be detected in such surveys. However, to properly compare with the models, it is essential to carry out observations around the target luminous objects

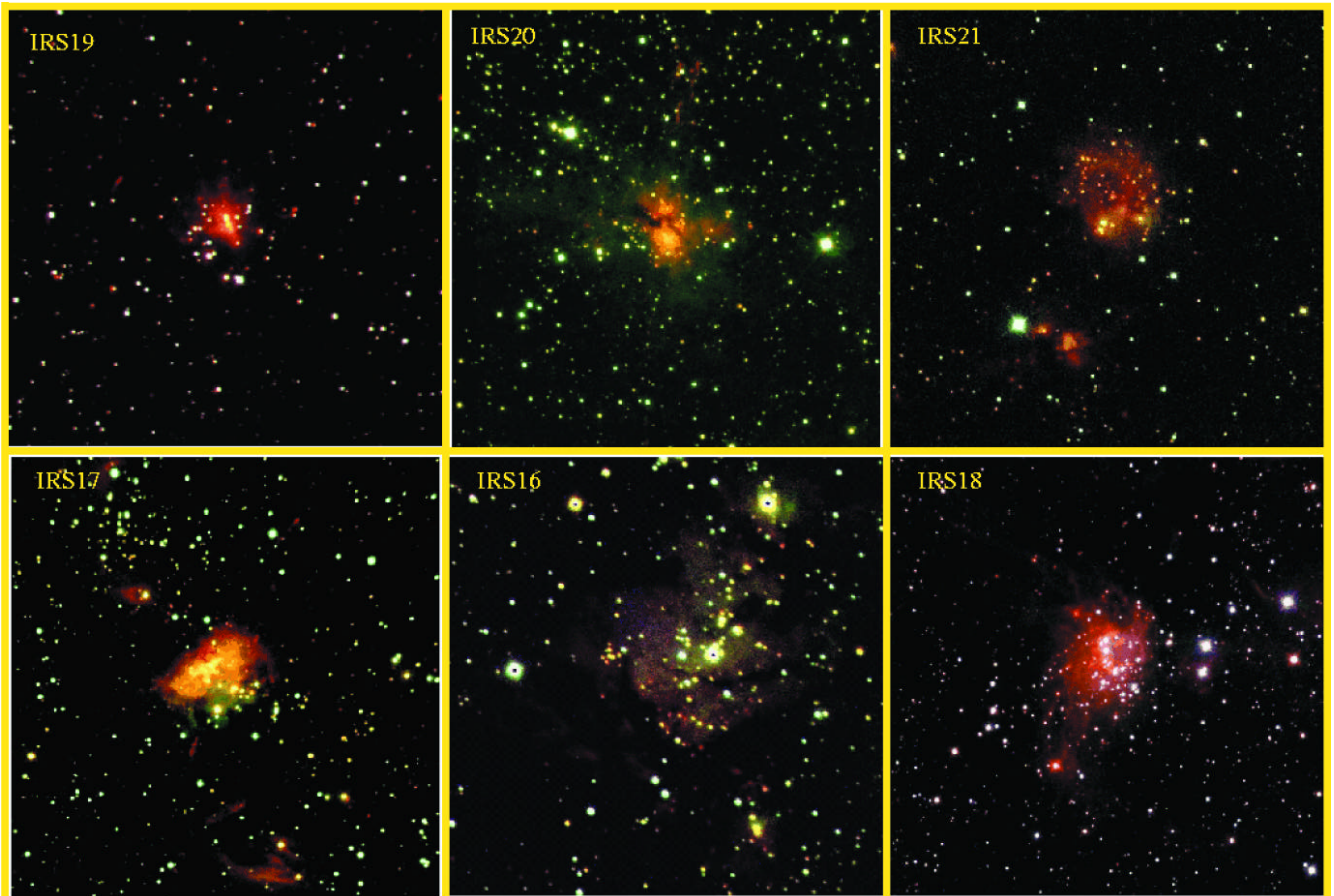


Figure 1: NTT/SOFI near infrared “true-colour” images ( $J$  blue,  $H$  green,  $K_s$  red) of the fields centred on the luminous IRAS sources in the Vela D molecular cloud. The sources are ordered by increasing far infrared (IRAS) luminosity from left to right and top to bottom.

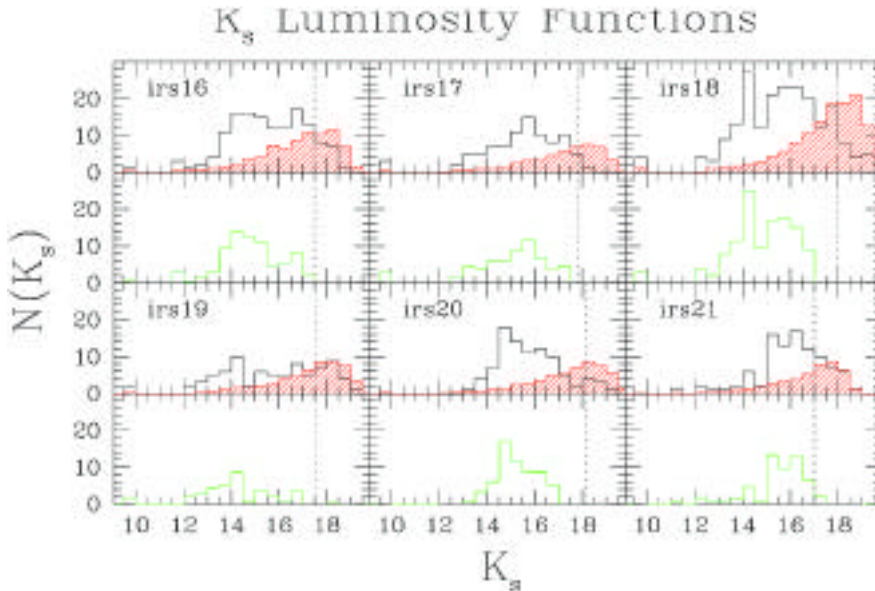


Figure 2:  $K_s$  luminosity functions for the observed sample. For each field in the top panel we show the observed  $K_s$ LF at the image centre (black histogram) and at the edges (red shaded histogram), normalised to the same area. The estimated  $K_s$ LF of each cluster, obtained by subtracting the “edge” from the “central”  $K_s$ LFs, are shown in the bottom panels as green histograms. The dotted vertical lines mark the  $K_s$  completeness magnitude.

complete down to at least  $0.1\text{--}0.2 M_\odot$  over a field of view large enough to cover the expected cluster size. The NTT/SOFI combination, with the provided field of view and sensitivity is an ideal asset to collect the required data and settle this fundamental issue. Moreover, due to the reduced extinction compared to the optical, the near infrared bands (especially  $K_s$ ) are the most effective for this type of studies, in fact the young clusters are expected to be at least partially embedded within their parent molecular cloud core. In this paper we report on the results of a study of a complete sample of luminous IRAS sources in the Vela-D giant molecular cloud.

### 1. The Vela-D Luminous IRAS Sources

Low-resolution observations in the CO(1–0) mm-line of the region of the galactic plane defined by  $255^\circ \leq l \leq 275^\circ$ ,  $-5^\circ \leq b < +5^\circ$  carried out by Murphy & May (1991) uncovered the existence of an emission ridge in the range  $0 \leq v_{\text{LSR}} \leq 15 \text{ km s}^{-1}$  which was promptly dubbed “Vela Molecular Ridge” (VMR). These authors found the molecular gas complex to be made out of four main molecular clouds that they indicated as A, B, C and D,  $\sim 10^5 M_\odot$  each. Liseau et al. (1992) studied the association of luminous IRAS sources with the VMR and selected among them a complete sample of protostellar objects based on IRAS colours, their spectral slopes from the near- to the far-infrared and the velocity of the parental molecular gas. They also discussed the distance of the VMR, concluding that clouds ACD are likely to be located  $\sim 700 \pm 200 \text{ pc}$  from the Sun.

On this basis, they found no O-type stars recently having been formed in the VMR, although birth of intermediate-mass stars is in progress. Massi et al. (1999, 2000) examined in detail NIR images of the subsample of IRAS protostellar sources (12) belonging to the D cloud, concluding that most of their bolometric luminosity arises from single young stellar objects (or close pairs of young stellar objects) of intermediate mass embedded in young stellar clus-

ters. We selected the most luminous ( $L_{\text{bol}} > 10^3 L_\odot$ ) IRAS sources in the subsample of Massi et al. (1999, 2000), namely IRS 17, 18, 19, 20 and 21 (following the classification of Liseau et al. 1992), adding IRS 16, a source not included by Liseau et al. (1992) in their final list of protostellar objects associated with the VMR possibly because of its failure in fulfilling some of the rather conservative selection criteria chosen, although lying toward an HII region.

Our observations were designed to reach at  $K_s$  band a completeness magnitude high enough to be sensitive to all stars more massive than  $0.1 M_\odot$  in all the clusters. From the observations of Massi et al. (2000), the age of all known young clusters in our sample is less than 1 Myr and the visual extinction much less than 30 mag, as derived from the brightest members of the clusters. Using the methods described in Testi et al. (1998) and the PMS evolutionary tracks from Palla & Stahler (1999), these constraints translate in a required  $K_s$  completeness magnitude of  $\sim 17$ , this figure having been used to design the observing strategy and integration times. The expected cluster sizes were estimated from the Testi et al. (1999) and Massi et al. (2000) surveys, which found an average cluster radius of 0.2 pc, corresponding to  $\sim 1$  arcmin at the distance of the Vela D cloud.

The clusters were observed with SOFI at the NTT through the J, H and  $K_s$  broad-band filters and with the large-field objective offering an instantaneous field coverage of  $\sim 5$  arcmin with

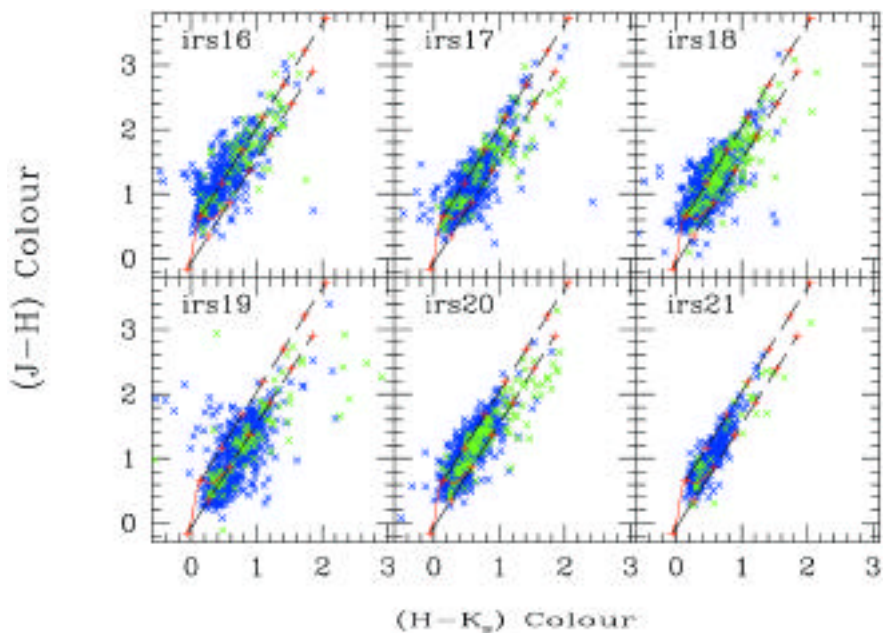


Figure 3:  $(J-H)$  vs.  $(H-K_s)$  colour-colour diagrams for the six observed regions. Sources within one arcminute from the field centres are shown in green, sources further away are shown in blue. The red line marks the location of main sequence, non reddened stars. The reddening vectors are shown as dashed lines with a red cross every 5 magnitudes. Sources in the inner regions show on average redder colours, some of them exhibit an infrared excess, typical of young stellar objects. Only very few sources are affected by extinction exceeding 25 mags in the visual.

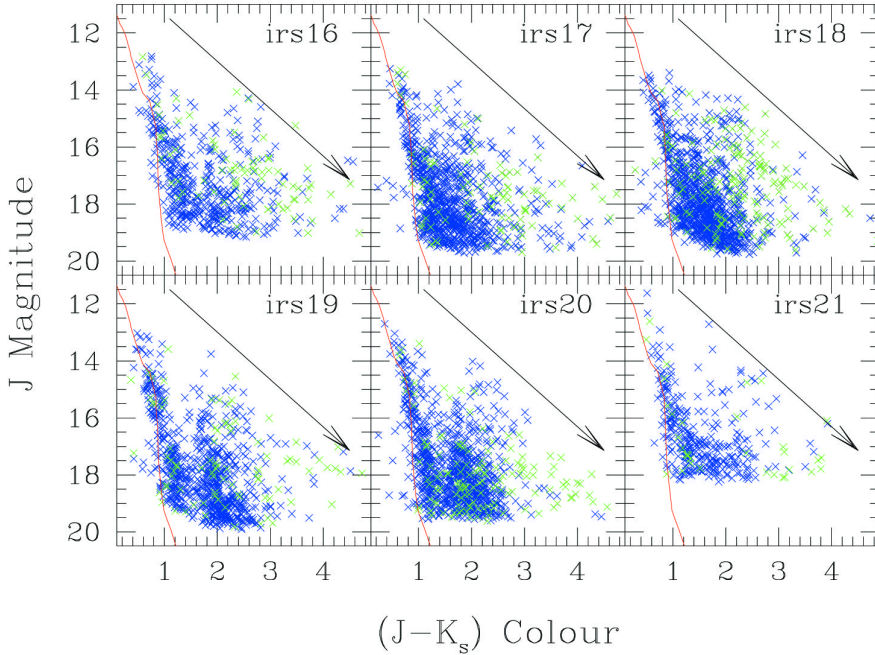


Figure 4:  $J$  vs.  $(H-K_s)$  colour-magnitude diagrams for the six observed regions. Sources within one arcminute from the field centres are shown in green, sources further away are shown in blue. The red line marks the location of main sequence, non reddened stars. The arrows show the direction of the reddening vectors and its length correspond to a visual extinction of 20 mag.

a pixel scale of 0.292 arcsec. We integrated for  $\sim 15$  minutes per filter and cluster. Object and sky were alternatively observed to have a good sampling of the background variations. The images were reduced following the standard procedure and the “Special FlatField” technique. After combining the dithered frames, the final image quality is  $\sim 0.85$  arcsec for all fields but IRS 16, which was observed under worse seeing conditions (1.1 arcsec).

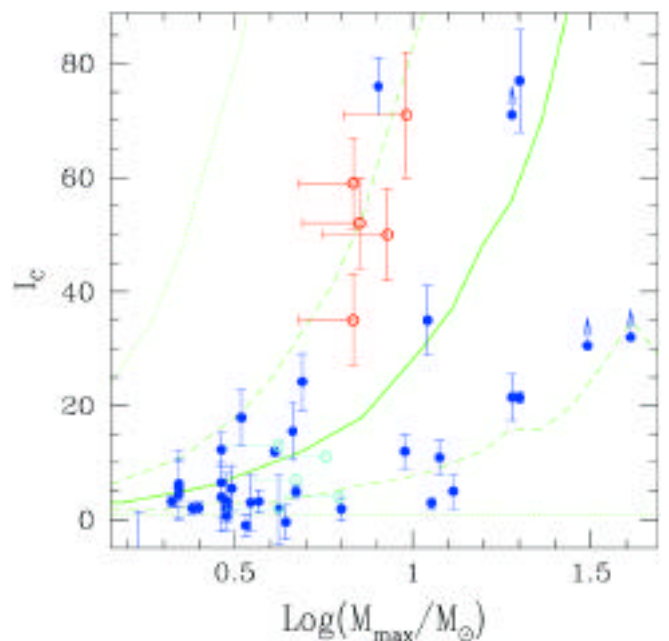
## 2. Results

In Figure 1 we show a subsection of the NTT/SOFI near infrared “true-colour” images of the fields surrounding the six IRAS sources that we surveyed. From the images it is immediately clear that we detected groups of very red sources in every field, and an increase of the stellar surface density toward the centre, where the luminous IRAS sources are located, is also evident. All clusters are embedded within a diffuse nebulosity, likely due to cluster members light scattered toward the line of sight by the dust in which the younger sources are still embedded. In a few cases, IRS 17 and IRS 20 are the most evident, we clearly detect in the  $K_s$  broad-band filter the line emission from collimated jets (see also Massi et al. 1997 for a narrow-band survey of the region) emerging from the inner regions of the clusters, confirming the youth of the objects.

More quantitatively the presence of an excess of (relatively) bright sources toward the map centres can be made clear by comparing  $K_s$ -band luminosity

functions of the central regions with those of the image edges. In Figure 2, we show such comparison for all fields on our sample. In all cases, the presence of a cluster near the centre is clearly indicated by the excess of luminous sources with respect to the edge regions. In Figure 2 we also show the  $K_s$  completeness magnitudes for each field. As expected, our observations are deep enough to obtain a complete census of whole relevant young stellar population in all clusters. Additionally, we note that the derived cluster  $K_s$ LFs are all sharply declining above our completeness limits, suggesting that either

Figure 5:  $I_C$  versus maximum stellar mass for the luminous young clusters in the Vela D molecular cloud (red open circles), compared with the results toward low luminosity sources in the same cloud (cyan open circles) and the Herbig Ae/Be sample (blue filled circles). The prediction of the “random” model (see text) are shown in green: median results (solid line), 50% of the realisations (dashed lines), and 98% of the realisations (dotted lines).



the relative number of sub-stellar objects in the Vela D cluster is smaller than in other cluster forming regions (such as the Orion Nebula Cluster, Hillenbrand & Carpenter 2000), or that most of the sources within the clusters are affected by a visual extinction much lower than the  $A_V = 30$  mag value that we have assumed to compute the sensitivity estimates. This latter explanation is in agreement with the near infrared colour-colour and colour-magnitude diagrams shown in Figures 3 and 4, where sources within 1 arcmin from the image centres are shown in green. On average, they show redder colours than sources further away from the centre and a fraction of them display a clear infrared excess, typical of young stellar objects. In the figures, the reddening vectors and the main sequence loci are also displayed, only very few sources are consistent with an extinction greater than 20 mag in the visual.

To obtain a quantitative estimate of the richness of the detected young stellar clusters, we followed the method described in Testi et al. (1999) and derived the richness indicator  $I_C$  for all six sources.  $I_C$  gives the “effective” number of cluster members, since it is defined as the integral of the radial  $K_s$  stellar surface density profile centred on the peak stellar surface density and corrected for the foreground/background stellar density as computed on the edge of the images. In Figure 5, we show  $I_C$  as a function of the maximum stellar mass in each cluster for the high-luminosity sources in the Vela D cloud compared with the results of Testi et al. (1999) toward Herbig Ae/Be systems and the low luminosity sources in the Vela D cloud (Massi et al. 2000). The mass sensitivity of our NTT survey is similar to the estimated mass sensitivity of the Herbig Ae/Be survey, while the

Massi et al. survey of low-luminosity sources in the Vela D cloud has a slightly lower sensitivity. The maximum stellar masses in the Vela clusters have been computed assuming that a fraction of the total luminosity ranging from 30% to 100% is emitted by the most massive object. The young IRAS sources in the Vela molecular cloud show the same trend as the Herbig Ae/Be stars: more massive stars are surrounded by rich clusters, while low-mass stars are found in relative isolation.

In the same plot, the result of the various surveys are compared with the predictions of a "random sampling model" (as described in Testi et al. 2001). Our results clearly deviate from the prediction of the model, since no massive object is found in isolation, and all lie above the median predictions of the model. These results suggest that there is a physical connection between clusters and high-mass stars. This

does not necessarily *imply* that massive stars are formed by coalescence in (proto-)cluster environments, but suggests that the conditions to form a massive star are such that this process is associated with the formation of a cluster of (lower-mass) objects. The cluster could be either the catalyst of high-mass star formation or a by-product of it.

These conclusions should and will be made more firm by combining larger samples from various surveys toward different regions.

## References

- Bonnell I. A., & Clarke C. J., 1999, *MNRAS*, **309**, 461.  
 Clarke C. J., Bonnell I. A., & Hillenbrand L. A., 2000, in *Protostars and Planets IV*, eds. V. Mannings, A. Boss & S. S. Russell (Tucson: University of Arizona press), p. 151.  
 Gomez M., Hartmann L., Kenyon S. J., Hewett R., 1993, *AJ*, **105**, 1927.

- Hillenbrand L. A. & Hartmann L. W., 1998, *ApJ*, **492**, 540.  
 Hillenbrand L. A. & Carpenter J. M., 2000, *ApJ*, **540**, 236.  
 Liseau R., Lorenzetti D., Nisini B., Spinoglio L., Moneti A., 1992, *A&A* **265**, 577.  
 Massi F., Lorenzetti D., Vitali F.: "Near Infrared H<sub>2</sub> imaging of YSOs in Vela Molecular Clouds" in Malbet F., Castets A. (eds.), *Low Mass Star Formation from Infall to Outflow – Poster Proceedings of the IAU Symposium n. 182 on Herbig-Haro Flows and the Birth of Low Mass Stars*, Observatoire de Grenoble 1997.  
 Massi F., Giannini T., Lorenzetti D. et al., 1999, *A&AS* **136**, 471.  
 Massi F., Lorenzetti D., Giannini T., Vitali F., 2000, *A&A* **353**, 598.  
 Murphy D. C., May J., 1991, *A&A* **247**, 202.  
 Palla F. & Stahler S.W., 1999, *ApJ*, **525**, 772.  
 Testi L., Palla F., Natta A., 1998, *A&AS*, **133**, 81.  
 Testi L., Palla F., Natta A., 1999, *A&A*, **342**, 515.  
 Testi L., Palla F., Natta A., 2001, in "From Darkness to Light", eds. T. Montmerle and Ph. André, ASP Conf. Series, in press.

# Building Luminous Blue Compact Galaxies by Merging

P. AMRAM<sup>1</sup> AND G. ÖSTLIN<sup>2</sup>

<sup>1</sup>Observatoire de Marseille, France; <sup>2</sup>Stockholm Observatory, Sweden

## ABSTRACT

*Observations of six luminous blue compact galaxies (LBCGs) and two star-forming companion galaxies were carried out with the CIGALE scanning Fabry-Perot interferometer attached to the ESO 3.6-m telescope, targeting the H $\alpha$  emission line. The gaseous velocity field presents large-scale peculiarities, strong deviations to pure circular motions and sometimes, secondary dynamical components. In about half the cases, the observed rotational velocities are too small to allow for pure rotational support. If the gas and stars are dynamically coupled, a possible explanation is either that velocity dispersion dominates the gravitational support or the galaxies are not in dynamical equilibrium, because they are involved in mergers, explaining the peculiar kinematics. In two cases, we find evidence for the presence of dark matter within the extent of the H $\alpha$  rotation curves and in two other cases we find marginal evidence. For most of the galaxies of the present sample, the observed peculiarities have probably as origin merging processes; in five cases, the merger hypothesis is the best way to explain the ignition of the starbursts. This is the most extensive study as yet of optical velocity fields of luminous blue compact galaxies.*

## 1. Introduction

A Blue Compact Galaxy (BCG) is characterised by blue optical colours,  $-21 < M_B < -12$ , an HII-region-like emission-line spectrum, a compact appearance on photographic sky-survey plates, small to intermediate sizes, high star-formation rates per unit luminosity and low chemical abundances (e.g. Searle and Sargent, 1972). Moreover, most BCGs are rich in neutral hydrogen. There is no consensus on the process(es) that trigger the bursts of star formation. Three main scenarios have been proposed to explain it: (1) cyclic infall of cooled gas: Starbursts

are terminated by SN winds, but when gas later accretes back, a new starburst may be ignited; (2) galaxy interactions and (3) collapse of protocloud if BCGs are genuinely young galaxies. Most arguments have been based on photometry alone. On the other hand, the dynamics of these systems are not well explored, still the creation of an energetic event like a sudden burst of star formation is likely to have dynamical causes and impacts, complicating the interpretation.

To improve our understanding of the dynamics and the triggering mechanisms behind the starburst activity, we have obtained Fabry-Perot data allow-

ing us to achieve two-dimensional velocity fields with both high spatial and spectral (velocity) resolutions. BCGs are obviously the galaxies for which 2-D data are absolutely requested due to the non-axisymmetry of the velocity field around the centre of mass.

The selected BCGs are among the more luminous ones known in the nearby universe. The galaxies were observed at the H $\alpha$ -emission line with the ESO 3.6-m telescope on La Silla. The exposure times ranged between 24 minutes and 160 minutes. In Östlin et al. (1999), we presented and described the data: H $\alpha$  images, velocity fields, continuum maps and rotation curves. In

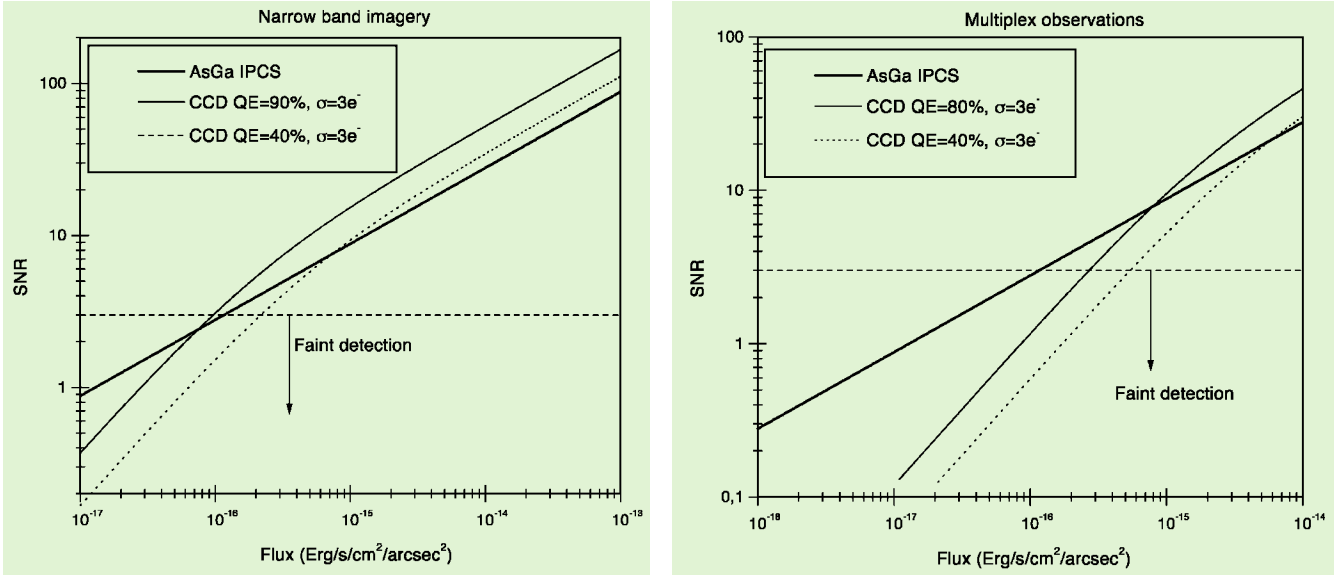


Figure 1: Comparison of the performances, expressed in terms of signal-to-noise ratio vs. the flux of the extended source for two CCDs (with different quantum efficiency) and an AsGa IPCS in a narrow-band imaging application (left) and in a multiplex application like a scanning Fabry-Perot interferometer (right). See text for further details.

Östlin et al. (2001), we will discuss the interpretation of these observations and their implications on the dynamics, the mass distribution and the triggering mechanism behind the starbursts.

In this paper, we give a flavour of the observations and provide some descriptions of two galaxies: ESO 350-IG38 and ESO 338-IG04. Then, we point out the hot spots of the sample and suggest an interpretation.

## 2. A Scanning Fabry-Perot Interferometer on the ESO 3.6-m

The instrument CIGALE attached to the Cassegrain focus of the ESO 3.6-m was used for the observations. CIGALE is basically composed of a focal reducer, a scanning Fabry-Perot interferometer, an interference filter and an IPCS (Image Photon Counting System). CIGALE (for Cinématique des GALaxiEs) is a visiting instrument belonging to Marseille Observatory, mounted for the first time on the ESO 3.6-m in 1991 and commissioned on the average for one run a year since that time. (In fact, a Fabry-Perot etalon plus an image tube has been mounted on the ESO 3.6-m by the Marseille team for the first time in 1979, see Marcelin et al., 1982). With the efficient cooperation of the 3.6-m ESO team and of the astro-workshop, using the facilities of the telescope, the instrument is easily mounted during the daytime of the first observing night. Several replica of this instrument exist throughout the world, one of them is presently extensively used on the OHP 1.93-m telescope (Observatoire de Haute-Provence, France) to provide a sample of about 200 velocity fields of nearby galaxies (the GHASP's project – Gassendi H $\alpha$  SPIral galaxies survey – see <http://www-obs.cursmrs.fr/interferometrie/GHASP/ghasp.html>).

The instrument CIGALE based at La Silla is used both on the ESO 3.6-m and on the Marseille 36-cm telescope. On the Marseille telescope, CIGALE has a wide field of view (40 arcmin square) and is used to make a kinematical deep H $\alpha$  survey of gaseous emission regions in the Milky Way and in the Magellanic Clouds (see for instance Georgelin et al., 2000). On the 3.6-m, CIGALE has a one hundred times smaller field ( $\sim 4$  arcmin square, providing a pixel size of 0.91 arcsec). The spectral scanning step depends on the interferometer used, it was of 4.8 km s<sup>-1</sup> for the present study. A full description of the instrument CIGALE is given in a previous paper in *The Messenger* (Amram et al., 1991). By the way, a previous discussion in *The Messenger* on BCGs (Infants of the Universe?) including ESO 338-IG04 can be found in Bergvall & Olofsson (1984). Data reduction was performed using the http available ADHOCw software (<http://www-obs.cnrs-mrs.friadhoc/adhoc.html>); a complete data-reduction procedure is given for instance in Amram et al. (1991, 1996). In August 1999 and in September 2000, two major upgrades were realised on CIGALE: the data-acquisition system and the receptor were removed. (1) Two hundred kg of electronics were substituted by a Matrox board allowing the acquisition of frames 1024  $\times$  1024 px<sup>2</sup> at high frequency and the computation in real time of the events on each frame. (2) The 20-year old Thomson IPCS was replaced by a new AsGa IPCS. The semi-conductor photocathode AsGa (built by Hamamatsu) of the new detector offers a d.q.e. five times higher (25% instead of 5% for the old Thomson IPCS). The output of the AsGa tube is coupled by optical fibers to a 1024  $\times$  1024 CCD. (<http://>

[www.observatoire.cnrs-mrs.fr/interferometrie/instrumentation.html#AsGa](http://www.observatoire.cnrs-mrs.fr/interferometrie/instrumentation.html#AsGa)). The IPCS, with a time resolution of 1/50 second and zero readout noise makes it possible to scan the interferometer rapidly, avoiding problems with varying sky transparency, airmass and seeing during long exposures; and thus has several advantages over a CCD for this application. Figure 1 compares the total efficiency of a CCD and an IPCS used in narrow-band imaging (left) and in multiplex application (right). It clearly shows that at low intensity level, the signal-to-noise ratio is much higher with an IPCS than with a CCD in the case of multiplex observations as for instance scanning Fabry-Perot interferometry. Figure 1 has been plotted from a simulation of one hour exposure time on an 8-metre telescope, for a pixel size of 0.25 arcsec square, 48 scanning channels, transmissions of: 80% for the atmosphere; 64% for the 2 mirrors of the telescope; 70% for the interference filter; 80% for the optics and 90% for the Fabry-Perot (Gach et al., 2001). The data presented here were obtained in August 1995 with the old system; new observations were performed for another 15 BCGs, extending down to fainter luminosities in 1999 and 2000 with the new system, this will allow us to obtain a more comprehensive picture on the evolution of BCGs.

## 3. Results: Description of Two BCGs

### 3.1 ESO 350-IG38 (Haro 11)

The morphology of this object is complex. The three bright starburst nuclei are composed of numerous individual super star clusters ( $M_V \geq -15$ , Östlin, 2000) as it can be seen for an HST/WFPC2 image (Fig. 2 – left,

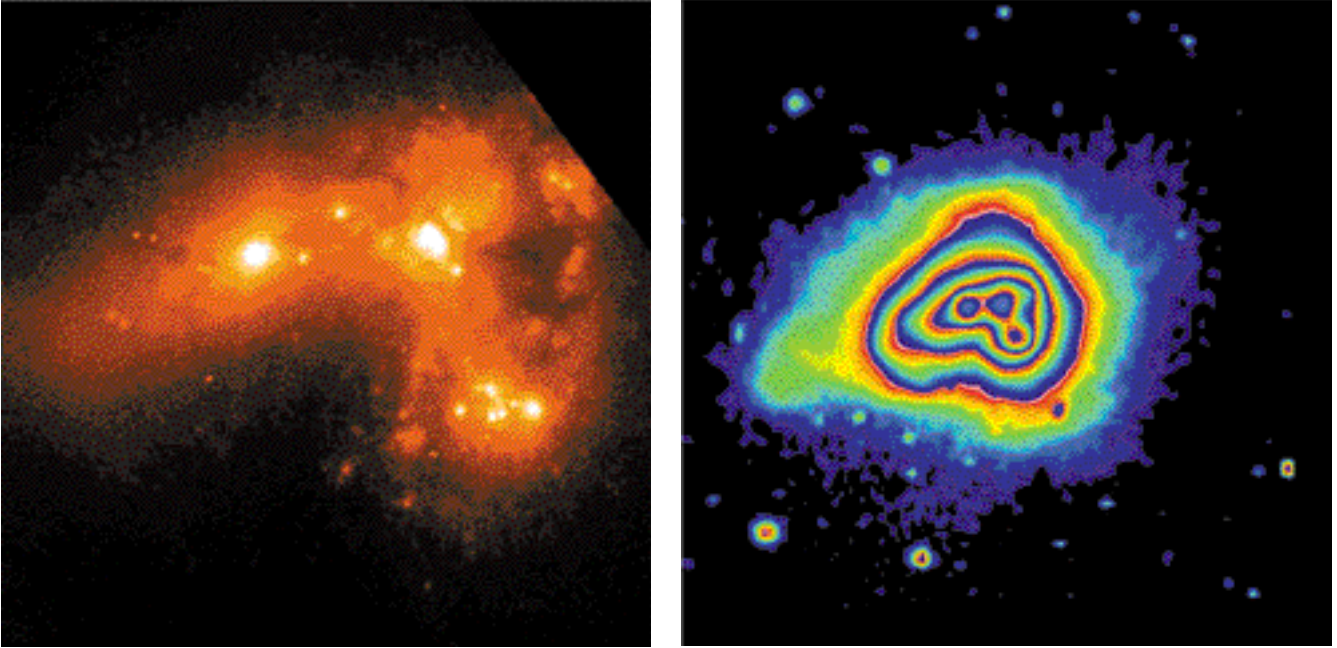


Figure 2: **ESO 350-IG38**. North is up, East is left. (Left): HST/WFPC2 V+R (F606W) broad-band image. The scale of the box is 24 arcsec square. (Right): R-band CCD image. Note the irregular morphology at all isophotal levels. The faintest visible structures are  $\mu_R \approx 26$  mag/arc<sup>2</sup>. The size of the field is 1 by 1 arcminute, corresponding to  $23 \times 23$  kpc.

Malkan et al. 1998). The properties of the central regions bear a close resemblance with the classical colliding galaxies NGC 4038/4039 as seen in HST data (Whitmore and Schweizer 1995). This galaxy is the most massive in the whole sample and also has the highest star-formation rate ( $\sim 20 M_{\odot}/\text{yr}$ ). The inferred supernova (SN type II) frequency is one every 7 years. Surprisingly, the galaxy is very luminous in IR but seems to be rather de-

void of cool gas ( $M_{\text{HI}} < 10^8 M_{\odot}$  = detection limit) despite a very high star-formation rate (Bergvall et al., 2000). This suggests that either the starburst is about to run out of fuel or the gas is to a large extent in molecular and ionised form as suggested by calculation. The outer isocontours are distorted out to very faint isophotal levels ( $\mu_R \approx 26$  mag/arcsec<sup>2</sup>) on broad-band images (Fig. 2 – right). This is still visible but less extended in the H line demonstrating that the light originates mainly in stars. Hence, the large-scale distribution of stars in this galaxy is highly asymmetric. At all isophotal levels an

extension in the south-east is evident. This may be a tidal tail in development or most likely the remnants of such.

The H line profiles of this galaxy are broad, up to FWHM = 270 km/s, and have non-gaussian shape. This suggests that two or more non-virialised components may be present. In the centre, double peaked lines are present consistent with the presence of a counter rotating disk or high velocity blobs. This galaxy presents a strong central velocity gradient and large-scale distortions (see Fig. 4 – up). If we do not decompose the velocity field in several components, the rapid increase of the rotation curve is followed by a keplerian decrease. Alternatively, if we disentangle two possible components, the main one (in terms of intensity and extension) provides a low-velocity amplitude flat rotation curve while the second one gives a high-velocity amplitude but only in the central parts of the galaxy (see Fig. 5 – left). These properties indicate that the centre is not dynamically relaxed, while the outer velocity field shows a very slow rotation. The estimated stellar mass density exceeds by far what can be supported by the observed amount of rotation (G 30 km/s). Thus the galaxy is either not in equilibrium, or it is not primarily supported by rotation. These properties strongly suggest that the starburst has been triggered by a merger process.

### 3.2 ESO 338-IG04 (Tololo 1924-416)

HST observations of this well-known starburst (see Fig. 4 – left, Östlin et al., 1998) have revealed that in addition to

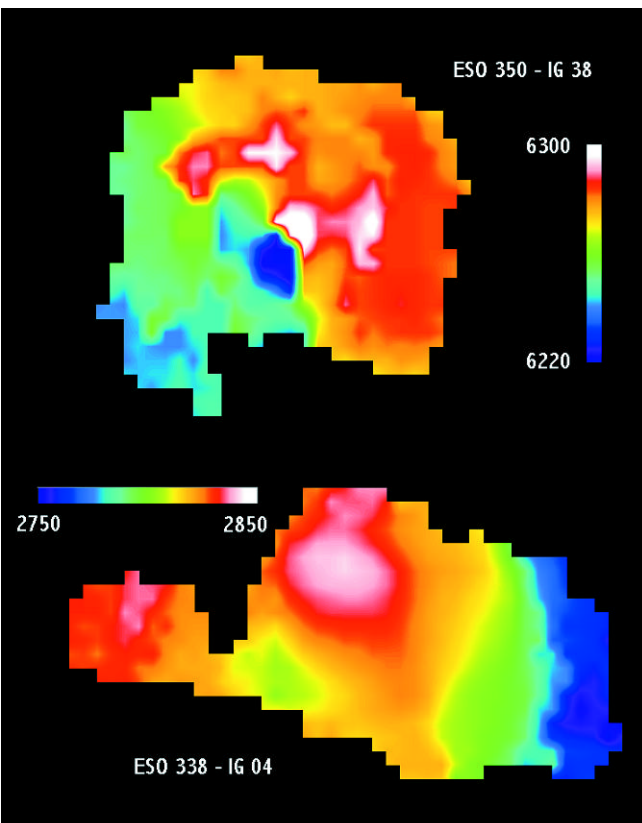


Figure 3: Velocity fields for ESO 350-IG38 (up) and ESO 338-IG04 (bottom). The two galaxies have the same pixel size (0.91 arcsec/px) and scale on the image; the horizontal size of the box is 42 arcsec. ESO 350-IG38: The velocity amplitude ranges linearly from violet (6220 km s<sup>-1</sup>) to white (6300 km s<sup>-1</sup>). ESO338-IG04: The velocity amplitude ranges linearly from violet (2750 km s<sup>-1</sup>) to white (2850 km s<sup>-1</sup>).

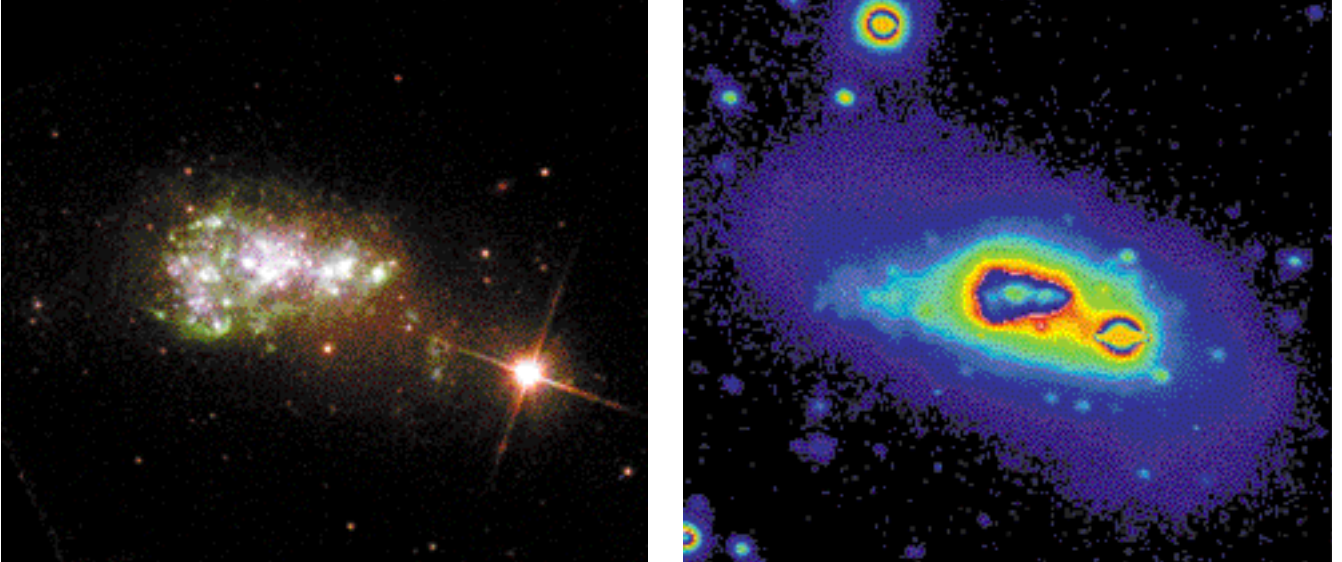


Figure 4: **ESO 338-IG04**. North is up, East is left. (Left): HST/WFPC2 true composite colour BVI-image. The scale of the box is 28 arcsec square. (Right): R-band CCD image. Note the irregular morphology at all isophotal levels. The faintest visible structures are  $\mu_R \approx 26$  mag/arc<sup>2</sup>. The size of the field is 60 arcsec  $\times$  53 arcsec, corresponding to 11  $\times$  9.5 kpc.

many young compact star clusters, it contains a system of intermediate-age ( $\sim 2$  Gyr) globular clusters, a fossil of a previous dramatic starburst event. This galaxy has a companion at a projected distance of 70 kpc to the south-west. There is a 5 kpc long tail towards east, and large-scale isophotal asymmetries down to the  $\mu_R = 26$  mag/arcsec<sup>2</sup> level (Fig. 4 – right). At fainter levels, the morphology becomes more regular, but a boxy shape remains on the western side. The tail has much bluer colours than the rest of the galaxy outside the starburst region, signifying a younger stellar population. It contains stellar clusters, and cannot be explained by a purely gaseous tail.

This galaxy has an almost chaotic velocity field (see Fig. 3 – bottom), with strong gradients and an extended tail with little internal velocity structure. Approximately 10 arcsec east of the centre, just at the border of the central star-forming region, there is a velocity component whose kinematical axis is perpendicular to the photometric major axis of the galaxy (Figs. 5 and 6 in Östlin et al., 1999). The radial light distribution indicates that the observed mean rotational velocity (if a such is at all meaningful to define in view of the irregular velocity field) cannot support the system gravitationally. The tail has almost no velocity gradient with respect to the centre ( $\leq 10$  km/s). On the other hand, the western half of the galaxy has a strong gradient and an implied rotational velocity of 80 km/s at a distance of 3 kpc from the centre. This is identical to the rotational velocity in the companion ESO 338-IG04B that has an equal photometric mass. Hence, the western part of the galaxy shows about the expected level of velocity difference with respect to the centre for rotational support to be possible. But what is happening at the eastern

side in the tail? The colour of the tail suggests that it has a distinctly different stellar population from the rest of the galaxy. The most likely is that the tail is a remnant of a merger and that projection effects prevent us from seeing the true velocity amplitude. The part of the galaxy on the eastern side which is not in the tail, does not emit strongly in H $\alpha$ , hence we have no information on its kinematics. Where the tail meets the starburst region, we see an increased H $\alpha$  velocity dispersion, perhaps due to a shock. This coincides with the location of the perpendicular dynamical component discussed above. The companion is probably too far away for tidal forces to influence the internal gas kinematics to such an extent that it may have caused the starburst and the peculiar velocity field.

Radio interferometric observations (Östlin et al., in preparation) reveal that the galaxy is embedded in a very large HI cloud, more than 7 arcminutes across (corresponding to 80 kpc at the distance of ESO 338-IG04). The HI cloud has irregular morphology with two main components and no single axis of rotation. ESO 338-IG04 appears to be located in the eastern HI cloud. The companion is detected in HI but lies further away. Although we cannot exclude that the starburst in ESO 338-IG04 is triggered by interaction with the companion, a merger appears more likely in view of the complex velocity field and the non-rotating arm.

## 4. Discussion on the Whole Sample

### 4.1 Photometric and kinematical analysis

The morphologies of the BCGs present strong large-scale asymmetries down to the faintest isophotal levels, re-

vealing large-scale asymmetries in the distribution of stars. In most cases we see clear signatures of merging/interaction. The young burst population dominates the integrated optical luminosities, while only contributing 1 to 5% of the total stellar mass, which ranges from a few times  $10^8$  to more than  $10^{10}$   $M_{\odot}$ . The mass is dominated by an older underlying population and the integrated (burst + old population) mass to light ratios are  $M/L_V \sim 1$ .

The velocity fields, in spite of the high signal-to-noise ratio of the emission lines, appear irregular and distorted, except for the two companion galaxies included in the sample. As the S/N is high, these irregular isovelocity fields should be considered as real. Some rotation curves appear strange or non-uniform; this indicates that the simple assumptions of a regular warp-free disk and pure circular motion around the centre are not valid in general. The estimated dynamical masses range from a few times  $10^8$  to a few times  $10^9$   $M_{\odot}$ . Secondary components have been detected in several cases.

In about half the cases, the observed rotational velocities are too small to allow for pure rotational support. A possible explanation is that velocity dispersion dominates the gravitational support. This is consistent with the observed line widths ( $\sigma_{H\alpha} = 35$  to 80 km/s), but does not explain the strange shape of many of the rotation curves (see Fig. 5). Another possibility is that the galaxies are not in dynamical equilibrium, e.g. because they are involved in mergers, explaining the peculiar kinematics. It is also possible that gas and stars are dynamically decoupled and the H $\alpha$  velocity field does not trace the gravitational potential. A way to distinguish between these alternatives would be to obtain the rotation curve and velocity dispersion for the

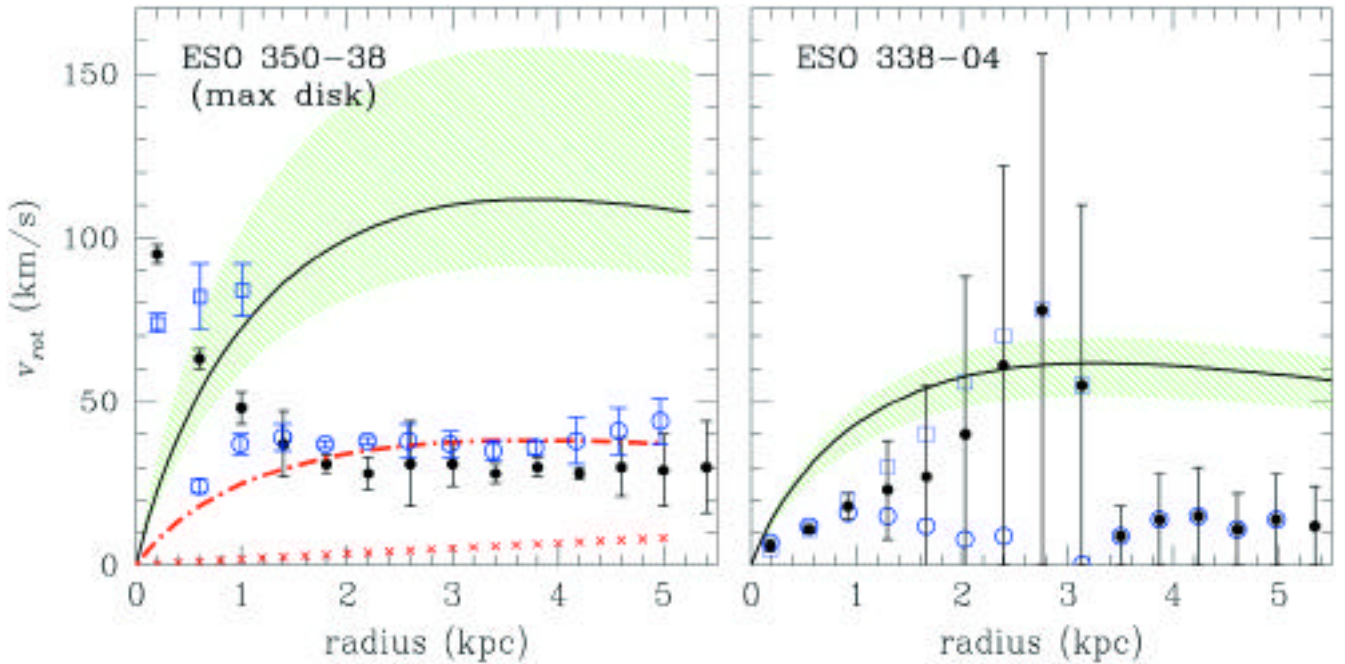


Figure 5: Mass model for ESO 350-IG38 (left) and ESO 338-IG04 (right). The solid line is the photometric rotation curve for the disk component; and the green shaded area is the allowed range based on the uncertainty in M/L. The filled circles show both sides'averaged observed rotation curves, the error bars represent mainly the deviation to pure circular motions. ESO 350-IG38 (left): the blue open symbols show the rotation curve based on the decomposed velocity field. The blue open circles correspond to the main component; the secondary component, which is counter rotating is shown by the blue open squares. The maximum disk model (in order to provide an upper limit of the (M/L)disk) has been computed on the main component. The dash-dot red line is the stellar disk component from the mass model and the crosses is the halo component (red crosses) is very faint, the total model (disk + halo) matches the stellar component. ESO338-IG04 (right): The blue open symbols show both sides of the rotation curve. The blue open circles correspond to the receding side while the approaching one is shown by the blue open squares. Due to the disagreement between the approaching and the receding sides, the averaged rotation curves do not represent the axisymmetric potential well of the galaxy, the instrumental accuracy of the velocity being 2–3 km/s at high signal-to-noise ratio. Furthermore, no dynamical model can be plotted for this galaxy.

stellar component. In two cases, we find evidence for the presence of dark matter within the extent of the H $\alpha$  rotation curves, and in two other cases we find marginal evidence. Indeed, even with a maximum disk model, the rotation curves computed from the surface brightness profiles cannot fit the observed rotation curve without an additional dark halo component.

#### 4.2 Spectral Evolutionary Models and Dynamical Analysis

Spectral evolutionary synthesis models in combination with colour profiles in the optical and near infrared are used to estimate the mass to light ratios (M/L) of the galaxies (the models are described in Bergvall and Rönnback, 1995). Photometric mass distributions were derived by integrating the luminosity profiles for the disk and burst components and using their corresponding M/L values. The photometric mass distributions are further compared to dynamical mass models (see Fig. 5). From B-band surface brightness photometry, an exponential disk has been separated from the burst by extrapolation of the profile of the outer regions where the contribution to the burst is marginal. The photometric M/L of the disks and of the bursts have been evaluated by matching the observed colours to extended sets of models with different IMF, mass limit

and star-formation histories (Östlin et al., 2001). The photometric total masses of the disk and of the burst have been obtained by integrating the luminosities with the M/L values in the allowed range. The dynamical M/L of the disk have been computed using a two-component (exponential disk + dark halo) best-fit mass model or maximum disk model (Carignan, 1985). In most cases, the M/L obtained from the dynamical mass models are lower than the ones obtained from the spectral evolutionary synthesis models. This means that the dynamical mass is under-evaluated, the velocity fields being disturbed by non-circular motions or/and that the galaxies are not rotationally supported.

#### 4.3 Merging in Process

For this sample of LBCGs, two kinds of perturbation are probably in competition: (1) merging processes distorting the velocity fields at large scale and (2) winds driven by starbursts strongly disturbing the circular motion of the ionised gas at smaller scales. Merging, interaction and wind driven by supernovae can induce non-circular motions of high amplitude to the gas. Then, due to dissipative collisions, the gas is probably decoupled from the rotation of the stars which constitute the dominant mass of the disk. Stars and gas are then decoupled due to dissipative colli-

sions in the gaseous component of the galaxies. Furthermore, the gas becomes a bad tracer of the potential well but a good tracer of starburst activity. Stars should be a better tracer of the potential well but their observations present difficulties due to the weakness of the continuum emission and absorption lines in this class of galaxies.

When considering the kinematics and morphologies of this sample of luminous BCGs, we are led to the conclusion that dwarf galaxy mergers are the favoured explanation for the starbursts. The dynamics of the studied galaxies fall into two broad classes: one with well behaving rotation curves at large radii and one with very perturbed dynamics. This may indicate a distinction of the fate of these galaxies, once the starbursts fade. Alternatively, depending on the state in which we see the interaction/merger, we will detect more or less chaotic velocity maps.

## 5. Perspectives

Dwarf galaxies are very common objects in the universe; compact galaxies (CGs) are frequent and blue compact galaxies (BCGs) are not rare. At high redshift, gas-rich dwarf galaxies and perhaps also CGs even can be the building blocks of the larger galaxies, merge and form stars during episodic processes in their evolution. The luminous blue compact galaxies (LBCGs)

# ESO VACANCY

Applications are invited for the position of

## Head of the Office for Science

**Assignment:** A strong research-oriented scientific staff with diverse expertise is essential to fulfil ESO's mandate of providing and maintaining international competitive observatories for its community of users. In this context the Head of the Office for Science will be responsible to the Director General for the science policies, and the main tasks will be

- to foster science across the entire Organisation and increase the exchange between ESO Chile and Garching;
- to support the efforts of ESO staff to conduct science at a high level;
- to provide a reference point for young scientists;
- to pursue actively the Fellowship, Studentship, Visitor programmes and carry out scientific exchanges with the European community through a strong and attractive Workshop Programme;
- to be the ESO representative at the International Research School recently created in the Munich area.

**Experience and knowledge:** Candidates must have an outstanding record of achievement in one or more areas of modern astrophysics and preferably be widely experienced in the use of large ground-based optical and/or radio telescopes. Excellent communication and management skills and a strong sense of team spirit are essential.

**Duty station:** Garching near Munich, Germany, with regular trips to Chile.

**Starting date:** 1 September 2001 or later.

We offer an attractive remuneration package including a competitive salary (tax free), comprehensive social benefits and financial help in relocating your family. The initial contract is for a period of three years with the possibility of a fixed-term extension. Serious consideration will be given to outstanding candidates willing to be seconded to ESO on extended leaves from their home institutions. Either the title or the grade may be subject to change according to education and the number of years of experience.

If you are interested in working in areas of front-line science and technology in a stimulating international research environment, please send us your CV (in English language) and the [ESO Application Form](#) (to be obtained from the ESO Home Page at <http://www.eso.org/>) and four letters of reference

**before 15 May 2001.**

For further information, please consult the ESO Home Page.

have luminosities and properties similar to galaxies seen at intermediate redshifts (e.g. Guzman et al., 1997). Moreover, they are among the least massive/luminous galaxies that are possible probes also at high redshifts. The sample of LBCGs presented here is not representative of classical BCGs but can be regarded as a reference sample for high redshift LBCGs, for which, moreover, observations present a serious bias. Even if there are evolutionary processes that make distant galaxies unique, the evolutionary history of a galaxy is not only a time-dependent parameter but it may also strongly depend on the environment. Furthermore, LBCGs can be thought of as nearby sites which mimic galaxy interaction, merging and the star triggering in higher-density environments of the young universe.

These local dwarf galaxy mergers may be the best analogues of hierarchical build-up of more massive galaxies at high redshifts.

### Acknowledgements

We would like to thank our collaborators Nils Bergvall, Josefa Masegosa, Jacques Boulesteix and Isabel Marquez for their contributions to this work. Jean-Luc Gach from Marseille Observatory is thanked for providing the computations for Figure 1. Nils Bergvall is thanked for his comments and his careful reading of this paper. The 3.6-m ESO and the astroworkshop teams are thanked for providing efficient support during the set-up of the instrument.

### References

- Amram P., Boulesteix J., Georgelin Y.M. et al., 1991, *The Messenger*, **64**, 44.  
Amram P., Balkowski C., Boulesteix J. et al., 1996, *A & A*, **310**, 737.  
Bergvall N. and Olofsson K., 1984, *The Messenger* **38**, 2.  
Bergvall N., Masegosa J., Östlin G. and Cernicharo J., 2000, *A&A* **359**, 41.

- Bergvall N., Rönnback J., 1995, *MNRAS* **273**, 603.  
Carignan C., 1985, *ApJ* **299**, 59.  
Östlin G., in "Massive Stellar Clusters", A. Lancon and C. Boily Eds., 2000, ASP Conf. Ser. **211**, p. 63.  
Östlin G., Amram P., Masegosa J., Bergvall N., Boulesteix J., 1999, *A&AS*, **137**, 419.  
Östlin G., Amram P., Masegosa J., Bergvall N., Boulesteix J. and Marquez I. 2001, to be submitted.  
Östlin G., Bergvall N., Rönnback J., 1998, *A&A* **335**, 85.  
Gach J.L. et al., 2001, in preparation for *ApJS*.  
Guzman R., Gallego J., Koo D.V. et al., 1997, *ApJ*, **489**, 559.  
Georgelin Y.M., Russeil D., Amram P. et al., 2000, *A & A* **357**, 308.  
Malkan, Gorjian and Tam, 1998, *ApJS* **117**, 25.  
Marcelin, M.; Boulesteix, J.; Courtes, G.; Milliard, B. *Nature*, vol. 297, May 6, 1982, p. 38-42.  
Searle L. and Sargent W.L.W., 1972, *ApJ*, **173**, 25.  
Whitmore B., Schweizer F., 1995, *AJ* **109**, 960.

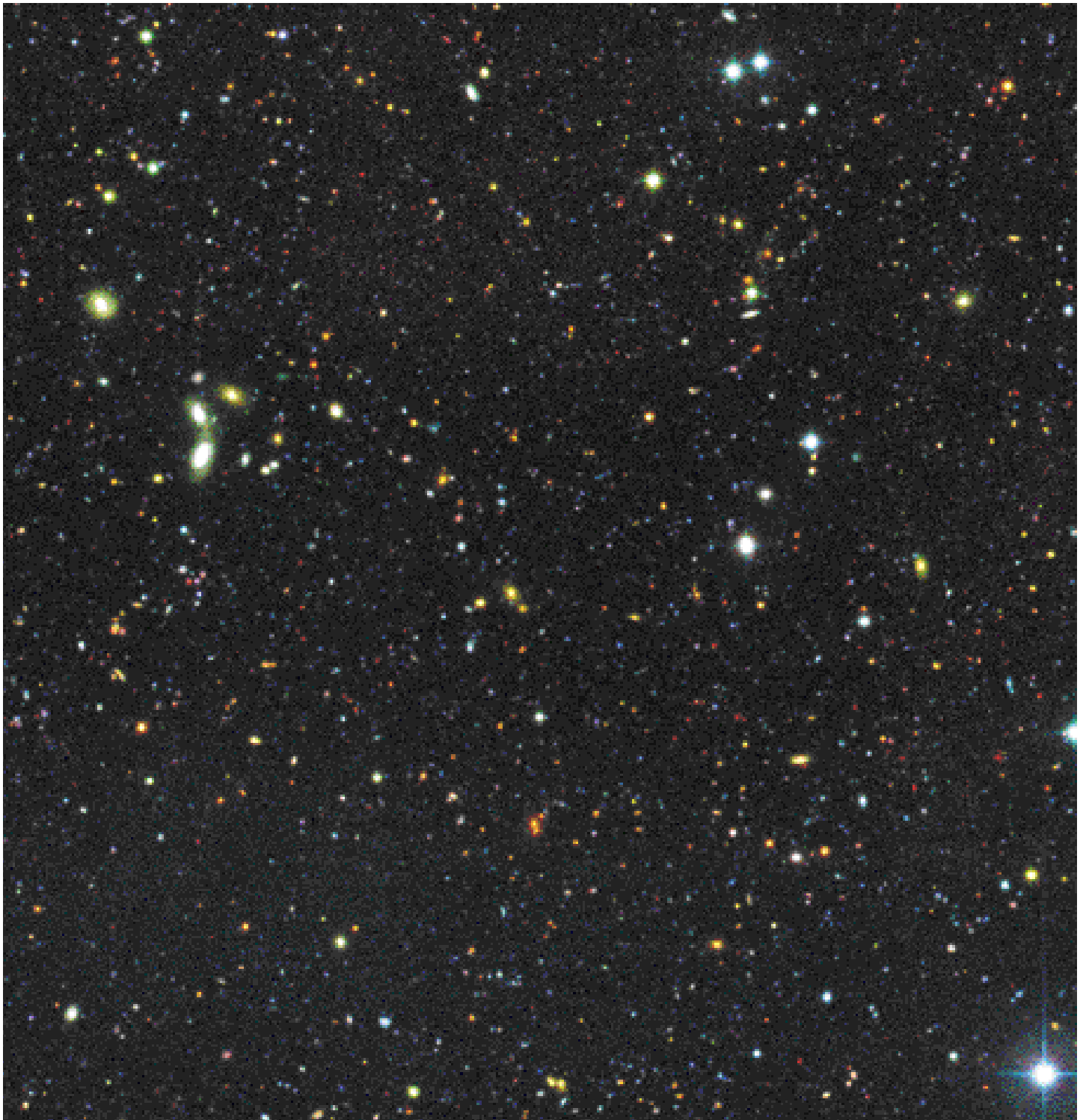
## EIS Data on the Chandra Deep Field South Released

The purpose of this note is to announce that the ESO Imaging Survey programme has released a full set of optical/infrared data covering the so-called Chandra Deep Field South (CDF-S) rapidly becoming a favoured target for cosmological studies in the southern hemisphere. The field was originally selected for deep X-ray observations with Chandra and XMM. The former have already been completed producing the deepest high-resolution X-ray

image ever taken with a total integration time of one million seconds. The data obtained by EIS include J and Ks infrared observations of an area of 0.1 square degree nearly matching the Chandra image down to  $J_{AB} \sim 23.4$  and  $K_{AB} \sim 22.6$  and  $UU'BVRI$  optical observations over 0.25 square degree, matching the XMM field of view, reaching 5 limiting magnitudes of  $U'_{AB} = 26.0$ ,  $U_{AB} = 25.7$ ,  $B_{AB} = 26.4$ ,  $V_{AB} = 25.4$ ,  $R_{AB} = 25.5$  and  $I_{AB} = 24.7$  mag, as

measured within a  $2 \times$  FWHM aperture.

Given the general interest on this field, fully calibrated images and associated weight maps as well as source lists have been made available worldwide on February 16, 2001 and March 5, 2001. The data can be requested through the URL "<http://www.eso.org/eis>". A first impression of the data is given by the colour composite image shown below which combines  $U$ ,  $R$ , and  $J+K$  infrared images.



# ANNOUNCEMENTS

## ESO Studentship Programme 2001

The European Southern Observatory research student programme aims at providing the opportunities and the facilities to enhance the post-graduate programmes of ESO member-state universities by bringing young scientists into close contact with the instruments, activities, and people at one of the world's foremost observatories. For more information about ESO's astronomical research activities please consult Research Projects and Activities (<http://www.eso.org/science/> or <http://www.eso.org/projects/>).

Students in the programme work on an advanced research degree under the formal tutelage of their home university and department, but come to either Garching or Vitacura-Santiago for a stay of normally up to two years to conduct part of their studies under the supervision of an ESO staff astronomer. Candidates and their national supervisors should agree on a research project together with the potential ESO local supervisor. This research programme should be described in the application and the name of the ESO local supervisor should also be mentioned. It is highly recommended that the applicants start their Ph.D. studies at their home institute before continuing their Ph.D. work and developing observational expertise at ESO.

The ESO studentship programme comprises about 14 positions, so that each year a total of up to 7 new studentships are available either at the ESO Headquarters in Garching or in Chile at the Vitacura Quarters. These positions are open to students enrolled in a Ph.D. programme in the ESO member states and exceptionally at a university outside the ESO member states.

**The closing date for applications is June 15, 2001.**

Please apply by using the ESO Studentship application form available on-line (<http://www.eso.org/gen-fac/adm/pers/forms/>).

European Southern Observatory  
Studentship Programme  
Karl-Schwarzschild-Str. 2  
85748 Garching bei München  
Germany  
abeller@eso.org

## PERSONNEL MOVEMENTS

### International Staff

(January – March 2001)

#### ARRIVALS

##### EUROPE

BRANDNER, Wolfgang (D), Adaptive Optics Instrument Scientist  
CHATZIMINAOGLOU, Evanthia (GR), Associate EIS  
CONAN, Rodolphe (F), Associate  
CONDORELLI, Livio (I), VLT Software System Manager for UNIX computers  
DEMARCO, Ricardo (RCH), Student  
EKVALL, Jenny (S), Associate  
HACKENBERG, Wolfgang (D), Laser Specialist  
KORNMESSER, Martin (D), Graphics Designer  
LAMPERSBERGER, Brigitte (D), Associate  
MARCHETTI, Enrico (I), Associate  
NELSON, Martine (UK), Division Secretary/Assistant  
TRIPICCHIO, Alfredo (I), Associate  
VAN BOEKEL, Roy (NL), Student  
VANZELLA, Eros (I), Student

##### CHILE

BAUVIR, Bertrand (B), Software Engineer  
HOUSEN, Nico (B), Software Engineer  
HUBRIG, Svetlana (D), Operations Staff Astronomer  
MOREL, Sébastien (F), VLT Instrument Operator  
SCHÜTZ, Oliver (D), Student

SLUSE, Dominique (B), Student  
WITTKOWSKI, Markus (D), VLT Instrument Operator  
WOODS, Paul (UK), Student

#### DEPARTURES

##### EUROPE

TORWIE-SCHMER, Claudia (D), Accounting Assistant

### Local Staff

(December 2000 – March 2001)

#### ARRIVALS

ALARCON, Hector, Telescope Instruments Operator, Paranal  
GODOY, Angelina, Bilingual Secretary, Santiago  
HERRERA, Cristian, Telescope Instruments Operator, Paranal  
MORALES, Alex, Maintenance Engineer, Paranal  
ROJAS, Manuel, Telescope Instruments Operator, Paranal

#### DEPARTURES

ABUTER, Roberto, Software Engineer, Paranal  
ALVAREZ, Roberto, Bilingual Secretary, Paranal  
BROWNING, Victoria, Paranal Administrator, Paranal  
FIGUEROA, Edgardo, Precision Mechanics, La Silla  
MARTIN, Gabriel, Telescope Instruments Operator, La Silla  
RAHMER, Gustavo, Optical Detector Engineer, Paranal

# A Challenge for

# Astronomers,

# Engineers in the field of Software Electronics and / or Mechanics,



The ESO Garching Headquarters

who are ready to work in areas of front  
line astronomy and technology in  
a multinational environment are invited to  
send us your application.



The ESO Paranal Observatory

For further information about currently  
available positions and employment con-  
ditions please consult our homepage;  
<http://www.eso.org>

*We offer an attractive remuneration package in-  
cluding a competitive net salary, comprehensive  
social benefits and professional training opportunities*

ESO, Karl-Schwarzschild-Str. 2, D-85748 Garching  
near Munich, Germany Tel. +49-89-3200-6553  
Fax +49-89-3200-6490



The ESO La Silla Observatory



**ESO. Astronomy made in Europe**

ESO, the European Southern Observatory, was created in 1962 to "... establish and operate an astronomical observatory in the southern hemisphere, equipped with powerful instruments, with the aim of furthering and organising collaboration in astronomy ...". It is supported by eight countries: Belgium, Denmark, France, Germany, Italy, the Netherlands, Sweden and Switzerland. ESO operates at two sites. It operates the La Silla observatory in the Atacama desert, 600 km north of Santiago de Chile, at 2,400 m altitude, where several optical telescopes with diameters up to 3.6 m and a 15-m submillimetre radio telescope (SEST) are now in operation. In addition, ESO is in the process of building the Very Large Telescope (VLT) on Paranal, a 2,600 m high mountain approximately 130 km south of Antofagasta, in the driest part of the Atacama desert. The VLT consists of four 8.2-metre and three 1.8-metre telescopes. These telescopes can also be used in combination as a giant interferometer (VLTI). In April 1999, the first 8.2-metre telescope (called ANTU) started regular operation, and also the three other ones (KUEYEN, MELIPAL and YEPUN) have already delivered pictures of excellent quality. Over 1200 proposals are made each year for the use of the ESO telescopes. The ESO Headquarters are located in Garching, near Munich, Germany. This is the scientific, technical and administrative centre of ESO where technical development programmes are carried out to provide the La Silla and Paranal observatories with the most advanced instruments. There are also extensive astronomical data facilities. In Europe ESO employs about 200 international staff members, Fellows and Associates; in Chile about 70 and, in addition, about 130 local staff members.

The ESO MESSENGER is published four times a year: normally in March, June, September and December. ESO also publishes Conference Proceedings, Preprints, Technical Notes and other material connected to its activities. Press Releases inform the media about particular events. For further information, contact the ESO Education and Public Relations Department at the following address:

EUROPEAN  
SOUTHERN OBSERVATORY  
Karl-Schwarzschild-Str. 2  
D-85748 Garching bei München  
Germany  
Tel. (089) 320 06-0  
Telefax (089) 3202362  
ips@eso.org (internet)  
URL: <http://www.eso.org>  
<http://www.eso.org/gen-fac/pubs/messenger/>

The ESO Messenger:  
Editor: Marie-Hélène Demoulin  
Technical editor: Kurt Kjär

Printed by  
J. Gotteswinter GmbH  
Buch- und Offsetdruck  
Joseph-Dollinger-Bogen 22  
D-80807 München  
Germany

ISSN 0722-6691

# SCIENTIFIC PREPRINTS

(January – March 2001)

1408. E. Scannapieco and T. Broadhurst: Linking the Metallicity Distribution of Galactic Halo Stars to the Enrichment History of the Universe. *ApJ Letters*.  
1409. M. Rejkuba: Deep VLT Search for Globular Clusters in NGC 5128: Color-Magnitude Diagrams and Globular Cluster Luminosity Function. *A&A*.  
1410. Th. Rivinius, D. Baade, S. Štefl, R.H.D. Townsend, O. Stahl, B. Wolf and A. Kaufer: Stellar and Circumstellar Activity of the Be Star  $\mu$ Centauri. III. Multiline Nonradial Pulsation Modeling. *A&A*.  
1411. B. Paltrinieri, F.R. Ferraro, F. Paresce and G. De Marchi: VLT Observations of the Peculiar Globular Cluster NGC 6712. III. The Evolved Stellar Population. *AJ*.  
1412. B. L. Jensen et al.: The Afterglow of the Short/Intermediate-Duration Gamma-Ray Burst GRB 000301C: A Jet at  $z = 2.04$ . *A&A*.

## Contents

J. Alves, C. Lada and E. Lada: Seeing the Light Through the Dark . . . 1

### TELESCOPES AND INSTRUMENTATION

- A. Gilliotte: La Silla Telescope Status, a Great Achievement on Image Quality Performances . . . . . 2  
A. Gilliotte: Image Quality Improvement of the 2.2-m . . . . . 4  
O. Hainaut and the NTT Team: NEWS from the NTT . . . . . 7  
H. Jones: 2p2 Team News . . . . . 9  
H. Jones, A. Renzini, P. Rosati and W. Seifert: Tunable Filters and Large Telescopes . . . . . 10

### REPORTS FROM OBSERVERS

- J. Alves, C. Lada and E. Lada: Seeing the Light Through the Dark (Continued from page 1) . . . . . 15  
F. Comerón and M. Fernández: Strong Accretion and Mass Loss Near the Substellar Limit . . . . . 21  
J.U. Fynbo, P. Møller, B. Thomsen: Star Formation at  $z = 2-4$ : Going Below the Spectroscopic Limit with FORS1 . . . . . 24  
H. Jones, B. Stappers, B. Gaensler: Discovery of a Bow-Shock Nebula Around the Pulsar B0740-28 . . . . . 27  
L. Testi, L. Vanzi, F. Massi: Young Stellar Clusters in the Vela D Molecular Cloud . . . . . 28  
P. Amram and G. Östlin: Building Luminous Blue Compact Galaxies by Merging . . . . . 31

### OTHER ASTRONOMICAL NEWS

EIS Data on the Chandra Deep Field South Released . . . . . 37

### ANNOUNCEMENTS

- ESO Vacancy. Head of the Office for Science . . . . . 36  
ESO Studentship Programme 2001 . . . . . 38  
Personnel Movements . . . . . 38  
ESO Vacancies. A Challenge for Astronomers, Engineers in the Field of Software, Electronics and/or Mechanics . . . . . 39  
Scientific Preprints (January – March 2001) . . . . . 40